Using Gravitational Waves as a Probe into the Interior of Isolated Neutron Stars

by

Matthew Ball

A dissertation accepted and approved in partial fulfillment of the

requirements for the degree of

Doctor of Philosophy

in Physics

Dissertation Committee:

Ben Farr, Chair

Raymond Frey, Advisor

Dean Livelybrooks, Core Member

Carol Paty, Institutional Representative

University of Oregon

June 2025

DISSERTATION ABSTRACT

Matthew Ball

Doctor of Philosophy in Physics

Title: Using Gravitational Waves as a Probe into the Interior of Isolated Neutron Stars

The ever-increasing sensitivity of the Advanced LIGO detectors presents a host of new challenges and opportunities within gravitational wave (GW) astronomy. The ability to observe more of the universe also opens the door to unexpected outcomes. This will likely range from new types of astrophysical signals that shed light on new physics to new types of background noise that require novel techniques to mitigate. Both categories present new challenges that must be overcome to best understand the vast amount of information that future observing runs will bring. This dissertation explores my role in tackling problems in both of these categories.

One of the worst potential noise sources in a GW detector network is one that is coherent between multiple detectors. Modern analyses rely on the assumption that real GW events will be coherent across long distances, but noise artifacts will not. The transient magnetic fields generated by individual lightning strokes can propagate great distances at nearly the speed of light potentially causing unwanted noise artifacts coherent between detectors. We examine the effects of this on current and future detectors.

The internal structure of neutron stars is largely unknown. GWs emitted by oscillations within the star could teach us much about this structure. Highly magnetized neutron stars emit X-ray flares that may be associated with these

oscillations. We present methods for extracting astrophysical parameters from these signals that would augment future searches for GWs that target these objects.

These oscillations may also be generated by the process that causes glitches in rotating pulsars. We augment our previous methods to consider pulsar glitches and include a model for longer duration continuous waves that may also be emitted. We perform a search for short duration GWs associated with a glitch in the Vela pulsar from December 2016 and attempt to place limits on the neutron star parameters. We then repeat this for the collaboration search for GWs from the April 2024 Vela pulsar glitch.

This dissertation contains previously published and unpublished material.

CURRICULUM VITAE

NAME OF AUTHOR: Matthew Ball

GRADUATE AND UNDERGRADUATE SCHOOLS ATTENDED:

University of Oregon, Eugene, OR, USA
Oregon State University, Corvallis, OR, USA

DEGREES AWARDED:

Doctor of Philosophy, Physics, 2025, University of Oregon
Bachelor of Science, Physics, 2018, Oregon State University

AREAS OF SPECIAL INTEREST:

Gravitational-Wave Astrophysics
Mutimessenger Astrophysics

PROFESSIONAL EXPERIENCE:

Research Assistant, Department of Physics, University of Oregon, 2020-2025
Teaching Assistant, Department of Physics, University of Oregon, 2018-2025

GRANTS, AWARDS AND HONORS:

The LIGO Laboratory Award for Excellence in Detector Characterization and Calibration, LIGO Lab, 2022

PUBLICATIONS:

Ball, M., Frey, R., Merfeld, K. (2024). Prospects for neutron star parameter estimation using gravitational waves from f modes associated with magnetar flares. *Monthly Notices of the Royal Astronomical Society*, 533, 3090.

Ball, M., Frey, R. (2023). Galactic Magnetars and Cosmic Explorer. `https://dcc.cosmicexplorer.org/CE-P2300010/public`, Cosmic Explorer Science Letter

Janssens, K.; Ball, M.; Schofield, R. M. S.; Christensen, N.; Frey, R.; van Remortel, N.; et al. (2022). Correlated 1–1000 Hz magnetic field fluctuations from lightning over Earth-scale distances and their impact on gravitational wave searches. *Physical Review D*, 107, 022004.

Abbott, R., et al. (2023) Search for Gravitational-wave Transients Associated with Magnetar Bursts in Advanced LIGO and Advanced Virgo Data from the Third Observing Run. *The Astrophysical Journal*, 966, 137

The LIGO Scientific Collaboration, Virgo Collaboration, KAGRA Collaboration, CHIME/FRB Collaboration, (submitted). Search for gravitational waves associated with fast radio bursts detected by CHIME/FRB during the LIGO-Virgo observing run O3b.

The LIGO Scientific Collaboration, Virgo Collaboration, KAGRA Collaboration (in-preparation). Search for gravitational waves associated with gamma-ray bursts detected by Fermi and Swift during the LIGO-Virgo observing run O4a.

The LIGO Scientific Collaboration, Virgo Collaboration, KAGRA Collaboration. (in-preparation). Constraints on gravitational waves from the 2024 Vela pulsar glitch

Ball, M., Frey, R. (in-preparation). Methods for estimating neutron star parameters using multiple mechanisms for gravitational wave emission associated with pulsar glitches.

ACKNOWLEDGEMENTS

This dissertation would not have been possible without the tutelage of Ray Frey. I am also thankful to Robert Schofield, who taught me much about how the interferometers worked during my time at the LIGO Hanford Observatory. I would like to thank my fellow members of the Oregon LIGO group for providing a sense of community and specifically Adrian Helmling-Cornell, who was my desk neighbor for nearly the entirety of my time in graduate school. I would like to thank Claire Albrecht and Jeremy Metzner for their constant companionship, especially during our first year in the Binney. Lastly, I would like to thank my parents for always supporting me, even if they never really understood what I was working on.

To my parents

TABLE OF CONTENTS

Chapter Page

Chapter Page

LIST OF FIGURES

Figure Page

LIST OF TABLES

Table Page

CHAPTER I

INTRODUCTION

On September 14, 2015, the Laser Interferometer Gravitational Wave Observatory (LIGO) measured a fluctuation of spacetime smaller than the width of a proton created by the merger of two black holes nearly one and a half billion lightyears from Earth (B. Abbott et al., 2016b). With this, the era of gravitational wave astronomy had begun. The first and second observing runs (O1 and O2 respectively) would detect a total of 11 binary mergers (B. Abbott et al., 2019) including the first binary neutron star merger (B. P. Abbott et al., 2017b) along with the coincident measurement of a gamma-ray burst (B. P. Abbott et al., 2017a, 2017c), ushering in the era of multimessenger astrophysics.

The third observing run was a bit tamer, bringing 39 candidates during the first half (referred to as O3a) (R. Abbott et al., 2021d) and an additional 35 candidates during O3b (R. Abbott et al., 2023). While not capturing any multimessenger detections, O3 did still bring two new binary neutron star mergers (R. Abbott et al., 2021e) as well as the largest binary black hole merger observed (R. Abbott et al., 2020). So far, the fourth observing run has continued the trend of even more detections, with the most interesting detection being the merger of a neutron star with a mass-gap object (Abac et al., 2024).

This dissertation tells the story of my path through GW astrophysics. In Chapter II, I lay the groundwork for how general relativity leads to gravitational waves. I also discuss how we measure them as well as describe a few common sources. Then, in Chapter III, I detail the smaller projects I worked on during my time at the LIGO Hanford observatory in 2019. In Chapter IV, I present my first major project, where I examined the effects of the magnetic fields from lightning strikes on the LIGO detector network as a source of coherent noise. In Chapter V, I pivot into astrophysical data analysis with a project seeking to improve searches for GWs associated with magnetar flares through methods for performing parameter estimation to extract neutron star parameters from results. Chapter VI modifies and extends this work to GWs associated with pulsar glitches, now combining long duration continuous wave search results with short duration burst search results in a first-of-its-kind analysis. I also apply these methods to the April 2024 Vela pulsar glitch during O4. Finally, in Chapter VII, I give some final thoughts on this journey and some lessons learned.

CHAPTER II

BACKGROUND

This chapter will provide an overview of how gravitational waves mathematically arise from general relativity following discussions from Hartle (2002); Landau and Lfshitz (1975); Misner, Thorne, and Wheeler (1973). This chapter will also discuss various sources of gravitational waves as well as how they are measured.

2.1 General Relativity and the Mathematics of Gravitational Waves

In classical, Newtonian mechanics, gravity is a force exerted by massive objects on each other. In the simplest two-body system, the force is proportional to the product of both masses and inversely proportional to the square of the distance between them. G is the gravitational constant, approximately equal to $6.67 \times 10^{-11}\mathrm{Nm^2kg^{-2}}$.

$$F_G = \frac{Gm_1m_2}{r^2} \tag{2.1}$$

Since the force of gravity is a conservative force, it can be expressed in terms of a scalar field Φ: $F = -\nabla\Phi$. We can generally express this gravitational field in terms of the mass distribution (density) ρ:

$$\nabla^2\Phi = 4\pi\rho \tag{2.2}$$

From a reductionist point of view, this roughly says that the curvature of the gravitational field is equal to the mass distribution. We might then ask: *what* is actually curving here?

2.1.1 The Einstein Field Equations.

General relativity suggests that this medium is a 4-dimensional spacetime, and that this relation can instead be written as in Equation 2.3 where G is the gravitational constant again, and c is the speed of light.

$$G_{\mu\nu} = \frac{8\pi G}{c^4} T_{\mu\nu} \tag{2.3}$$

Here, the curvature of the scalar gravitational field $\nabla^2\Phi$ and the scalar mass/density distribution ρ are replaced by the rank-2 tensors $G_{\mu\nu}$ and $T_{\mu\nu}$, respectively, where $\mu, \nu = 0, 1, 2, 3$. $G_{\mu\nu}$ is referred to as the Einstein curvature tensor and $T_{\mu\nu}$ is the stress-energy tensor. As these are a four-dimensional tensors, this actually represents 16 coupled, partial differential equations (though, since the tensors are symmetric, there are only 10 unique equations).

Let's break down these tensors a little. Starting with the stress-energy tensor $T_{\mu\nu}$, we can divide it up into four primary pieces. Here, we let $i, j = 1, 2, 3$ in contrast to our previous definition(s) of μ and ν. T^{00} is the scalar energy density. T^{i0} is the momentum density along direction i. T^{0j} is energy flux along direction j, although since $T^{\mu\nu}$ is symmetric, these two quantities are equivalent. Lastly, $T^{i,j}$ is the mechanical stress tensor, which describes the ith pressure applied to a surface in direction j.

To understand the Einstein tensor $G_{\mu\nu}$, we need to define a few quantities. The backbone of general relativity is the metric tensor $g_{\mu\nu}$ which describes how displacements in one coordinate axis change as you vary other coordinates. The metric tensor connected to the line element ds which describes the spacetime distance of an infinitesimal displacement.

$$ds^2 = g_{\mu\nu} dx^\mu dx^\nu \tag{2.4}$$

For a flat spacetime in Cartesian coordinates, the metric is diagonal and the line element takes the form:

$$ds^2 = -\left(cdt\right)^2 + dx^2 + dy^2 + dz^2 \tag{2.5}$$

In a coordinate space described by some $g_{\mu\nu}$, we can describe the motion of particles in free-fall via the geodesic equation:

$$\frac{d^2 x^\alpha}{ds^2} + \Gamma^\alpha{}_{\mu\nu} \frac{dx^\mu}{ds} \frac{dx^\nu}{ds} \tag{2.6}$$

Where $\Gamma^\alpha{}_{\mu\nu}$ are the Christoffel symbols, defined as

$$\Gamma^\alpha{}_{\mu\nu} = \frac{1}{2} g^{\alpha\beta} \left(\partial_\nu g_{\beta\mu} + \partial_\mu g_{\beta\nu} - \partial_\beta g_{\mu\nu}\right) \tag{2.7}$$

We can then introduce the Riemann curvature tensor $R_{\alpha\beta\mu\nu}$

$$R_{\alpha\beta\mu\nu} = g_{\alpha\gamma} \left(\partial_\mu \Gamma^\gamma{}_{\beta\nu} - \partial_\nu \Gamma^\gamma{}_{\beta\mu} + \Gamma^\gamma{}_{\delta\mu} \Gamma^\delta{}_{\beta\nu} - \Gamma^\gamma{}_{\delta\nu} \Gamma^\delta{}_{\beta\mu}\right) \tag{2.8}$$

From the Riemann tensor, we can define the Ricci curvature tensor $R_{\mu\nu}$ as a partial contraction of the Riemann tensor:

$$R_{\mu\nu} \equiv R^\alpha{}_{\mu\alpha\nu} = \partial_\alpha \Gamma^\alpha{}_{\mu\nu} - \partial_\nu \Gamma^\alpha{}_{\mu\alpha} + \Gamma^\alpha{}_{\beta\alpha} \Gamma^\beta{}_{\mu\nu} - \Gamma^\alpha{}_{\beta\nu} \Gamma^\beta{}_{\mu\alpha} \tag{2.9}$$

We can contract this further to define the Ricci scalar curvature

$$R \equiv R^{\mu}{}_{\mu} \tag{2.10}$$

With these definitions, we can properly define the Einstein curvature tensor:

$$G_{\mu\nu} \equiv g_{\mu\gamma}\left(R^{\gamma}{}_{\nu} - \frac{1}{2}\delta^{\gamma}{}_{\nu}R\right) = R_{\mu\nu} - \frac{1}{2}g_{\mu\nu}R \tag{2.11}$$

2.1.2 Linearized Gravity. For weak-field situations, we consider a perturbation to a flat spacetime of the form:

$$g_{\mu\nu} = \eta_{\mu\nu} + h_{\mu\nu}, \quad |h_{\mu\nu}| << 1 \tag{2.12}$$

where $\eta_{\mu\nu}$ is the flat Minkowski metric (see Equation 2.5). Under this substitution, the Christoffel symbols become:

$$\Gamma^{\alpha}{}_{\mu\nu} = \frac{1}{2}\eta^{\alpha\beta}\left(\partial_{\nu}h_{\beta\mu} + \partial_{\mu}h_{\beta\nu} - \partial_{\beta}h_{\mu\nu}\right) + \mathcal{O}\left(h^2\right). \tag{2.13}$$

We can also do this for the Ricci tensor:

$$\begin{aligned} R_{\mu\nu} &= \partial_{\alpha}\Gamma^{\alpha}{}_{\mu\nu} - \partial_{\nu}\Gamma^{\alpha}{}_{\mu\alpha} + \mathcal{O}\left(h^2\right) \\ &= \frac{1}{2}\left(\partial_{\alpha}\partial_{\nu}h^{\alpha}{}_{\mu} + \partial_{\alpha}\partial_{\mu}h^{\alpha}{}_{\nu} - \partial_{\alpha}\partial^{\alpha}h_{\mu\nu} - \partial_{\mu}\partial_{\nu}h^{\alpha}{}_{\alpha}\right) \end{aligned} \tag{2.14}$$

and the contracted Ricci scalar:

$$R = g^{\mu\nu}R_{\mu\nu} \approx \eta^{\mu\nu}R_{\mu\nu} = \partial_{\alpha}\partial^{\beta}h^{\alpha}{}_{\beta} - \partial_{\alpha}\partial^{\alpha}h^{\beta}{}_{\beta} \tag{2.15}$$

Substituting this into the Einstein field equation gives (in geometric units where $c = G = 1$)

$$G_{\mu\nu} = \frac{1}{2}\left(\partial_\alpha\partial_\nu h^\alpha{}_\mu + \partial_\alpha\partial_\mu h^\alpha{}_\nu - \partial_\alpha\partial^\alpha h_{\mu\nu} - \partial_\mu\partial_\nu h^\alpha{}_\alpha - \eta_{\mu\nu}\partial_\alpha\partial^\beta h^\alpha{}_\beta + \eta_{\mu\nu}\partial_\alpha\partial^\alpha h^\beta{}_\beta\right) = 8\pi T_{\mu\nu} \tag{2.16}$$

We can make the transformation (Equation 2.17) where $h \equiv \eta^{\mu\nu}h_{\mu\nu}$.

$$\overline{h}_{\mu\nu} \equiv h_{\mu\nu} - \frac{1}{2}\eta_{\mu\nu}h \tag{2.17}$$

We can then write the linearized field equation as:

$$\partial_\alpha\partial_\nu\overline{h}^\alpha{}_\mu + \partial_\alpha\partial_\mu\overline{h}^\alpha{}_\nu - \partial_\alpha\partial^\alpha\overline{h}_{\mu\nu} - \eta_{\mu\nu}\partial_\alpha\partial^\beta\overline{h}^\alpha{}_\beta = 16\pi T_{\mu\nu} \tag{2.18}$$

This can be further simplified after considering gauge and coordinate transformations. Consider the infinitesimal coordinate transformation

$$x^{\mu'} = x^\mu + \xi^\mu \tag{2.19}$$

The metric will transform according to

$$g_{\mu'\nu'}(x^{\alpha'}) = g_{\mu\nu}(x^\alpha)\frac{\partial x^\mu}{\partial x^{\mu'}}\frac{\partial x^\nu}{\partial x^{\nu'}} \tag{2.20}$$

This works out to

$$g_{\mu'\nu'}(x^{\alpha'}) = g_{\mu'\nu'}(x^\alpha) - \partial_{\nu'}\xi_{\mu'} - \partial_{\mu'}\xi_{\nu'} + \mathcal{O}\left((\partial\xi)^2\right) \tag{2.21}$$

If we consider that our coordinate transformation is infinitesimal, then only the perturbation should transform under this coordinate transform:

$$g_{\mu'\nu'}(x^{\alpha'}) = \eta_{\mu'\nu'} + h_{\mu'\nu'}(x^\alpha) - \partial_{\nu'}\xi_{\mu'} - \partial_{\mu'}\xi_{\nu'} + \mathcal{O}\left((\partial\xi)^2\right) \tag{2.22}$$

For this linearized gravity to hold under such a coordinate transformation, we must require that the perturbation satisfy

$$h_{\mu\nu}^{\text{new}} = h_{\mu\nu}^{\text{old}} - \partial_\nu \xi_\mu - \partial_\mu \xi_\nu \tag{2.23}$$

If we transform this back in terms of $\overline{h}$, we get

$$\overline{h}_{\mu\nu}^{\text{new}} = \overline{h}_{\mu\nu}^{\text{old}} - \partial_\mu \xi_\nu - \partial_\nu \xi_\mu + \eta_{\mu\nu} \partial_\alpha \xi^\alpha \tag{2.24}$$

We can then introduce the gauge condition:

$$\partial_\alpha \overline{h}^{\text{new}\,\mu\alpha} = 0 \tag{2.25}$$

Imposing this gauge condition on Equation 2.24 gives

$$\begin{aligned} \partial_\alpha \overline{h}^{\text{new}\,\mu\alpha} &= \partial_\alpha \overline{h}^{\text{old}\,\mu\alpha} - \partial_\alpha \partial^\alpha \xi^\mu = 0 \\ \partial_\alpha \partial^\alpha \xi^\mu &= \partial_\alpha \overline{h}^{\mu\alpha} \end{aligned} \tag{2.26}$$

As long as our choice of ξ^μ satisfies this condition, we are free to use this gauge transformation. The linearized field equations then reduce to

$$-\partial_\alpha \partial^\alpha \overline{h}_{\mu\nu} = 16\pi T_{\mu\nu} \tag{2.27}$$

2.1.3 Plane Wave solutions in Vacuum.

In the simplest case, we consider how the perturbation metric $\overline{h}_{\mu\nu}$ behaves in vacuum where $T_{\mu\nu} = 0$

$$\partial_\alpha \partial^\alpha \overline{h}_{\mu\nu} = 0 \tag{2.28}$$

This is simply a wave equation, so the simplest solution is a monochromatic, plane wave:

$$\overline{h}_{\mu\nu} = \mathrm{Re}\left(a_{\mu\nu} e^{ik_\alpha x^\alpha}\right) \tag{2.29}$$

where the values $a_{\mu\nu}$ and k_α are constants that satisfy the requirements:

$$\begin{aligned} k_\alpha k^\alpha &= 0 \\ a_{\mu\alpha} k^\alpha &= 0 \end{aligned} \tag{2.30}$$

These conditions describe a transverse, plane wave with frequency $\omega = k_0 = (k_x^2 + k_y^2 + k_z^2)^{1/2}$ traveling at the speed of light in the direction of the spatial 3-vector k_i with amplitude $a_{\mu\nu}$.

2.1.4 Gravitational Wave Polarization.

From the freedom of our gauge transformation (Equation 2.26), we can choose functions ξ^μ such that we can impose the extra constraints $a^\mu{}_\mu = 0$ and $a_{\mu\alpha} u^\alpha = 0$, where u^μ is a 4-velocity representing a specific global Lorentz frame. Also, recall that $h_{\mu\nu}$ is symmetric, so $a_{\mu\nu}$ must also be symmetric.

It helps to consider a stationary frame where $u^0 = 1$ and $u^i = 0$. The two gauge-induced constraints tell us a few things about the amplitude $a_{\mu\nu}$. The condition in Equation 2.31 tells us that only the spatial components of $a_{\mu\nu}$ are non-zero. The condition in Equation 2.32 tells us that the trace of $a_{\mu\nu}$ must be zero.

$$\begin{aligned} a_{\mu\alpha} u^\alpha &= 0 \\ a_{\mu 0} &= 0 \end{aligned} \tag{2.31}$$

$$
\begin{aligned}
a^{\mu}{}_{\mu} &= 0 \\
a^{j}{}_{j} &= 0
\end{aligned} \tag{2.32}
$$

Let's also consider the case where the vector k^i is pointing only in the $+z$ direction, $k^i = (0, 0, \omega)$. The constraint in Equation 2.30 then becomes Equation 2.33 which tells us that all z-components of $a_{\mu\nu}$ must also be zero

$$
\begin{aligned}
a_{\mu\alpha} k^{\alpha} &= 0 \\
a_{j3} &= 0
\end{aligned} \tag{2.33}
$$

After considering these constraints, we are left with

$$
\overline{h}_{\mu\nu} = \begin{pmatrix} 0 & 0 & 0 & 0 \\ 0 & a_{11} & a_{12} & 0 \\ 0 & a_{12} & -a_{11} & 0 \\ 0 & 0 & 0 & 0 \end{pmatrix} e^{i\omega(z-t)} \tag{2.34}
$$

The gauge transformations that let us reduce the metric perturbation to this are referred to as the transverse-traceless gauge, which we will denote by $h^{TT}_{\mu\nu}$. The remaining amplitude terms are usually written as $a_{11} = A_{+}$ and $a_{12} = A_{\times}$, alluding to the two polarization vectors. We can visualize the effect of these polarizations best by considering a ring of test particles and watching how they move as the wave passes through the ring. From the components of $a_{\mu\nu}$, we can estimate the effect by essentially reading off the non-zero components. The polarization we call "plus" represents the a_{xx} and a_{yy} components, so we might expect the ring to deform along the x- and y-axes directly. Similarly, the "cross" polarization represents the

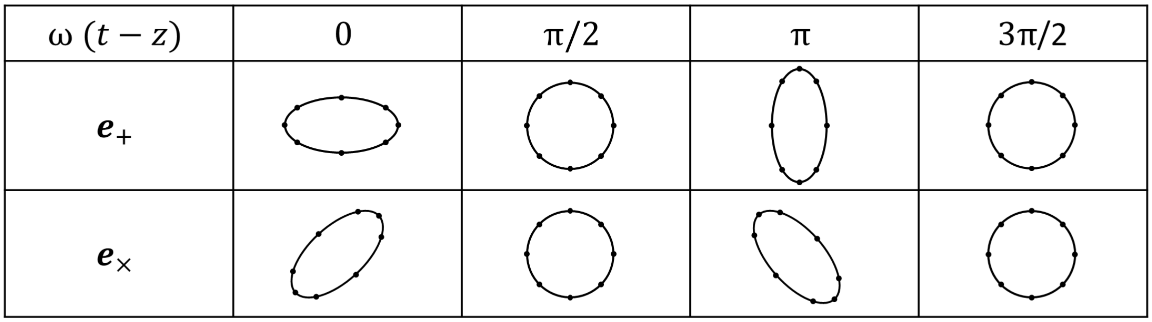

Figure 1. Phase evolution of the effect of a GW passing through a ring of particles. The two polarzations are shown separately. Here, we denote the plus polarization by the unit vector $\boldsymbol{e}_+$ and the cross polarization by the unit vector $\boldsymbol{e}_\times$.

a_{xy} and a_{yx} components, so we might expect the ring to deform along the $y = \pm x$ directions. Figure 1 shows this deformation explicitly.

2.1.5 Minimum Necessary Conditions for Emission. To consider the emission of gravitational waves, we need to look at more general solutions to the linearized field equations (Equation 2.27), this time without simplifying to a vacuum solution. Integrating Equation 2.27 gives Equation 2.35.

$$\overline{h}^{\mu\nu}(t, \boldsymbol{x}) = \frac{4G}{c^4} \int d^3x' \frac{T^{\mu\nu}(t - |\boldsymbol{x} - \boldsymbol{x}'|/c, \boldsymbol{x}')}{|\boldsymbol{x} - \boldsymbol{x}'|} \tag{2.35}$$

Since, in practice, any measurement of gravitational waves will be far from the source, we consider the far-field limit in Equation 2.36.

$$\overline{h}^{\mu\nu}(t, \boldsymbol{x}) \xrightarrow[r\to\infty]{} \frac{4G}{c^4 r} \int d^3x' T^{\mu\nu}(t - r/c, \boldsymbol{x}') \tag{2.36}$$

From Equation 2.31, we know that far from the source in vacuum, only the spatial part of $\overline{h}^{\mu\nu}$ is non-zero, so we need only consider the spatial components of Equation 2.36. We can write it as

$$\overline{h}^{ij}(t, \boldsymbol{x}) \xrightarrow[r\to\infty]{} \frac{4G}{c^4 r} \int d^3x' T^{ij}(t - r/c, \boldsymbol{x}') \tag{2.37}$$

In the limit of a flat spacetime, the stress-energy tensor obeys conservation of energy and momentum (Equation 2.38).

$$\partial_\beta T^{\alpha\beta} = 0 \tag{2.38}$$

We can break this up into time and spatial components and differentiate with respect to time to get

$$\frac{\partial^2 T^{00}}{\partial t^2} = \frac{\partial^2 T^{ij}}{\partial x^i \partial x^j} \tag{2.39}$$

Multiplying this by $x^i x^j$ and integrating over all space, we get the relation:

$$\int d^3x T^{ij}(\boldsymbol{x}) = \frac{1}{2}\frac{d^2}{dt^2} \int d^3x x^i x^j T^{00}(\boldsymbol{x}) \tag{2.40}$$

To get the far-field approximation in Equation 2.36, we implicitly assumed that the wavelength of the radiation was large compared to the length scale of the source. This has the added caveat of implying that the source must be slowly varying, ie. the source is non-relativistic. We can safely assume that the total energy of the source $T^{00}(\boldsymbol{x})$ will be dominated by the rest-mass energy of the source $\mu(\boldsymbol{x})$. Making this substitution, and we have the definition of the second moment of the mass distribution:

$$I^{ij} = \int d^3x \mu(\boldsymbol{x}) x^i x^j \tag{2.41}$$

The far-field approximation for the gravitational wave metric can then be written as:

$$\overline{h}^{ij}(t, \boldsymbol{x}) \xrightarrow[r\to\infty]{} \frac{2G}{c^4 r}\frac{d^2}{dt^2} I^{ij}(t - r/c) \tag{2.42}$$

We actually want this in the transverse-traceless gauge, h_{ij}^{TT} as opposed to $\overline{h}^{ij}$. We do this with the projection operator

$$P_{lm} = \delta_{lm} - n_l n_m; \quad n_l = x^l/r \tag{2.43}$$

We transform the second moment of the mass distribution I_{ij} as

$$I_{ij}^{TT} = P_{il} I_{lm} P_{mj} - \frac{1}{2} P_{ij}(P_{lm} I_{ml}) \tag{2.44}$$

We go one step further by defining the reduced quadrupole moment

$$\not{I}_{ij} \equiv I_{ij} - \frac{1}{3}\delta_{ij} I \tag{2.45}$$

We can then write the perturbation metric in the transverse-traceless gauge

$$h_{ij}^{TT}(t, \boldsymbol{x}) = \frac{2}{r}\frac{d^2 \not{I}_{ij}^{TT}(t - r)}{dt^2} \tag{2.46}$$

2.1.6 Sources of Gravitational Waves. One of the most efficient emitters of gravitational radiation is an orbiting binary system. Let's consider two point masses m_1 and m_2 in the $x_1 - x_2$ plane orbiting at a constant distance from the origin r_1 and r_2, respectively. We define the orbital separation $a = r_1 + r_2$, the total mass $M = m_1 + m_2$, the angle $\varphi = \omega t$ between the x_1 axis and the position vector of mass m_1 and linearly increases in time, and the reduced mass

$\mu = m_1 m_2/M$. The non-zero components of the inertia tensor I_{ij} are shown in Equation 2.47.

$$\begin{aligned} I_{11} &= \frac{1}{2}\mu a^2 \left(1 + \cos 2\varphi\right) \\ I_{22} &= \frac{1}{2}\mu a^2 \left(1 - \cos 2\varphi\right) \\ I_{33} &= \frac{1}{2}\mu a^2 \sin 2\varphi \end{aligned} \tag{2.47}$$

Plugging these into Equation 2.46 (and restoring factors of G and c), we get Equation 2.48.

$$h_{ij}^{TT}(t, \boldsymbol{x}) = -\frac{4G\mu a^2\omega^2}{c^4 r} \begin{pmatrix} \cos 2\varphi & \sin 2\varphi & 0 \\ \sin 2\varphi & -\cos 2\varphi & 0 \\ 0 & 0 & 0 \end{pmatrix} \tag{2.48}$$

The two polarizations can be read from the tensor components to get Equation 2.49.

$$\begin{aligned} h_+ &= -\frac{4G\mu a^2\omega^2}{c^4 r}\cos 2\varphi \\ h_\times &= -\frac{4G\mu a^2\omega^2}{c^4 r}\sin 2\varphi \end{aligned} \tag{2.49}$$

The gravitational waves will be emitted at twice the orbital frequency $f_{GW} = \omega/\pi$. The GW polarizations are often written in terms of $\nu = a\omega$ which from Kepler's third law, can be written as $\nu = (\pi G M f_{GW})^{1/3}$. Equation 2.50 also include a geometric correction for off-axis observation, parameterized by the inclination angle ι.

$$\begin{aligned} h_+ &= -\frac{2G\mu}{c^2 r}\left(1 + \cos^2\iota\right)\left(\frac{\nu}{c}\right)^2 \cos 2\varphi \\ h_\times &= -\frac{2G\mu}{c^2 r}\cos\iota \left(\frac{\nu}{c}\right)^2 \sin 2\varphi \end{aligned} \tag{2.50}$$

We can get an order of magnitude estimate of what this looks like in a more tangible scenario. Consider two 25.0 $M_\odot$ objects in a circular binary system separated by 200 km at a distance of 30 Mpc from our detector and optimally oriented ($\iota = 0$). This gives a dimensionless strain of approximately 2.9×10^{-20} at about 290 Hz.

2.1.7 The First Detection of Gravitational Waves.

Theory was finally realized in September 2014, gravitational waves were observed from a binary black hole merger (B. Abbott et al., 2016b). This was the start of the first observing run (O1), which ran until January 12 2016 with an angle-averaged BNS sensitivity range of 80 Mpc. The second observing run (O2) began on November 30, 2016 and ran until August 25, 2017, with the Virgo detector joining briefly near the end (the LIGO detectors reached a BNS sensitivity of around 100 Mpc and Virgo reached about 30 Mpc). The third observing run began on April 1, 2019, took a commissioning break during October 2019, and ran until March 26, 2020, ending prematurely due to the COVID-19 pandemic. O3 sensitivity ranged from $100 - 140$ Mpc for the LIGO detectors and $40 - 50$ Mpc for the Virgo detector. The fourth observing run (O4) began on May 24, 2023 and is currently underway. The LIGO detectors are reaching a sensitivity of $150 - 160$ Mpc and Virgo is reaching $50 - 80$ Mpc. This timeline is represented graphically in Figure 2.

Since observation began, many more events have been detected, and by the end of O3, 90 total candidates had been reported (B. Abbott et al., 2019; R. Abbott et al., 2021d, 2023, 2024a). All of these detections have been some form of compact object binary inspiral, be it a standard binary black hole merger (BBH), a binary neutron star merger (BNS) (B. P. Abbott et al., 2017b), or a black hole and a neutron star (NSBH) (R. Abbott et al., 2021e).

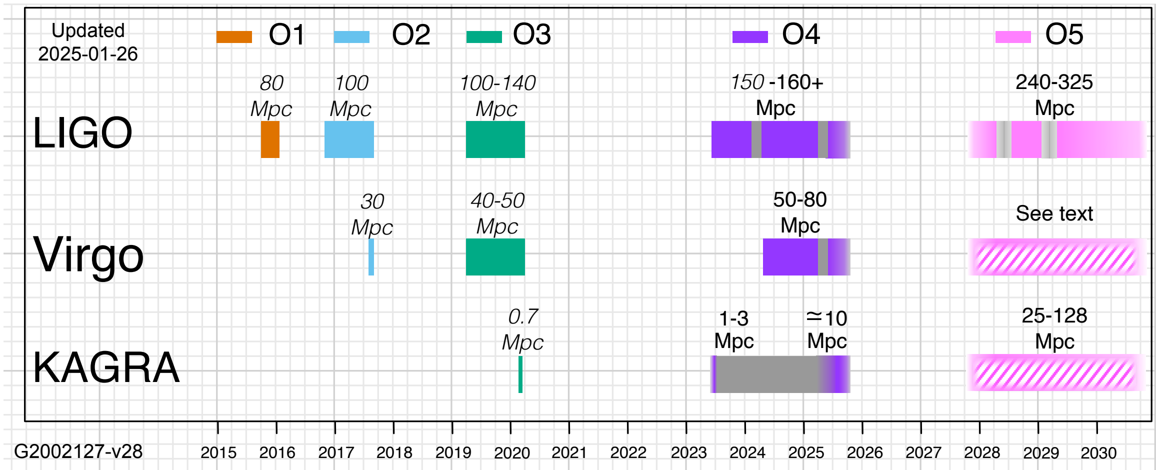

Figure 2. Timeline of the LIGO observing runs with approximate sensitivity ranges (Shoemaker, Arnaud, & Sawada, 2025). Breaks during observing runs are marked in gray. Also included are the observing timelines for the Virgo detector in Italy and the KAGRA detector in Japan.

2.1.8 Other Astrophysical Sources of Gravitational Waves.

Sources of gravitational radiation are typically organized into categories based on the duration of the signal (Creighton & Anderson, 2011; K. Thorne, 1987). Signals where the emission is characterized by only a few cycles are referred to as *bursts*. Signals consisting of a few discrete frequencies persisting for a long duration are referred to as *continuous waves* (CWs). Signals consisting of many, incoherent frequencies persisting for a long duration are referred to as *stochastic* signals.

2.1.8.1 Burst Sources. Burst sources include a variety of potential astrophysical phenomena. Modern LIGO searches consider binary inspirals (see eg. R. Abbott et al. (2023)), supernovae (B. Abbott et al., 2016a, 2020), cosmic string interactions (Aasi et al., 2014; B. Abbott et al., 2018; B. P. Abbott et al., 2009; R. Abbott et al., 2021c), and oscillatory modes from isolated neutron stars (see eg. R. Abbott et al. (2021b, 2024b)). While these are all fascinating fields, in this thesis, I will focus on the signals from isolated neutron stars.

2.1.8.2 Continuous Wave Sources. One of the simplist sources one can imagine for a system with a non-zero second derivative of the moment of inertia is a spinning nearly rotationally symmetric system either speeding up or slowing down. At lower frequencies (below a few Hz), the primary example of this are binary systems where the binary partners are quite distant from each other (such that the orbital frequency remains relatively stationary). At frequencies in the LIGO sensitivity band, the primary system is a rotating, non-axisymmetric neutron star (Creighton & Anderson, 2011). Like burst sources, these types of signal would originate from singular sources, and thus many searches for these sources are targeted at known objects (see eg. R. Abbott et al. (2022b)).

2.1.8.3 Stochastic Sources. Long-duration signals that are not a discrete set of coherent frequencies may be described as stochastic. The primary stochastic GW source is a gravitational wave background (GWB). This background falls into two categories: isotropic and anisotropic. An isotropic GWB would be Gaussian, unpolarized, and stationary. This would be characterized by some background GW energy density spectrum. An anisotropic GWB would be directional, where the background energy originates from some set of locations, or is non-uniform in source location. In this case, the GWB would be characterized by a similar energy density spectrum, but it would also be dependent on the source location. LIGO has previously searched for both isotropic (R. Abbott et al., 2021f) and anisotropic (R. Abbott et al., 2022a) backgrounds, with no candidates so far. However, evidence for a GWB has ben found using pulsar timing arrays (Agazie et al., 2023), though this is in a much lower frequency band than the LIGO detectors are sensitve to.

A possible source for an isotropic GWB background would be some distribution of individual sources, such as binary black hole mergers, which cannot be distinguished and instead sum together into a "popcorn" background.

2.2 Gravitational Wave Interferometry and LIGO

At the end of Section 2.1.6, I gave a simple, but somewhat realistic, example of the approximate strain for a binary system in a circular orbit. With the binary optimally oriented, we required a background strain below 10^{-20} at approximately 300Hz. I will use this as a target sensitivity for this discussion.

2.2.1 The LIGO Detectors and Measuring Gravitational Waves with Laser Interferometry.

To measure fluctuations in spacetime at such a small scale, a device capable of measuring small variations in distance is necessary. Early designs of GW detectors considered measuring the strains within bulk matter due to the gravitational radiation (Weber, 1960). This was expanded upon into the first network of resonant-mass detectors which relied on the gravitational radiation exciting a resonant mode of a solid metallic cylinder (Allen et al., 2000). These early detectors did not reach the sensitivities necessary to successfully measure gravitational waves. An improved detector would use laser interferometry to determine if spacetime had been expanded or contracted. This discussion closely follows that in Creighton and Anderson (2011).

We start with the simple Michelson interferometer where a laser is split down two orthogonal arms to distant mirrors and reflected back. The reflected beams recombine and interfere with each other based on the difference in optical path lengths of the two arms. Consider a Michelson interferometer with two arms of identical length. The effect of a gravitational wave on this setup will be the asymmetic contraction/expansion of the arms, creating a difference in optical path.

If we call this optical path difference Δl and the length of the arms l, then the metric perturbation will be $h = \Delta l / l$. A measurable path length difference will be on the scale of a single wavelength of light, so if we assume an infrared laser with a wavelength of 1μm and arm lengths of 1 km then we can estimate the sensitivity of the interferometer to be about 10^{-9}, which is far below what is required to measure the effect of gravitational waves.

We can improve this in two ways: increase the effective arm length and reduce the minimum measurable length difference. There is a maximum arm length such that the gravitational metric does not significantly change during the time a photon is traveling. This gives an upper limit on the arm length of $l \sim \lambda_{GW}$, which is about 1000 km for $f_{GW} = 300\,\text{Hz}$. From a design point, building a 1000 km arm is not feasible, but creating an optical cavity such that photons bounce back and forth several times along the arm is. This is a Fabry-Pérot cavity, and relies on creating a 'locked' resonant state within the arms. Our interferometer has test mass mirrors at both the end of the arms and at the beginning of the arms to create this cavity. The measurement of the length difference is limited by the ability to measure the interference - ie. what is the smallest difference in the interference pattern that can be measured. The limitation here is shot noise. For a digital readout, a sensor will count incident photons for a discrete amount of time. The photon arrival rate is a Poisson process, so confident measurements require greater than $N_{\text{photons}}^{1/2}$ measured. This gives an approximate optical path difference of

$$\Delta l \sim \frac{N_{\text{photons}}^{1/2}}{N_{\text{photons}}} \lambda_{\text{laser}}. \tag{2.51}$$

To measure a gravitational wave with sample rate $f_s \sim f_{GW} \approx 300\,\text{Hz}$ from a laser with power P_{laser}, we collect approximately

$$N_{\text{photons}} \sim \frac{P_{\text{laser}}}{hc/\lambda_{\text{laser}}} \frac{1}{f_{GW}} \tag{2.52}$$

photons. For a 1 W laser at a wavelength of $\lambda_{\text{laser}} = 1\,\mu\text{m}$, this gives $N_{\text{photons}} \approx 10^{16}$ photons. This gives an approximate strain sensitivity of 10^{-20}, which is much closer to the target strain level.

There are a few more features that can improve a real detector. Since the reflected beams in each arm recombine at the beam splitter, half of that light will travel back towards the laser source. A power recycling mirror can reflect some of that back into the interferometer. Quantum shot noise can be reduced by introducing quantum squeezing. Higher laser power adds more photons to improve the shot noise as well. Figure 3 shows a schematic layout of the Advanced LIGO detector layout with many of the features discussed in this section (The LIGO Scientific Collaboration, 2015).

2.2.2 Sources of Noise in the LIGO Detectors. The LIGO noise curve is dominated by a few key sources of background. Here, we will briefly discuss a handful of the major ones. At high frequencies, the main limiting factor is quantum noise. This encompasses both the statistical uncertanties in photon arrival times (known as shot noise) and radiation pressure fluctuations due to variations in photon number. At intermediate frequencies, the background is dominated by coating Brownian noise in the test masses. This is due to the Brownian motion of molecules in the coating layers applied to the test masses (Creighton & Anderson, 2011; The LIGO Scientific Collaboration, 2015). Figure 4 shows how the sum of many of the dominant noise sources creates the signature "bucket" shape of the LIGO noise curve.

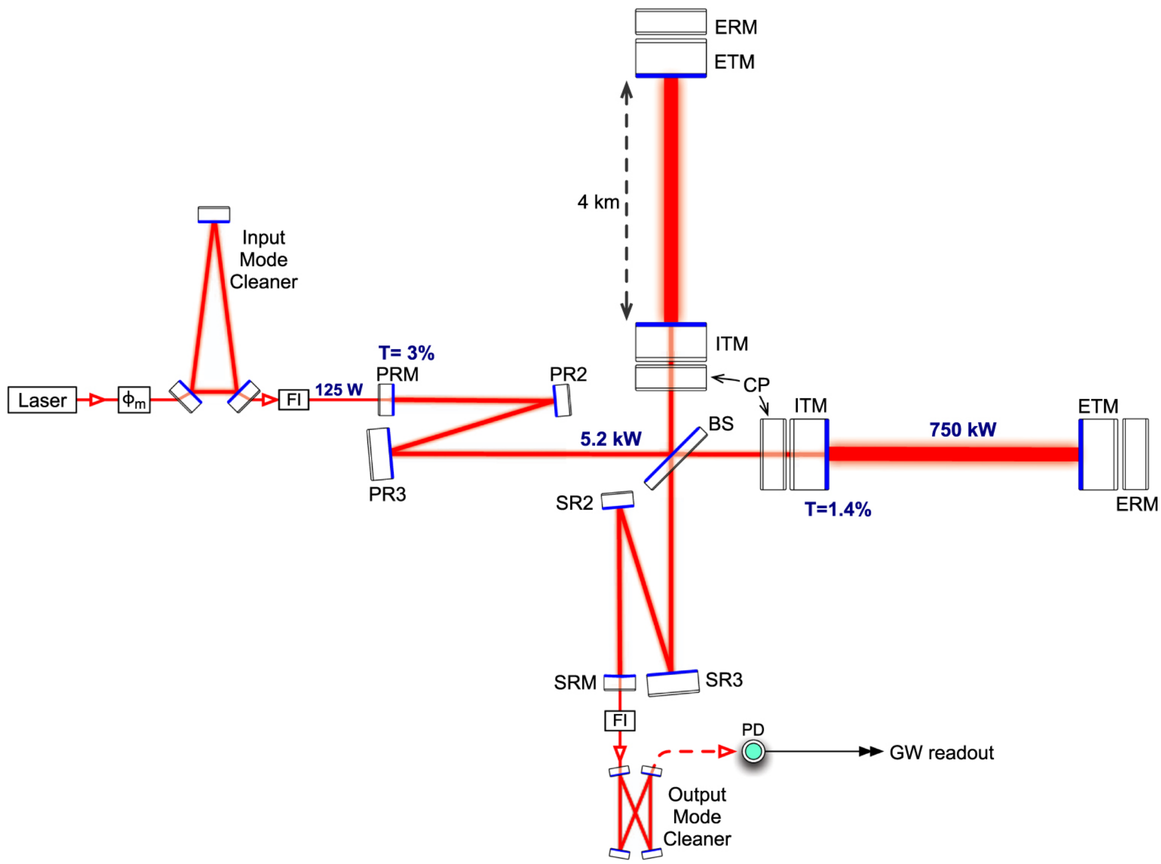

Figure 3. Schematic of the aLIGO layout going into the third observing run. Notable sections include the 4 km Fabry-Perot cavities in each arm, the input mode cleaner and output mode cleaner to remove higher-order modes in the beam, the power recycling cavity, and the signal recycling cavity. Image from The LIGO Scientific Collaboration (2015).

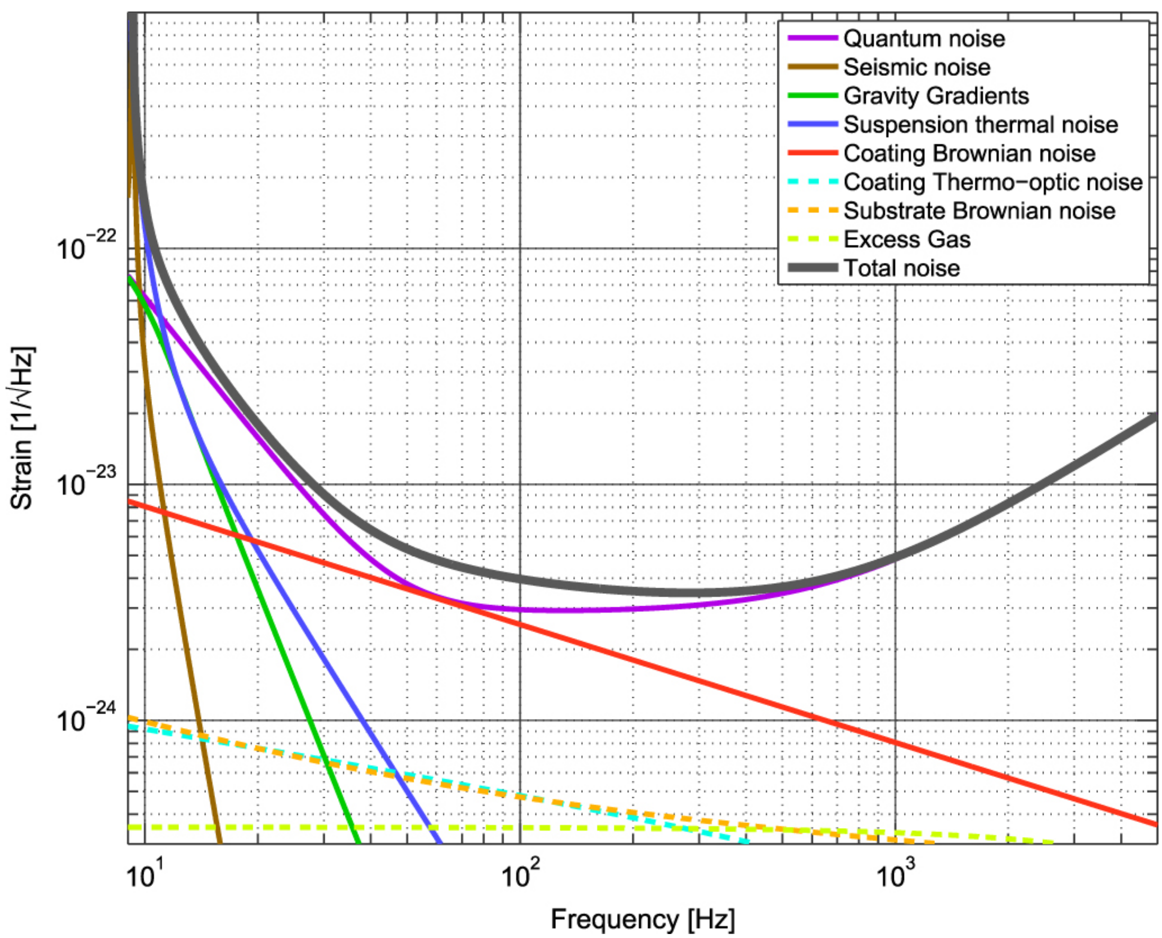

Figure 4. Sum of the dominant noise sources in aLIGO. These effects are the primary reason for the "bucket" shape of the noise curve. Image from The LIGO Scientific Collaboration (2015).

Many sources of noise are not necessarily intrinsic to the detector. Environmental effects can place significant limits on the sensitivity of the detector. One of the major ones is seismic noise caused by the propagation of vibrations through the ground. This primarily affects the low frequency regime of the detectors (as seen in Figure 4). This is primarily mitigated by a quadruple suspension system for the mirrors (Figure 5[1]). Due to the potential impact, it is necessary to monitor environmental effects in order to prevent false positives and ideally eliminate environmental contamination. An array of auxillary sensors around the detectors monitor seismic activity via seismomenters, the movement of individual components via accelerometers, acoustic effects via microphones, magnetic field effects via magnetometers, voltages via voltmeters, as well as wind speed, humidity, and even cosmic rays (Effler et al., 2015; Nguyen et al., 2021).

2.3 Isolated Neutron Stars as Sources of Gravitational Waves

One potential source of both continuous wave and burst-like gravitational waves is an isolated neutron star. The extreme internal dynamics of a neutron star creates an environment where large amounts of stress and potential energy can be built up and potentially released through the emission of gravitational waves. The precise internal dynamics are dictated by the relationship between the energy density and the internal pressure, which is known as the *equation of state.* The two main categories of neutron stars I consider are *magnetars* and *pulsars.*

2.3.1 Neutron Star Equation of State. The behavior of the material inside of a neutron star is dictated by the equation of state. At a fundamental level, this describes how the material behaves under pressure. More specifically, the equation of state describes the relationship between the pressure

[1] Image from `https://www.ligo.caltech.edu/page/ligo-technology`, modified from (Aston et al., 2012).

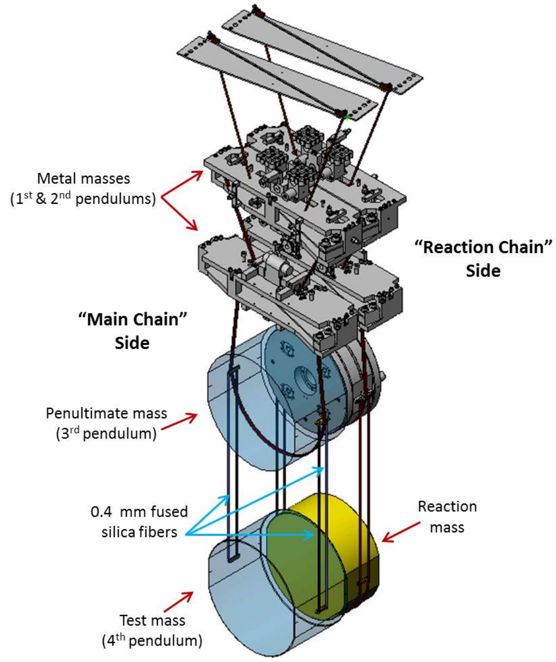

Figure 5. Quadruple suspension system for the LIGO mirrors (Aston et al., 2012).

and energy density, $P(\rho)$. Since the extreme density of a neutron star will create enormous pressures, the precise details of these relations can have significant effects on the global structure of the star. Neutron star equations of state can be categorized in several ways. One of the simplest is "hot" vs "cold," corresponding to an assumption of finite temperature or zero temperature, respectively. Hot equations of state are typically intended to describe newly born stars, whereas older, stable stars are typically described as cold. For the stable neutron stars we will discuss, cold equations of state will be appropriate. Equations of state are also typically described as "hard" or "soft." A neutron star with a hard (soft) equation of state would have a greater (smaller) pressure at a given energy density, leading to larger (smaller) radii and larger (smaller) maximum masses (Sumiyoshi, Kojo, & Furusawa, 2023).

2.3.2 Magnetars.

A subclass of neutron stars with exceptionally strong magnetic fields ($> 10^{14}G$) are referred to as magnetars (Duncan & Thompson, 1992). While their formation mechanism is debated (Ferrario, Melatos, & Zrake, 2015; Mereghetti, Pons, & Melatos, 2015), a prominent theory suggests that they may be formed by the collapse of highly magnetized Wolf-Rayet stars (Shenar et al., 2023). First known as soft gamma repeaters due to their regular emission of X- and γ-rays (Mazets & Golenetskii, 1981; Mazets, Golenetskij, & Guryan, 1979; Mazets, Golentskii, Ilinskii, Aptekar, & Guryan, 1979), magnetars are now known to be a subclass of neutron star, with 30 [2] known and categorized at the time (Olausen & Kaspi, 2014).

Magnetars are known for the bursts of X-rays they can emit. These bursts, or flares, are believed to be due to interactions between the strong magnetic field and the exotic matter in the interior (Thompson & Duncan, 1996). These flares can have isotropic energies of 10^{36} to 10^{43} ergs (Kaspi & Beloborodov, 2017), and some exceptionally large flares, simply referred to as giant flares, can have energies of 10^{44} to 10^{46} ergs (Hurley et al., 2005, 1999; Mazets, Golentskii, et al., 1979). However, these giant flares are much rarer. The light curve of the 2004 giant flare from SGR 1806-20 as measured by the Swift Burst Alert Telescope (BAT) is shown in Figure 6 (Palmer et al., 2005).

The unknown connection between these large flares and the internal structure of the stars leaves room for interpretation. At least for giant flares, theory suggests that magneto-hydrodynamic deformation in the interior of the star may release built up stress and release the energy into the magnetosphere through crust-cracking (de Freitas Pacheco, 1998; Levin & Van Hoven, 2011; Thompson &

[2] http://www.physics.mcgill.ca/ pulsar/magnetar/main.html

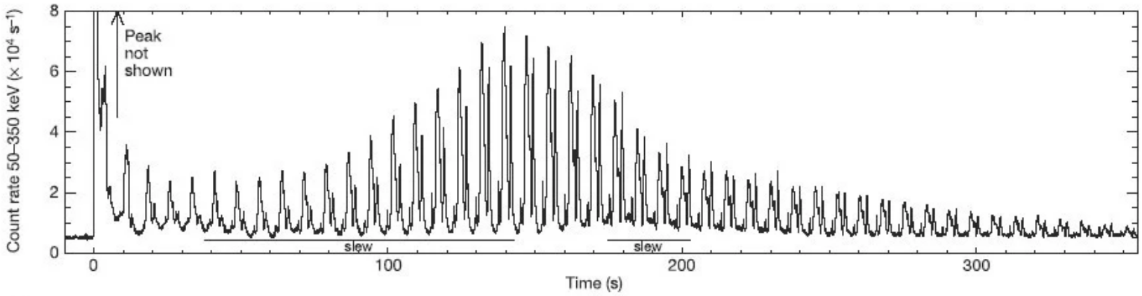

Figure 6. Swift BAT count rate for the 2004 giant flare from SGR 1806-20 (Palmer et al., 2005). The peak amplitude was large enough that it saturated the BAT sensor.

Duncan, 1995). The internal reconfiguration could potentially release energy both through the flaring as well as gravitational waves (Corsi & Owen, 2011; Ioka, 2001).

While no gravitational waves have ever been measured near a magnetar flare (B. P. Abbott et al., 2019; R. Abbott et al., 2024b), a variety of potential emission forms have been suggested. The most anticipated form is that from the vibration of excited fluid pressure modes. The fundamental mode (f-mode) is the lowest order of the non-radial oscillations and is predicted to have the strongest coupling to gravitational wave emission (McDermott, Van Horn, & Hansen, 1988). It should be monochromatic at a few kHz (de Freitas Pacheco, 1998; Lindblom & Detweiler, 1983), and be short lived (Levin, 2006). Other types of GW emission, while predicted to be smaller in amplitude, include higher order pressure modes (p-modes) (Andersson & Kokkotas, 1998), much higher frequency buoyancy modes (g-modes) (Reisenegger & Goldreich, 1992), lower frequency crustal and shear modes (Duncan, 1998; Piro, 2005), and the longer duration Alvén plasma modes below 1 kHz (Lasky, Zink, & Kokkotas, 2012). These Alvén modes are of interest due to the similarity between the expected frequency and observed quasi-periodic oscillations (QPOs) observed in the tails of some magnetar flares.

2.3.3 Pulsars.

Pulsars are a class of rapidly rotating neutron stars characerized by, from the perspective of an observer on Earth, periodic radio emission. First measured in 1967, the periodic behavior was believed to be due to pulsations within a compact object such as a neutron star or white dwarf (Hewish, Bell, Pilkington, Scott, & Collins, 1968). This hypothesis was rejected by Pacini (1967), who argued that pulsations within a neutron star would damp out in a few seconds due to gravitational radiation; the periodic behavior should instead be due to a constant EM emission from a rotating object, such that the emission would only periodically point at the observer. This was later confirmed by observations of the Crab pulsar (Gold, 1968).

Since then, the periodic behavior of hundreds of pulsars are tracked by regular observation from radio telescopes, and their rotation rates can be very precisely measured (Kaspi, Taylor, & Ryba, 1994; Ryba & Taylor, 1991a, 1991b). Continuous measurements of these objects has allowed for significant advancements in understanding neutron star properties. Pulsars in binary systems are subject to relativistic effects. Some of the first measurements of neutron star masses are due to measuring the Shapiro delay of the pulses due to the companion object (Ryba & Taylor, 1991a). This technique has been one of the most reliable methods to place constraints on the mass of neutron stars. Recently, more advanced implementations of this techinque have made measurements of the largest recorded neutron star at $2.35 \pm 0.17 M_{\odot}$ (Romani, Kandel, Filippenko, Brink, & Zheng, 2022).

While the rotation of pulsars can be very consistent, many pulsars experience sudden changes in rotation rate, referred to as "glitches" (Fuentes et al., 2017; Haskell & Melatos, 2015; Zhou, Gügercinoğlu, Yuan, Ge, & Yu, 2022). In a glitch, the rotation rate of the pulsar suddenly jumps and is followed by an accelerated spindown rate until it returns to nearly the original rate. These jumps are typically parameterized in terms of the fractional change in the rotation rate ($\Delta f/f$) and can range from roughly 10^{-10} to 10^{-6} [3] (Basu et al., 2021). These glitches are unique among known neutron star transient events, in that they are not associated with a change in the radiation properties - the pulses before and after a glitch are still very similar. This is unlike observed glitches in magnetars, which are typically associated with some sort of EM emission (Keith, Shannon, & Johnston, 2013; Livingstone, Ng, Kaspi, Gavriil, & Gotthelf, 2011; Lyne, Hobbs, Kramer, Stairs, & Stappers, 2010; Weltevrede, Johnston, & Espinoza, 2011).

There are a handful of models that attempt to explain the origin of these glitches, all of which depend on the internal structure of the pulsar. One of the earlier models suggested that the outer layers of the neutron star crust form a rigid crystalline structure as opposed to a more fluid interior. As the pulsar slowly spins down, the fluid interior is able to adapt to the change, but the rigid crust does not, and subsequently experiences discrete star quakes as it restructures itself (Ruderman, 1969; Smoluchowski, 1970).

A more modern model considers the interior as a superfluid, created by the intense pressures within the star. A superfluid exhibits little to no viscosity, so interior changes can take a long time to propagate to the surface, which would explain the long glitch recovery times observed (Baym, Pethick, Pines, & Ruderman, 1969). One key property of superfluids is that they are irrotational, and circulation is presented as quantized vortices. For angular momentum to be lost, a discrete number of vortices must be lost. This more modern model suggests that interactions with the crust "pin" the vortices and prevent movement. This

[3] http://www.jb.man.ac.uk/pulsar/glitches.html

prevents the loss of angular momentum from the superfluid, which ultimately leads to unpinning events, which present as glitches (Alpar, Pines, Anderson, & Shaham, 1984; Anderson & Itoh, 1975).

Pulsar glitches are thought to be sources of multiple types of transient gravitational waves. These fall into two main categories: short duration bursts caused by the initial jump in spin rate, and long duration waves caused by the slow emission associated with the long recovery time measured in EM. The short bursts are typically considered to be f-modes (Andersson & Kokkotas, 1998; Ho, Jones, Andersson, & Espinoza, 2020; Wilson & Ho, 2024; Yim & Jones, 2022). These are the same high-frequency, short-duration signals discussed in Section 2.3.2. The long duration transients are predicted to arise from either an Ekman flow driven mechanism (Bennett, Van Eysden, & Melatos, 2010; Singh, 2017; Van Eysden & Melatos, 2008) or due to the decay of an induced ellipticity, known as a "mountain" (Yim & Jones, 2020).

Searches have been performed for both classes of GW emission but with no success. One of the first targeted GW searches was from the 2006 Vela glitch (Abadie et al., 2011b). For various reasons, there have not been other targeted searches for short duration GWs associated with pulsar glitches. However, there have been more recent searches for long duration transients (R. Abbott et al., 2022c; Keitel et al., 2019), also with no detections.

CHAPTER III

DETECTOR CHARACTERIZATION

3.1 On-Site Detector Work

In the summer of 2019, I was a Fellow at the LIGO Hanford observatory. During this time, I worked on several day-to-day tasks as well as two major projects: working with the commissioning team to mitigate angular cross-coupling in the quadruple pendulum suspensions and working with Robert Schofield to identify and mitigate a mysterious 48 Hz noise peak in the spectrum.

3.1.1 Angular Cross-Coupling Modeling. The LIGO quadruple pendulum suspensions (see Figure 5 for a schematic diagram of the suspensions) are intended to reduce environmental vibrational noise from reaching the test mass (TST). In order to maintain stability, the calibration feedback loop involves pushing on the penultimate mass (PUM). This can introduce unexpected effects due to to the construction of the suspensions. Mitigating movement along some degrees of freedom can couple with others, introducing instabilities and unwanted noise. In particular, we looked at reducing the effect of linear motion of the PUM along the beam line (referred to simply as "length") on pitch angular motion of the TST, the effect of pitch motion of the PUM (referred to simply as "angle") to length motion of the TST, and the potential advantages of changing the frequencies of the active dither system (ADS) lines injected for calibration.

The LIGO control loops employ a series of digital filters in order to remove unwanted cross-coupling between different stages of the quadruple suspensions. However, these filters in conjunction with complicated coupling dynamics, can introduce unwanted features and instabilities in the detector. One particular set of filters was intended to mitigate motion generated in the upper intermediate mass

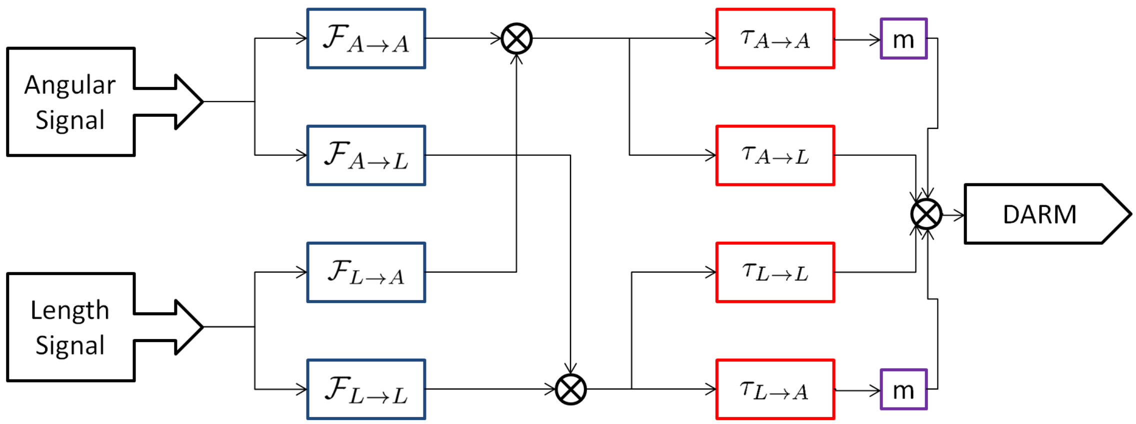

Figure 7. Schematic diagram of the old drive-align system. Digital filters are marked in blue, and mechanical transfer functions are marked in red. The scalar offset of the beam spot is marked in purple.

(UIM) that crosses over into the PUM but actually adds instabilities to the control loop. These instabilities are created by a parasitic "length-to-angle-to-length coupling" where linear motion in an upper stage causes both linear and angular motion in the test mass, and when filters push on the upper mass they introduce additional linear and now angular motion in the upper stage which couples further to the test mass (Driggers, 2019).

The general structure of the coupled feedback loop (referred to as the "drive-align system") at the start of the third observing run is shown in Figure 7, where $\mathcal{F}(f)$ are digital filters, $\tau(f)$ are mechanical transfer functions, and m is the linear offset of the main laser.

In practice, the beam offset m was larger than anticipated, magnifying the effect of TST angular motion on DARM. The simple approach to resolve this was to have a large scalar value for $\mathcal{F}_{A\to L}$ to compensate. This increased the effect of angular signals, but the location of the $\mathcal{F}_{L\to A}(f)$ filter did not balance this increase on the length scales, creating instabilities. Additionally, the $\mathcal{F}_{L\to A}(f)$ filter was not designed with large beam offsets in mind, so this added extra instabilities. Ultimately the $\mathcal{F}_{L\to A}(f)$ filter was disabled entirely in order to have a stable interferometer at the cost of cross-coupling. We can describe the coupling from PUM motion to DARM as simply $C_{L\to DARM} = \mathcal{F}_{L\to L}(f) \times \tau_{L\to L}$ under this regime.

In Kissel and Dwyer (2019), two fixes were proposed:

- Redirect the output of the $\mathcal{F}_{L\to A}(f)$ filter into the angular signal input, thereby feeding it into the $\mathcal{F}_{A\to L}$ and $\mathcal{F}_{A\to A}(f)$ directly. This would help to reduce instability by balancing the angular effect of a large beam offset with an appropriate length effect.
- Split the $\mathcal{F}_{A\to L}$ filter into the sum of a scalar spot-position term and a frequency-dependent term to improve decoupling.

3.1.1.1 Length-to-Angle Rerouting. The rerouted drive-align system is shown in Figure 8. Rather than just combining the effects of the $\mathcal{F}_{A\to A}(f)$ and $\mathcal{F}_{L\to A}(f)$ filters, the output of the $\mathcal{F}_{L\to A}(f)$ filter is fed into both the $\mathcal{F}_{A\to L}$ and $\mathcal{F}_{A\to A}(f)$ filters.

The cross-coupling between PUM linear motion and DARM motion under the new geometry can be described by Equation 3.1, where $\mathcal{F}(f)$ are digital filters, $\tau(f)$ are mechanical transfer functions, and m is the linear offset of the main laser. Clearly, the new geometry is a bit more complex!

$$\begin{aligned} C_{L\to DARM} = {} & \mathcal{F}_{L\to A}(f)\left[\mathcal{F}_{A\to A}(f)\left(\tau_{A\to L} + \tau_{A\to A} m\right) + \mathcal{F}_{A\to L}(f)\left(\tau_{L\to L} + \tau_{L\to A} m\right)\right] \\ & + \mathcal{F}_{L\to L}(f)\left(\tau_{L\to L} + \tau_{L\to A} m\right) \end{aligned} \tag{3.1}$$

We performed an initial test of this rerouting framework during a short maintenance window. We tested the change for both pitch and yaw angular motion

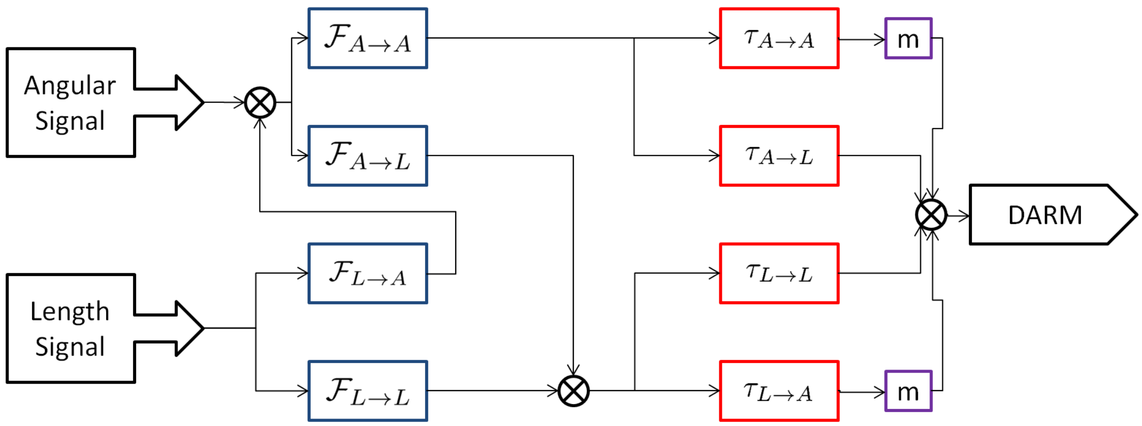

Figure 8. Schematic diagram of the new drive-align system with the $\mathcal{F}_{L\to A}$ rerouting in place. Digital filters are marked in blue, and mechanical transfer functions are marked in red. The scalar offset of the beam spot is marked in purple.

to see how stability of the interferometer would change. During this test, the detector maintained a locked state, something that may not have occurred using the old regime (Ball & Dwyer, 2019). We further tested this new topology with a low-frequency "boost" at the UIM suspension stage actuator intended to reduce actuation in the PUM associated with lockloss events associated with saturation at this stage. Figure 9 shows a timeseries the PUM stage motion when the boost was tested, showing a reduction in PUM motion after the boost was activated at time -923.192.

Calibration measurements taken with the new topology and the UIM boost show the elimination of the low-frequency instability (see Figure 10 taken from Kissel (2019)). The new topology allows for a non-zero frequency-dependent $\mathcal{F}_{L\to A}(f)$ filter while removing instabilities it formerly introduced.

3.1.1.2 Angle-to-DARM Filter Improvement. In either topology, the cross-coupling between PUM angular motion and DARM motion is given by Equation 3.2.

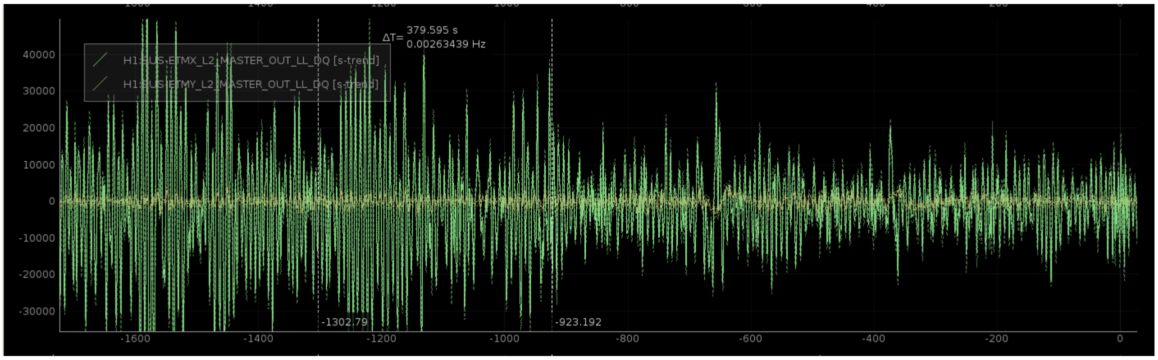

Figure 9. Timeseries of PUM actuation before and after the activation of a low-frequency "boost" at the UIM stage. The boost was activated at the vertical dotted line halfway through the plot – marked as -923.192.

$$C_{A\to DARM} = \mathcal{F}_{A\to A}(f)\,(\tau_{A\to A}m + \tau_{A\to L}) + \mathcal{F}_{A\to L}(f)\,(\tau_{L\to A}m + \tau_{L\to L}) \tag{3.2}$$

To completely eliminate this unwanted cross-coupling, the ideal representation of $\mathcal{F}_{A\to L}(f)$ is given by Equation 3.3

$$\mathcal{F}_{A\to L,\,ideal}(f) = -\frac{\mathcal{F}_{A\to A}(f)\,(\tau_{A\to A}(f)m + \tau_{A\to L}(f))}{\tau_{L\to A}(f)m + \tau_{L\to L}(f)} \tag{3.3}$$

Unfortunately, the dependence on the beam spot spot miscentering m is non-trivial. A more usable scenario would be a linearized version of the form $\mathcal{F}_{A\to L}(f) = \mathcal{F}_a(f)m + \mathcal{F}_b(f)$, where there are two separate frequency-dependent filters. This is optimal to easily change the filter as the beam spot offset m may change. To first order, the ideal filter can be expressed as in Equation 3.4.

$$\mathcal{F}_{A\to L,\,real}(f) = -\frac{\mathcal{F}_{A\to A}(f)\tau_{A\to A}(f)}{\tau_{L\to L}(f)}m - \frac{\mathcal{F}_{A\to A}(f)\tau_{A\to L}(f)}{\tau_{L\to L}(f)} \tag{3.4}$$

The $\mathcal{F}_{A\to A}$ filter is already in use in the feedback system, and estimates of the suspension transfer functions can be computed using a numerical model of the

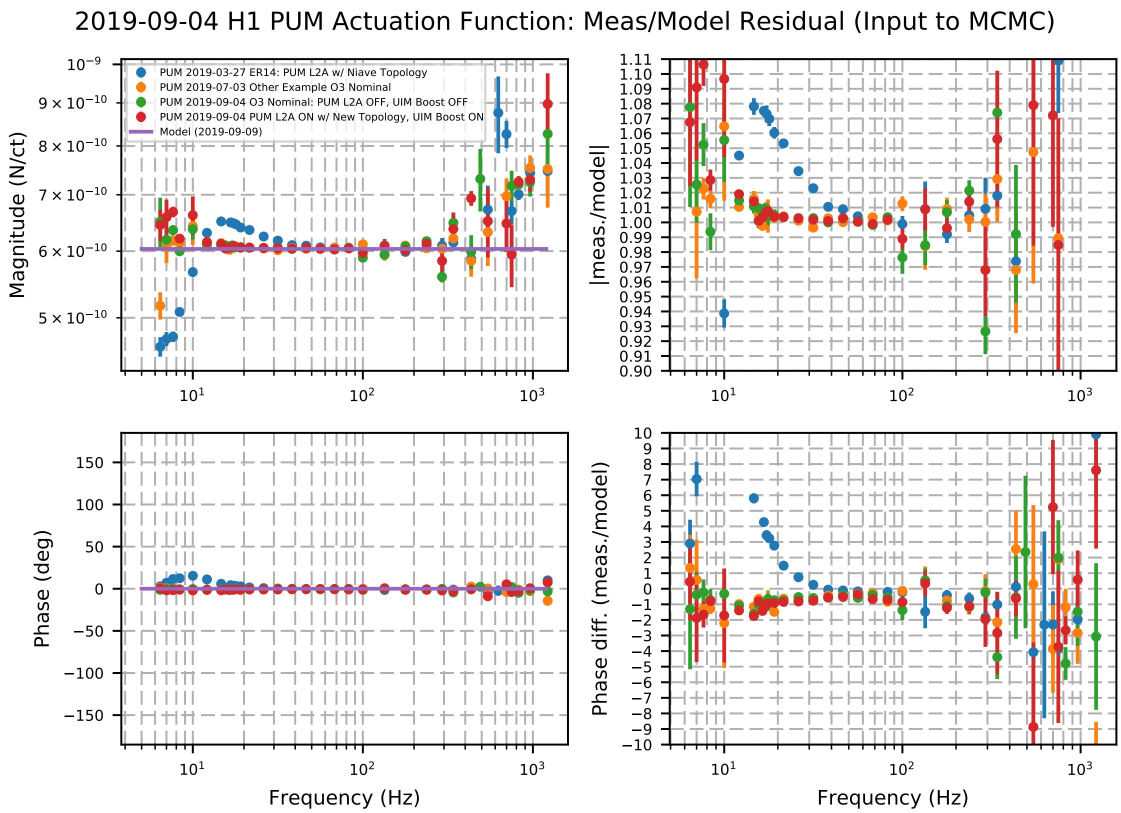

Figure 10. Calibration measurements taken by Jeff Kissel comparing measurements of the DARM feedback loop to the calibration model estimate of PUM actuation with and without the re-routed length-to-angle topology. Measurement of the original topology with the old frequency-dependent $\mathcal{F}_{L\to A}(f)$ is marked in blue, showing the low-frequency instability that emerges due to the beam spot position. A measurement of the original topology with $\mathcal{F}_{L\to A} = 0$ is shown in orange, showing early attempts to remove the instability. A more recent measurement of the same scenario is shown in green. Measurement of the new topology with the old frequency-dependent $\mathcal{F}_{L\to A}(f)$ and the UIM boost activated is shown in red. The re-routed topology eliminates the low-frequency instability and allows a non-zero frequency-dependent $\mathcal{F}_{L\to A}(f)$.

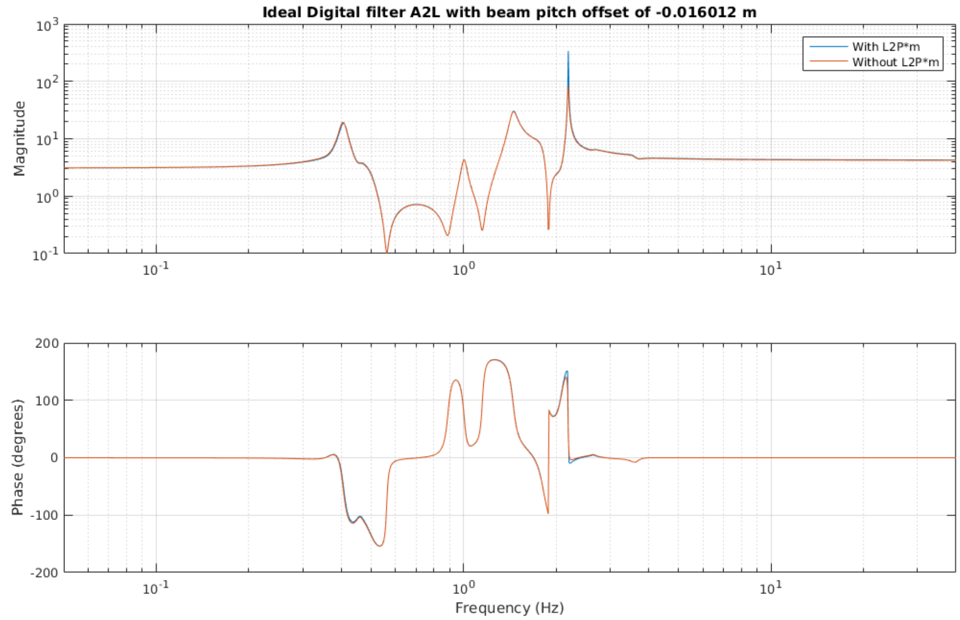

Figure 11. Frequency (top) and phase (bottom) shape of the ideal $\mathcal{F}_{A\to L}(f)$. Both the ideal and linearized versions are shown with functionally no difference. Here, we used a beam offset of $m = -0.016012\,\mathrm{m}$ which was the beam offset at the time.

suspension systems. Here, we used a version in MATLAB initially developed for GEO 600 by Torrie (2000) and updated for advanced LIGO (Barton, Torrie, Strain, & Robertson, 2012). Using this model, we can compute the transfer function for any degree of freedom between any suspension level. We use this to estimate $\tau_{A\to A}(f)$, $\tau_{A\to L}(f)$, $\tau_{L\to A}(f)$, and $\tau_{L\to L}(f)$.

With all of the pieces, we compute a frequency-dependent $\mathcal{F}_{A\to L}$ filter as shown in Figure 11. Figure 12 shows the difference in the PUM pitch to DARM length cross-coupling with the previous scalar $\mathcal{F}_{A\to L}$ and the new frequency-dependent $\mathcal{F}_{A\to L}(f)$.

Despite the apparent success of the new filters, they were never activated while I was on-site. They were saved and ready to be deployed (Ball, 2019), but were never activated. When I finished my stay, the detector was about to go down

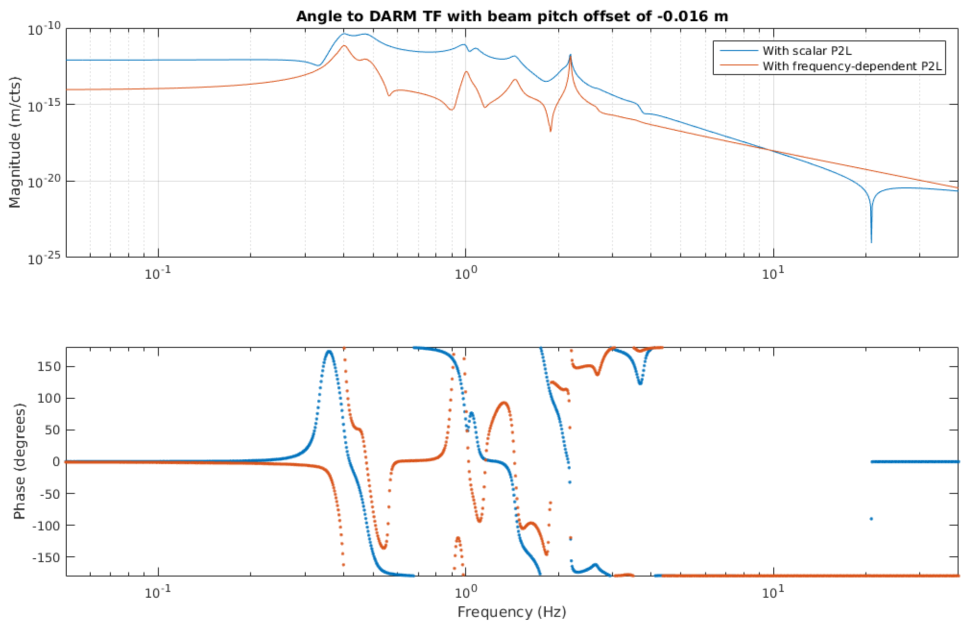

Figure 12. Comparison of the PUM angle to DARM cross-coupling with the old scalar scalar $\mathcal{F}_{A\to L}$ and the new frequency-dependent $\mathcal{F}_{A\to L}(f)$. The blue curve shows the cross-coupling when the $\mathcal{F}_{A\to L}$ filter was a scalar value. The orange curve shows the coupling when using the new frequency-dependent filter, demonstrating a significant decrease in the coupling below 10 Hz.

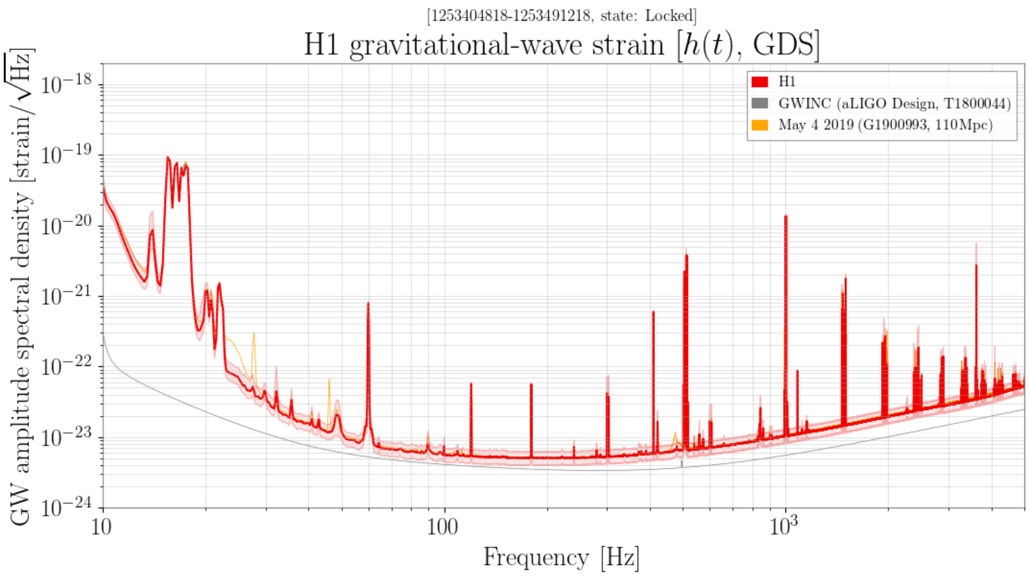

Figure 13. Daily gravitational wave amplitude spectral density from September 24, 2019 showing the "bump" at 48 Hz.

for a commissioning break at the midpoint of the third observing run. I later found out that the filters had been forgotten until the run-up to the fourth observing run, when they were finally activated (Kissel, 2022).

3.1.2 Mitigation of the 48 Hz Peak. In LIGO's 13th engineering run in the lead up to the third observing run, a new feature in the LHO detector spectrum was discovered. Elevated activity at 48.3 Hz and higher harmonics were discovered during the data quality shift that monitored detector output (Bidler, Smith, & Walker, 2018). At the time, this was seemingly ignored in lieu of monitoring other behaviors that resulted from detector upgrades. Later on, Fritschel (2019) re-discovered the 48 Hz peak along with its first harmonic at 96 Hz. They also noted that the feature was a wandering line, which varied up to a couple Hz in frequency on the timescale of a few seconds. The effect on detector sensitivity was quantified by Mansell (2019) to be about 2 Mpc. This feature is visible in the spectrum plot in Figure 13.

Initial investigations found that the peak could be excited acoustically and suggested that the source of the noise was near the vertex of the interferometer (Schofield, Nguyen, et al., 2019). These studies also found that the peak amplitude seemed to be correlated with times when the HVAC system was active.

My initial involvement with this work was to pursue the correlation with the HVAC system. I (along with fellow Oregon graduate student Adrian Helmling-Cornell) mounted temporary accelerometers on different pieces of the northern HVAC chiller units. Spectrograms of these accelerometers showed how the fans within these units stepped through different frequencies, and when compared to spectrograms of DARM, many of these frequency steps showed up directly overlapping the 48 Hz feature. Despite being mounted on springs to seismically isolate them, the units were still coupling into the interferometer (Schofield, Ball, Helmling-Cornell, & Warner, 2019). One initial solution was to change the frequency of the fans, to prevent them from stepping into the problematic frequency range. However, this quickly fell through when we learned the units were already in their low-noise configuration and there was no direct way to control what frequency the fans ran at (McCarthy, 2019).

The next approach was to address the coupling site and prevent this unwanted noise from getting into the interferometer. As mentioned above, previous studies had placed the coupling site near the vertex of the interferometer. To quickly narrow down the possible sites, we developed a new injection technique utilizing speakers and shakers operating at slightly different frequencies near 48 Hz to create a beat envelope. Figure 14 shows the two speakers and Figure 15 shows the two shakers. The two noise sources were separated such that there would be a location-dependent phase difference in the beat envelopes when viewed on an

(a) Small speaker (b) Big speaker

Figure 14. The two speaker set up in separate locations to produce beating.

accelerometer. The coupling point would then have an accelerometer beat envelope that temporally matched the beats in the gravitational wave readout.

We compared the beat envelopes of static accelerometers mounted around the vertex to initially find which vacuum chamber best matched DARM. This resulted in the HAM 3 chamber as the most likely coupling site. From there, multiple temporary accelerometers were mounted at various locations on the chamber to identify the precise spot where the coupling was occuring. As the coupling mechanism was already believed to be some sort of stray light reflecting off the chamber walls, this would identify where exactly said stray light was reflecting. Figure 16 shows the location of the final accelerometer that had the best match to the DARM beats along with spectrograms of the beat envelopes compared to DARM. The best matching accelerometer identified the coupling site

(a) Small shaker

(b) Big shaker

Figure 15. The two shakers mounted to the vacuum chambers

as the HAM 3 illuminator viewport (Schofield, Ball, Helmling-Cornell, Shoemaker, et al., 2019).

When we looked through the illuminator viewport, we found a milliwatt-scale "beam" directly hitting that spot. Stray light was hitting other parts of the chamber walls, including a second viewport. We inserted black glass into the illuminator viewport to prevent the stray light beam from reflecting back into the interferometer which entirely elliminated the 48 Hz peak (Helmling-Cornell, Ball, & Schofield, 2019; Schofield, Ball, Helmling-Cornell, Shoemaker, et al., 2019). Figure 17 shows the daily GW spectra after the removal of the 48 Hz peak.

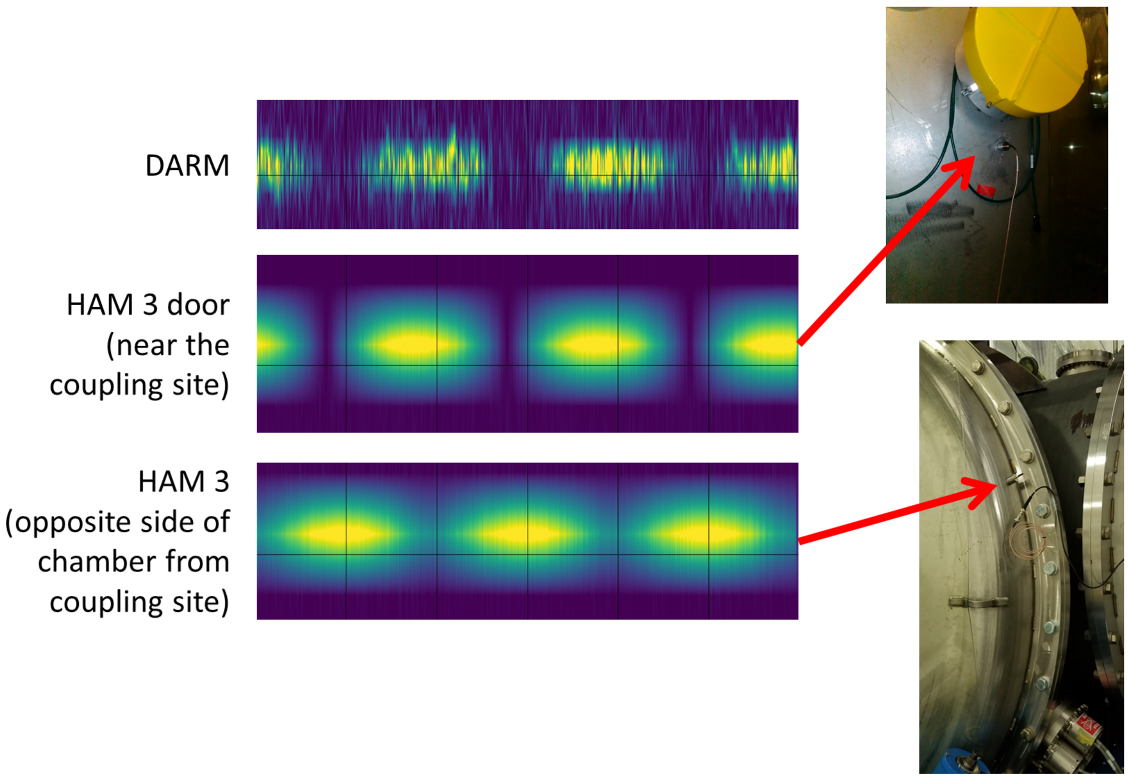

Figure 16. Beat envelopes observed in the gravitational wave channel compared to beats witnessed by accelerometers mounted to the vacuum chambers. Due to the finite travel time of the shaker vibrations in the material, there is a temporal offset of the beat envelopes strongly depending on the location of the accelerometer. The accelerometers here, despite having considerable beat offsets, were all mounted to different parts of the same vacuum chamber. The site of the coupling would be the location where the beat envelope of an accelerometer matches the envelope measured in DARM. In this case, the accelerometer in the center of the chamber door was the best match, indicating that the coupling site was very near to the illuminator viewport.

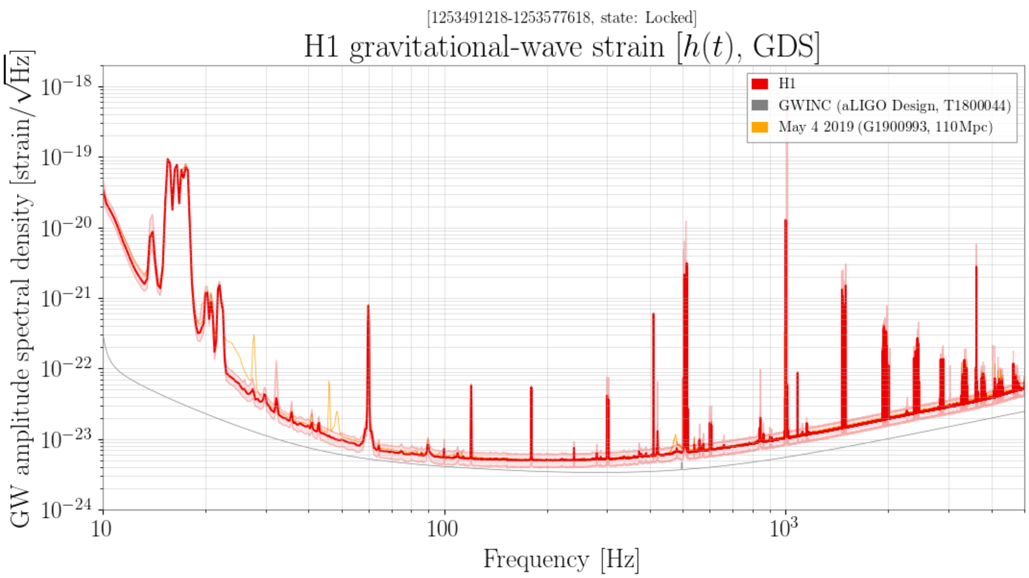

Figure 17. Daily gravitational wave amplitude spectral density from September 25, 2019 no longer showing the "bump" at 48 Hz.

CHAPTER IV

THE IMPACTS OF CORRELATED MAGNETIC FIELDS FROM LIGHTNING

4.1 Forward

On the last full day of my time at the LIGO Hanford Observatory, Robert Schofield asked me to take a look at the magnetometers at both sites. There had been a gigantic jet lightning stroke observed near Puerto Rico, and he was curious if it showed up at the sites. Lo and behold, there it was! Multiple magnetometers at both sites showed a broadband signal at nearly the exact same time. This sent me down the journey to quantify this effect on the detectors as a source of coherent noise. While I initially began the project only considering gigantic jets specifically, since they are not well documented, this was expanded into considering the effects of any lightning stroke. This section contains material previously published in Janssens et al. (2023).

4.2 Introduction

One of the worst forms an unwanted signal can take in a gravitational wave detector is one that is coherent or correlated between multiple distant detectors. Some of the earliest known potential sources for this kind of signal are the Schumann resonances, a set of electromagnetic resonances in the Earth-ionosphere waveguide (Himemoto & Taruya, 2019). As these are generally persistent signals, they are of most concern to searches for a stochastic gravitational wave background (Christensen, 2018; Coughlin et al., 2016, 2018; Himemoto & Taruya, 2017, 2019; Thrane, Christensen, & Schofield, 2013; Thrane, Christensen, Schofield, & Effler, 2014). These signals occur in the 6-25 Hz band and have been measured as coherent across Earth-scale distances. The impacts of these on GW detectors have been studied before (Kowalska-Leszczynska et al., 2017).

The primary mechanism for these signals to contaminate GW detectors is via either direct magnetic coupling to permanent magnets in actuation systems or by coupling to electronics and cabling (Nguyen et al., 2021; Thrane et al., 2013, 2014). In order to measure the effects of magnetic fields on the detectors, advanced LIGO installed low-noise LEMI-120 magnetometers at the LIGO Hanford and LIGO Livingston observatories (Aasi et al., 2015). These had primarily been used to monitor the Schumann resonances (Coughlin et al., 2018). Here, we study the effects of 1–1000 Hz magnetic field fluctuations for the LIGO detectors, specifically focusing on the effects of magnetic fields from individual lightning strokes [1]

In Section 4.3, we investigate the correlations and properties of individual lightning strokes. In Section 4.4, we quantify the effect of individual lightning strokes on searches for burst GWs, both current and future. Finally, in Section 4.6, we discuss the mechanism through which these magnetic fields may contaminate GW detectors.

4.3 Magnetic coherence between LIGO sites produced by the superposition of individual lightning strokes

4.3.1 Establishing LIGO detections of individual lightning strokes. Electromagnetic waves created by individual lightning strokes have signatures in both the 3Hz-3kHz Extremely Low Frequency (ELF) band and the 10-20kHz Very Low Frequency (VLF) band (Simões, Pfaff, Berthelier, & Klenzing, 2012). Traditionally, the VLF band is used by lightning detection networks to track individual lightning signals, but the ELF band has also been shown to be usable for

[1] The term "strike" is colloquially used for lightning. However, in the technical literature, "stroke" describes both cloud-to-cloud and cloud-to-ground lightning. "Strike" only refers to cloud-to-ground. Later in this paper we will use the Vaisala GLD360 database (Said, Cohen, & Inan, 2013) which detects "strokes" in general, so we use this term to refer to all detected lightning events here (Holle, 2020).

this purpose (Simões et al., 2012) and has some unique propagation characteristics (Gołkowski et al., 2018). The ability of the ELF band to travel long distances implies that these signals could be picked up by sensitive magnetometers at GW detectors, even if the lightning occurs several hundreds to thousands of kilometers away. This naturally raises the question whether the global lightning background could impact GW detectors.

In the remainder of this section, we will focus on coherence between LHO and LLO. Here, coherence takes the standard form in equation 4.1 where CSD_{IJ} is the cross-spectral density between data I an J and PSD_I is the one-sided power spectral density of data I.

$$coh_{IJ}(f) = \frac{|CSD_{IJ}(f)|^2}{PSD_I(f)PSD_J(f)} \tag{4.1}$$

We establish these correlated short-duration signals by identifying magnetic signals at individual magnetometers at each LIGO site. We then reduce these to magnetic signals coincident between sites to build a set of LIGO-measured magnetic signals. We then compare these to the GLD360 lightning dataset from Vaisala (Said et al., 2013) as a confirmed reference. GLD360 data for the week of September 23, 2019 was provided for this section.

To identify lightning signals coincident between sites, we use the Omicron transient detection tool (Robinet et al., 2020) to select periods of excess noise in the LEMI-120 magnetometers located at LHO and LLO during the week of September 23, 2019. The LEMI-120 magnetometers are low-noise, sensitive up to around 400 Hz, and sampled at a rate of 4096 Hz. Each site has two of these magnetometers, one aligned with each orthogonal arm of the interferometer, and the Omicron tool was run on each magnetometer independently. The Omicron tool looks for excess energy (deviation from the average background) via sine-Gaussian fits. This gives a time-frequency grid of energy for the data. SNR values are computed for each pixel of the grid, and those exceeding a minimum threshold are recorded. Individual pixels adjacent in time are clustered as combined events. Omicron returns the start and end time of each of these events (referred to as triggers) with the minimum and maximum frequency of the pixel cluster. It also returns the time and frequency of the maximum energy pixel of the trigger which are recorded as "peak times" and "peak frequencies" (Robinet et al., 2020).

A comprehensive list of coincident LEMI signals was collected by selecting Omicron triggers meeting time coincidence criteria. For triggers in different magnetometers at the same site, we want trigger times to be effectively identical. For triggers at different sites, we want triggers to be separated by no more than the travel time for a wave propagating at 75% of the speed of light along the surface of the Earth. This accounts for the frequency-dependence of the signal propagation that decreases to as low as $0.75c$ at $\sim 10\,\mathrm{Hz}$ (Kemp, 1971). To account for uncertainties in Omicron time clustering, these thresholds are loosened to 5 ms (20 LEMI samples) between magnetometers at the same site and twice the light travel time for magnetometers at different sites. This large uncertainty on the timing of the lightning is caused by the fact that Omicron combines both time and frequency information. Whereas the frequency information can give more insight on the spectral behaviour of the event it comes at a cost with respect to the time resolution. Because each site has two orthogonal magnetometers, we selected triggers that were detected in at least three of the four total magnetometers subject to the aforementioned time delays. The peak time at each site was recorded for each coincident trigger to preserve the relative time delay between sites. This set of triggers, those coincident between LHO and LLO magnetometers, we refer to as "HL coincident triggers."

We match the HL coincident triggers to the Vaisala GLD360 lightning detection database (Said et al., 2013). This dataset is collected by a broad network of GPS-synchronized sensors which use matched waveforms to estimate the location of a lightning stroke as well as the peak current. The current is estimated with a resolution of $\mathcal{O}$(kA), with polarity determined by the direction of the electric field – a negative current is assigned for an electric field pointing toward the Earth (Said et al., 2013). The GLD360 network claims an 80% detection efficiency in identifying cloud-to-ground strokes in the Northern Hemisphere and between 10% and 80% detection efficiency in the Southern Hemisphere (Demetriades, Murphy, & Cramer, 2010; Naccarato et al., 2010). Worldwide lightning strokes with 10 km spatial and $1\,\mu s$ temporal resolution were provided for the week of September 23, 2019 to match the HL coincident triggers. The required signal travel time for each GLD360 lightning stroke to each detector is computed assuming the minimum frequency-dependent travel speed of $0.75c$ (Kemp, 1971). This is used as an upper limit for the time difference between signals at each site and the detected lightning. A lower limit is set similarly assuming a signal travel speed of c.

Directly trying to identify coincidences between the GLD360 lightnings and HL coincident triggers on an event-by-event basis leads to a tremendous amount of false coincidences. This is caused by the large amount of GLD360 lightnings as well as HL coincident triggers, in combination with the large time window for identification due to LEMI sampling (4096 Hz) and Omicron time clustering.

To decrease the number of false positives, lightning strokes are broken up into 24 hour segments and clustered by location via K-means clustering (Hartigan, 1975). A cluster can roughly be compared to all the lightnings in a thunderstorm. For each cluster of lightnings, an event-by-event comparison is made between the HL coincident triggers and GLD360 strokes. In this comparison a time slide up to $\pm$ 2 s is applied to the GLD360 strokes and the number of coincidences between the GLD360 strokes and the HL coincident lightnings is counted as a function of the time slide duration. In case of a physical coincidence one would expect to observe a large number of coincidences when the time offset is zero and a lower number of coincidences for a non-zero time offset. In the case of purely chance coincidences, no larger amount of coincidences is expected for a zero time offset. By selecting regional lightning clusters where the zero time-offset peak is more than two times the number of background coincidences, we reject coincidences which are likely to be spurious. Afterwards, the individual coincident lightnings for accepted clusters are selected and these LHO-LLO-Vaisala coincidences, will be referred to as "lightning-coincident triggers."

From the two-site coincidence check, we find 314928 total HL coincident triggers. When compared to the 45007030 total GLD360 lightning strokes, we find 268971 total lightning-coincident triggers. We estimate a false-coincident rate of approximately 1 in 1200. This value is estimated from the average rate of background coincidences over the week, measured from the time slides, multiplied by coincidence time window.

In some clusters the background coincidences are about $0.5\% - 1\%$ of the number of lightnings in that given cluster. With the total number of lightnings this would lead to a number of coincidences which is of the same order of magnitude as the amount of HL coincident triggers. This highlights the need of the clustering

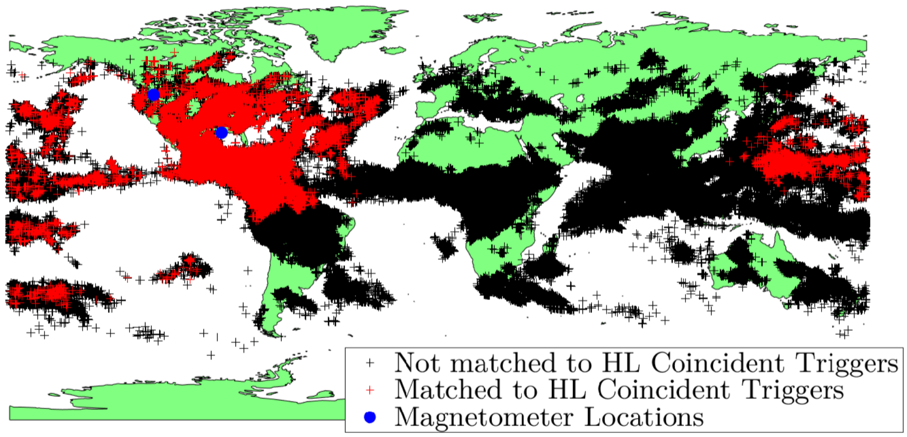

Figure 18. Map of all GLD360 lightning strokes during the week of Sept 23, 2019. Red (black) marks are events that did (not) align with HL coincident triggers. The presence of coincident events highlights North America as the primary sensitivity region.

and time-sliding analysis as a method to reject false coincidences when comparing the GLD360 strokes and the HL coincident triggers.

As seen in Fig. 18, the coincident lightning strokes were primarily confined to the Americas and Pacific. Over 97% of these were in North and Central America, suggesting that this is the approximate sensitive region for individual lightning signals observed at the LHO and LLO sites.

The distribution of global lightning strokes is generally balanced between positive and negative currents; however, the strokes that match the HL coincident triggers tend heavily toward negative currents (see Fig. 19). Negative currents in the GLD360 are assigned to electric fields pointing toward the Earth (Said et al., 2013). Strokes matched to HL coincident triggers have a noticeable dip near zero likely due to lower current strokes generating weaker magnetic fields and not being witnessed by magnetometers at both sites. The magnetic field fluctuations from lightning have durations below 10 ms and amplitudes of a few nT. Fig. 20 shows an example of a signal measured at both LHO and LLO believed to originate from

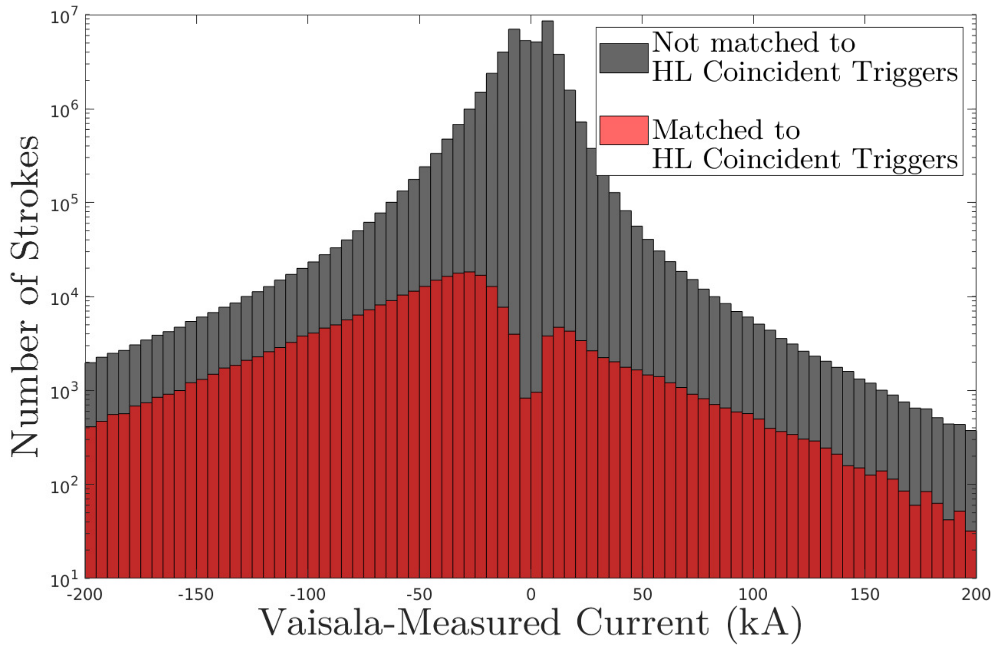

Figure 19. Distribution of global lightning stroke currents reported in GLD360. Grey distribution shows the current distribution of all lightning strokes in GLD360 not matched to an HL coincident trigger (corresponding to black locations on Fig 18). Red distribution shows the current distribution of lightning strokes that were coincident with HL coincident triggers (corresponding to red locations on Fig 18). The dip at 0 in the matched strokes is likely due to lower current strokes not generating strong enough fields to be witnessed by magnetometers at both LIGO sites.

the Caribbean Sea. Spectra of the LHO magnetometers are shown in Fig.21, where excess amplitude can be seen in the range $1 - -1000\,\text{Hz}$.

Lightning-coincident triggers are highly diurnal[2] in occurrence, as shown in Fig. 22. The shaded region marks local night in the central United States. The hourly lightning-coincident trigger rate exceeds 2000 coincidences per hour at times. This diurnal rate is most likely a mixture of the local lightning rate (since most strokes are localized spatially and occur during local night) and a diurnal

[2]Throughout this paper we will use the term diurnal to refer to the daily variations in lightning strikes as is done in literature (Blakeslee, Mach, Bateman, & Bailey, 2014).

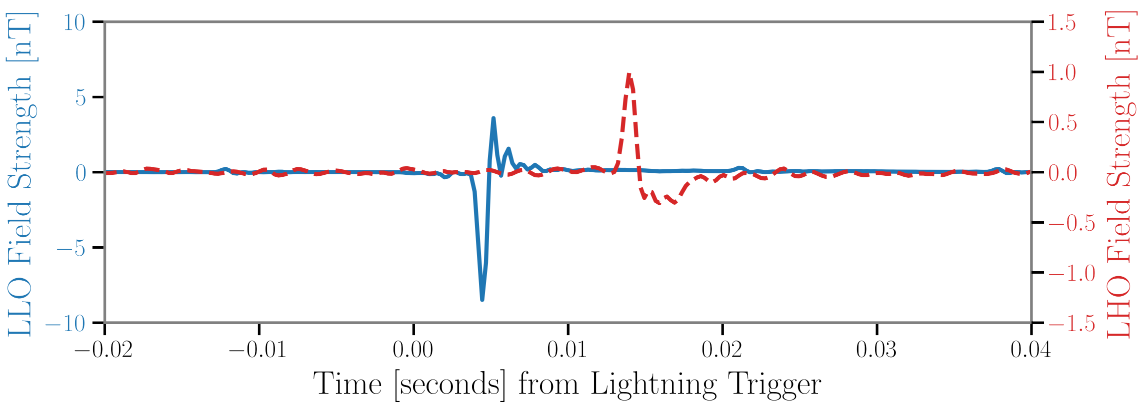

Figure 20. Timeseries of a lightning stroke witnessed by magnetometers oriented along the X-arms of each LIGO site. The blue solid line is LLO, and red dashed line is LHO. This is a lightning-coincident trigger linked to a lightning stroke in the Caribbean Sea. 60 Hz mains lines were removed here.

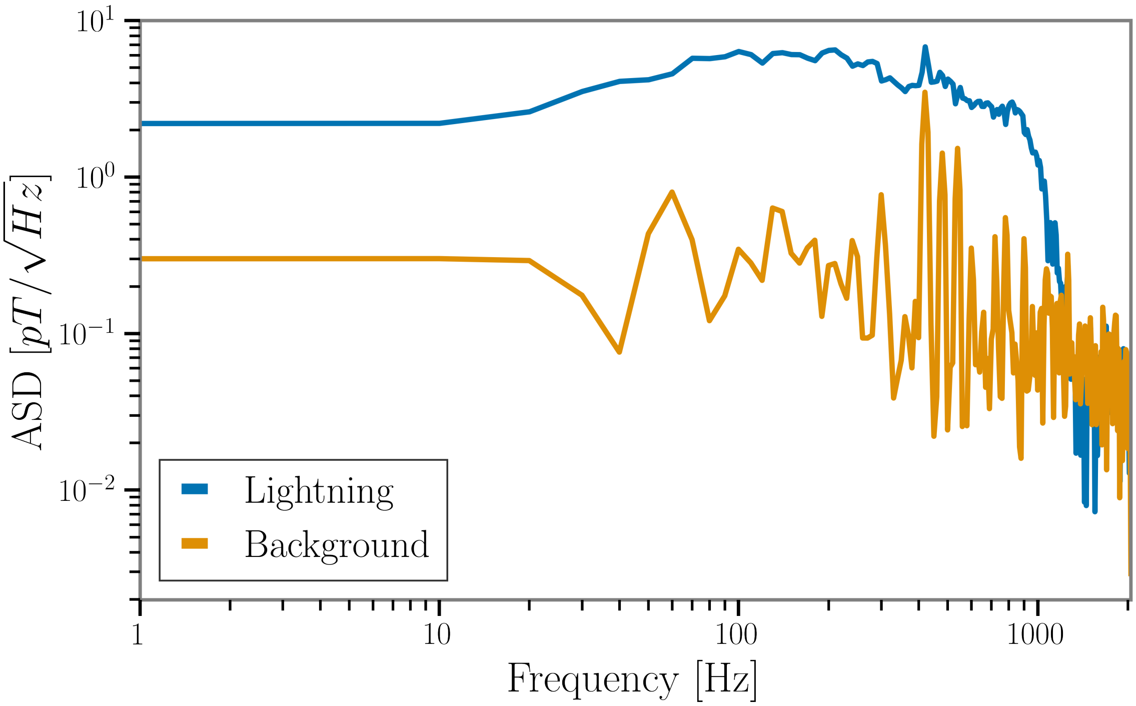

Figure 21. Amplitude spectral density from a magnetometer oriented along the LHO X-arm for the event shown in Fig. 20. Excess energy reaches from below 1 Hz to over 1 kHz. The blue curve shows 0.1s surrounding the lightning event; the orange curve shows 0.1s of background before the event. These have been corrected for the LEMI response curve, which has decreasing sensitivity at higher frequencies *LEMI Sensors: Induction coil magnetometer* (2011).

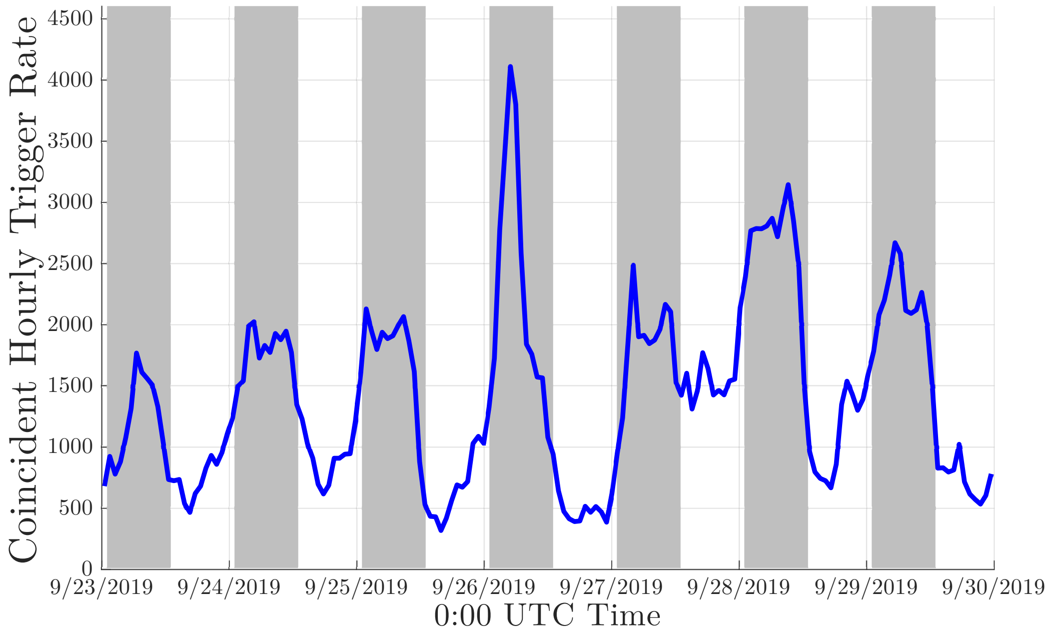

Figure 22. Hourly rate of HL magnetic triggers coincident with GLD360 lightning strokes for the week of Sept 23, 2019. Shaded regions mark approximate local night (1-13 UTC) halfway between LHO and LLO. X-axis ticks correspond to 24 hour increments at 0 UTC.

variability in the ionosphere conductivity due to solar radiation (Simões et al., 2012). This high diurnal variability in coincident signals suggests that magnetic coherence between sites may also be diurnal. Fig. 23 shows the magnetic cross spectral density (CSD) between the X-arm aligned magnetometers at the LIGO sites when broken up along the day/night cycle shown in Fig. 22. Below 200 Hz, the CSD observed during the day (red line) averages about 20% larger than at night, whereas above 200 Hz the nighttime CSD (black line) averages about 180% larger than day time.

4.3.2 Reducing inter-site magnetic coherence by excluding times with lightning strokes .

We can demonstrate the effect of lightning strokes on inter-site magnetic coherence by vetoing short time periods that

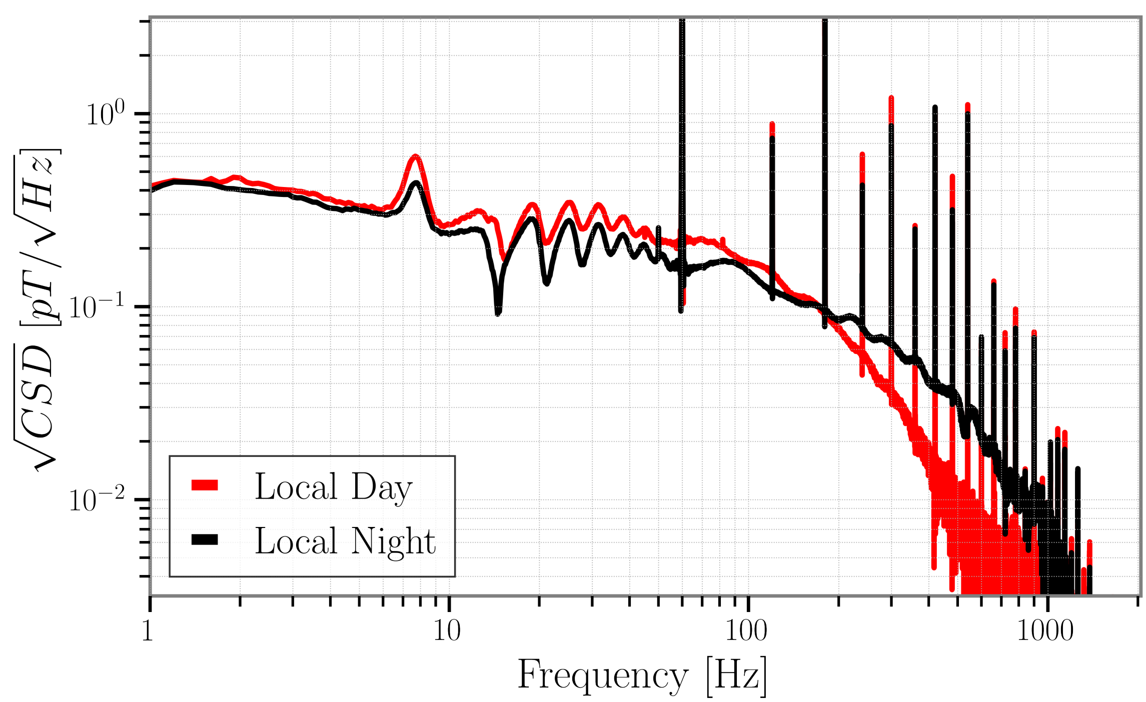

Figure 23. Magnetic CSD between the LIGO sites divided into times aligned with day and night in Fig. 22 for the entire O3 run. At frequencies above $\sim$ 200 Hz the CSD observed during local day (1-13 UTC, red) is smaller than the CSD observed during local night (14-0 UTC, black). The broad peaks below 60Hz are produced by the Schumann resonances. Peaks at multiples of 60 Hz are due to mains power lines and their harmonics.

contain individual strokes. Fig. 24 shows the coherence between LHO and LLO magnetometers over the course of the week of Sep. 23 2019 with and without vetoes of individual lightning signals. HL coincident trigger times were zeroed in the time-domain with an inverse-Tukey window in one channel (to prevent elevated low frequency coherence due to coincident vetoes) and replaced with Gaussian noise for the duration of the trigger, up to a maximum of 1 s, modulated by an equivalent Tukey window. This removes a small number of very long outliers with durations up to 1 second. However, the majority of the triggers have durations less than 0.1 s, with 90% shorter than 0.4 s. While this reduces the magnetic correlation between LHO and LLO, it did not fully account for the excess, so we also removed times directly tied to GLD360 lightning, accounting for the light travel time from the specific location of the stroke. This was done for GLD360 strokes in a 4000 km radius circle that best encompassed the sensitivity region shown in Fig. 18. We also repeated this, but with all strokes in a 10000 km radius circle, centered on the same point (far enough to reach to Europe). All GLD360-informed vetoes had durations less than 0.06s. To show that removing magnetic events is the cause of the reduced coherence, we also applied the same number of triggers randomly to the data and recalculated the coherence. The results are shown in the bottom plot of Fig. 24, and we see little to no reduction in the coherence.

The top plot in Fig. 24 shows the reduction in coherence as a function of the lightning vetoes used. HL coincident triggers accounted for 0.7% of the globally detected lightning during this time, and represent removing about 7.5% of the observation time. GLD360 strokes in the 4000 km radius circle accounted for 21.8% of globally detected lightning, and the vetoes removed 37.4% of the observation time. The GLD360 strokes in the 10000 km radius circle accounted for 44.9% of

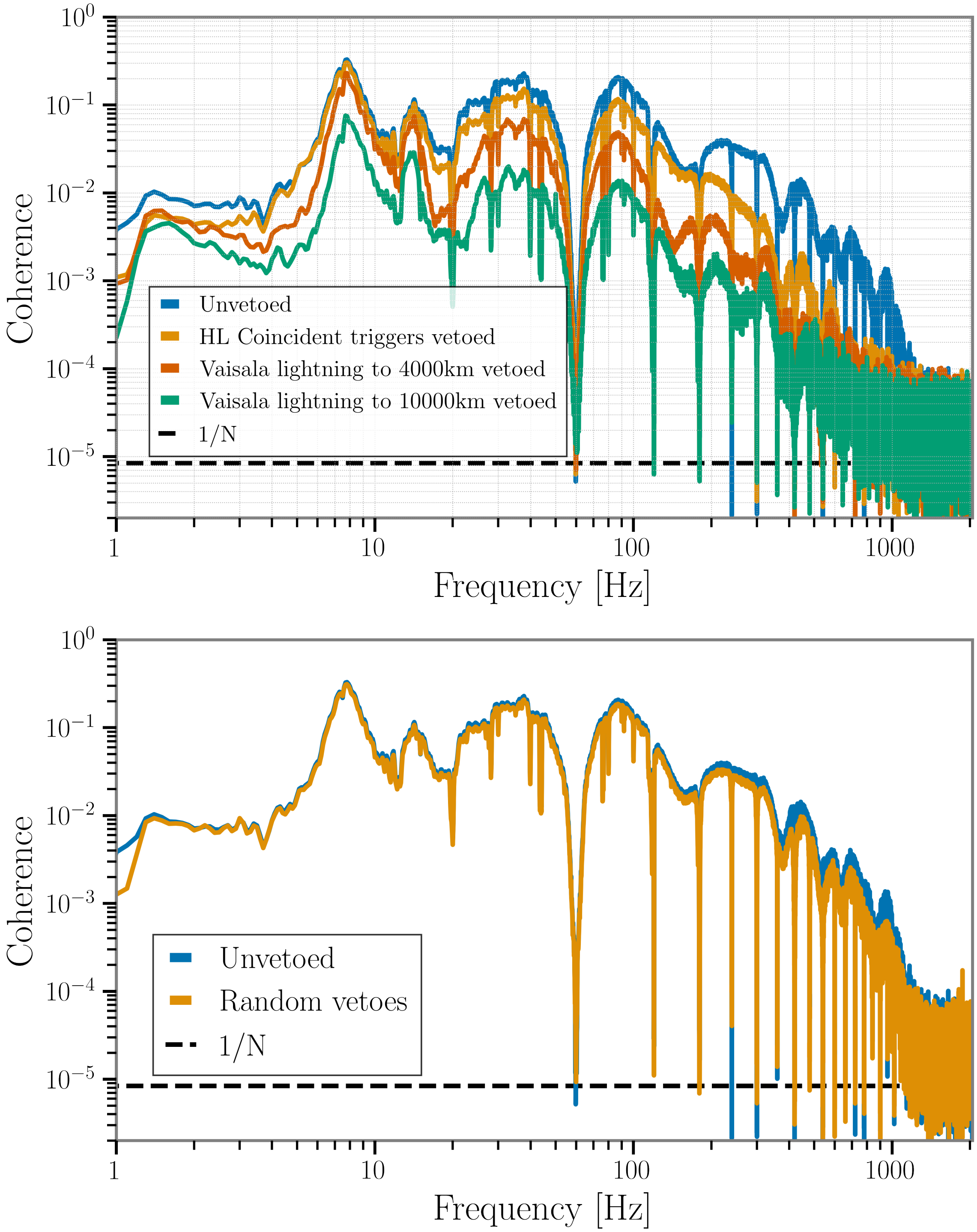

Figure 24. Top: Coherence (LHO and LLO magnetometers) spectra for the week of Sept 23, 2019 with varying amounts of lightning events vetoed. In the absence of correlated noise, one expects this to be consistent with Gaussian noise given by the number of averages (N) used to make the coherence spectrum, indicated by the black dashed line. Bottom: Randomly applying the same number of trigger vetoes to the data has minimal impact on the coherence spectra suggesting that lightning is the direct source of high frequency coherence. We note that near 1 Hz the coherence of the data with randomly shifted vetoes is lower. The origin of this is unknown.

global lightning, and the vetoes removed 70.9% of the observation time. Massively increasing the amount of lightning vetoed does reduce the coherence by over an order of magnitude but also removes the majority of the observation time, which is unfeasible in practical application. Whereas going from using HL coincident triggers to using GLD360 detections has a significant impact up to around 300 Hz – nearly double the reduction in some frequency ranges – it has negligible impact on reducing the coherence above a few hundred Hz and requires removing over 9 times as much observation time.

4.4 Impact on transient GW searches

We can estimate the effect of the individual lightning strokes on the GW strain using outside-to-inside magnetic coupling functions and inside-to-GW channel coupling functions for internal magnetometers. We present the budget for LLO in Fig. 25. We chose LLO to examine here due to greater nearby lightning activity relative to LHO as well as stronger observed magnetic coupling. This combination allows us to examine the worst case scenario for coupled lightning events.

To date, LIGO has not observed excess noise in GW strain due to individual lightning events (Davis et al., 2021; Schofield, 2016), whereas Virgo has (Acernese et al., 2022). Note that vibrational effects from thunder have been observed both at LIGO as well as Virgo (Acernese et al., 2022; Davis et al., 2021). With the increasing sensitivity of the current and future GW detectors, it is important to understand if additional mitigation efforts will be required.

We use the scalar value of the outside-to-inside magnetic coupling function measured from the ratio of the amplitudes of individual lightning events as described in Appendix 4.6. The inside-to-GW channel magnetic coupling functions include both directly measured values as well as upper limits. Measured values are log-normal with a factor of 2 uncertainty, and upper limits are treated as uniform uncertainties from 0 to the upper limit value in each frequency bin (Nguyen et al., 2021).

Fig. 25 includes theoretical noise curves for current and future detectors (Barsotti, Fritschel, Evans, & Gras, 2018a, 2018b; Hild et al., 2011; Srivastava et al., 2022). The predicted contribution to the GW channel spectrum of the loudest, 100th loudest, and 10000th loudest individual lightning-induced magnetic events are shown (red, dark blue, and light blue, respectively) for the week analyzed (out of the 268971 total HL coincident triggers). The width of these shaded regions represents the 68% confidence interval of the predicted contribution to the GW channel, based on the combined uncertainty in the product of the outside-to-inside and the inside-to-GW channel coupling functions. The downward triangles show the high value of the 68% confidence interval for values of the outside-to-inside coupling function with the upper limit inside-to-GW channel coupling function, which, as an upper limit, we assume has no uncertainty. All of these loudest events fall below the real O3 background but exceed the A+ design sensitivity below 20 Hz. If, in the future, lightning would couple significantly to the GW sensitive channel at one of the detectors, the event would also be measured by multiple magnetometers at each site. Such events would be identified in the standard PEM vetting system by estimating their impact on the GW sensitive channel (Nguyen et al., 2021). Once identified, It may be possible to subtract these glitches, though the coupling variability may make this subtraction difficult. However, glitch subtraction is performed for other types of glitches (Davis et al., 2022) and subtraction by

Wiener filtering has been investigated for Schumann resonances (Coughlin et al., 2016, 2018; Thrane et al., 2013, 2014).

The correlated power due to lightning could bias both unmodeled burst as well as modeled CBC searches. As an illustration, if the magnetic coupling for third generation detectors remains the same as those for the current detectors, $\mathcal{O}(10^5)$ magnetic transients per week would appear in the data. It is expected that binary neutron star mergers could be in the sensitivity band for $\mathcal{O}(10^3 s)$ in the case of third generation detectors (Hall et al., 2021; Li, Heng, Chan, Messenger, & Fan, 2022). Modeling these coherent lightnings as a Poisson process, it is nearly guaranteed that at least one lightning transient will overlap with one of these BNS signals, with over 160 overlapping lightnings expected on average for a single event. While these coherent magnetic signals may be vetted using magnetometer measurements, their presence and rate could interfere with transient GW searches and parameter estimation. This could be mitigated to some extent by reducing the magnetic couplings, since fewer magnetic transients coupling into the GW data stream will reduce the total impact on searches and analyses. However, we also recommend more detailed investigations into how to efficiently subtract these short transients from future longer events.

For third generation detectors, it may be important to consider facilities designs that could reduce the outside-to-inside coupling. Construction materials may need to be selected with this coupling in mind. For example, buildings could be constructed without using large ferromagnetic I-beams.

The lightning-induced beam tube currents discussed in Appendix 4.6 are probably particularly insidious because the beam tubes carry currents right into the heart of the detector where they generate magnetic fields in the most magnetically

sensitive regions. The lightning-induced beam tube currents might be reduced by increasing the resistance of the beam tube path through the building and reducing the resistance between the beam tube and ground, or by active cancellation.
The coupling of lightning-induced beam tube currents might also be reduced by distancing the primary coupling sites, like the magnets in magnetic actuators and the cable trays that carry signal cables, from the beam tubes. Other structures may also carry induced currents, and ferromagnetic structures such as I-beams may even locally amplify the correlated magnetic fields.

Furthermore, one can try to reduce the amount of magnets and ferromagnetic components attached to the test masses, as well as moving them higher up in the seismic suspensions stages. Finally, additional shielding can be considered as a complementary method to reduce the magnetic coupling (Cirone et al., 2019).

4.5 Conclusion

In this work, we have demonstrated the effects of transient magnetic fields from lightning on Earth-scale measurements of correlated magnetic transients and magnetic coherence. We have shown that magnetometers located at the LIGO Hanford and LIGO Livingston GW detectors likely measured these effects.

We quantified the effect of these fields on GW searches by using measured magnetic coupling functions and large-scale magnetic field fluctuations. While LIGO's third observing run was free of magnetic contamination, future more sensitive runs could be affected by this correlated noise source. Future detectors suh as Cosmic Explorer and the Einstein Telescope are especially at risk if the magnetic coupling mechanism is similar to that of current detectors.

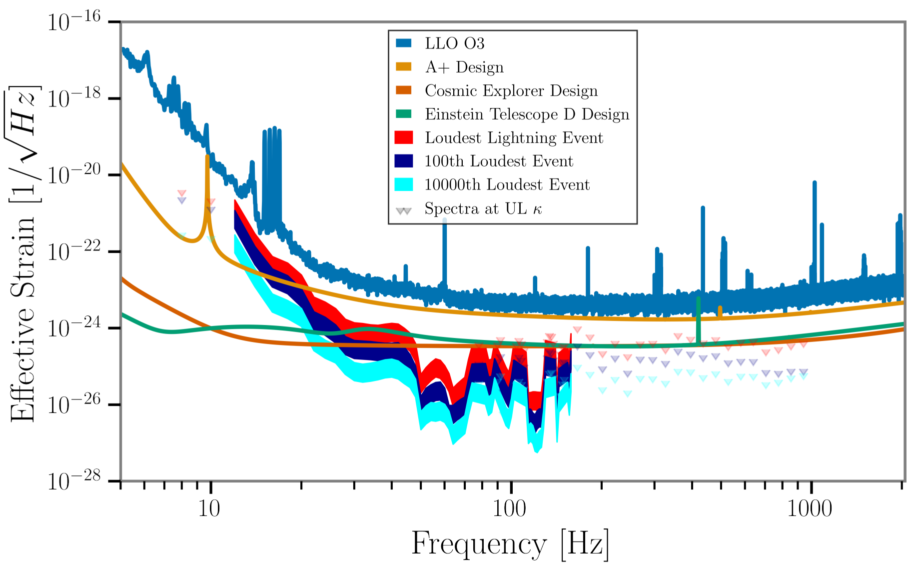

Figure 25. Estimates of the strain noise produced by individual lightning strokes for LIGO and, assuming the same magnetic coupling, for future detectors. The wide bands were made by projecting LEMI magnetic field spectra from the 1st, 100th, and 10000th highest amplitude lightning strokes detected by Omicron projected into the main GW strain channel through the outside-to-inside and inside-to-GW channel magnetic coupling functions as measured at LLO. Spectra represent 0.5s around lightning event. Shaded regions represent the 68% confidence interval for the spectra at frequencies where the inside-to-GW channel coupling functions are fully measured. Downward triangles represent the spectra at frequencies where only an upper limit for the inside-to-GW channel coupling is known. Upper limits are the maximum potential value of the inside-to-GW channel coupling when an injection does not generate a response in the GW strain readout. These estimates are shown against O3 background (blue line), the A+ design sensitivity (light orange line), and sensitivity estimates of Cosmic Explorer (dark orange line) and the Einstein Telescope (green line). The coupling at these planned facilities could potentially be reduced from the levels measured at LLO by further separating magnetic coupling sites, like cables and actuation magnets, from lightning-induced currents on the beam tubes.

Additional research is still needed to decrease the magnetic coupling, both the outside-to-inside and inside-to-GW mechanisms. The magnetic coupling could be reduced by shielding of the test masses (Cirone et al., 2019) and further optimization of eddy current shielding from building cladding. The reduction of lightning induced beam tube currents, as discussed in Sec. 4.4 and Appendix 4.6 should also be further investigated. Finally, for third generation detectors the placement of magnets and ferromagnetic components in the suspension design should be carefully considered.

In the event that complete mitigation of coupling cannot be achieved, further research will be needed on methods for how to eliminate contamination from data analysis. Data subtraction has been proposed as a solution, but the variation and uncertainty in the coupling functions make this quite difficult. For stochastic analyses, the intrinsic diurnal and seasonal vaiariation in the magnetic coherence could be used to distinguish between real astrophysical sources and these environmental effects.

4.6 Appendix: The outside-to-inside magnetic coupling function

Presently, we produce estimates of the inside-to-GW channel coupling of magnetic fields around the detector to the main GW strain readout by generating large fields (much larger than the magnetic fields generated by lightning) inside the buildings that house the sensitive regions of the detector, and then comparing the amplitude of the resulting signals from the GW strain readout and from the magnetometers in the buildings. In order to estimate the signal in the GW strain readout using the outdoor LEMI magnetometers, which are away from the noisy buildings and sensitive to the small inter-site correlated fields, we need to be able to estimate the amplitude of the fields inside, around the detector, from the fields measured by the outside LEMI magnetometer.

Previous estimates of this outside-to-inside magnetic field coupling were based on a comparison of outside and inside magnetometers for magnetic injections made using a generating coil that was set up at multiple locations outside of the vertex building (R. Abbott et al., 2021f). However, these coil-generated fields differ from the fields from distant lightning in time-scale and field uniformity. Lightning detection networks make it possible to identify lightning - generated magnetic field transients and thus to measure the outside-to-inside coupling specifically for magnetic fields from lightning.

To estimate this outside-to-inside coupling, individual lightning strokes were selected from the GLD360[3] at ranges exceeding 200km from LLO. The distance requirement serves to reduce any vertically-oriented field since the outdoor magnetometers are designed to detect Schumann resonance fields and have no vertical axis. We chose to calculate this for LLO due to the greater abundance of nearby lightning events. The events with the largest estimated ratio of current to distance were picked to ensure the signal was clearly witnessed by both outside and inside magnetometers. Signals were selected with an SNR exceeding 10 as measured outside and greater than 6 inside. Notch filters were used to remove all harmonics of the 60Hz mains line. All axes were added in quadrature (including the vertical components for interior magnetometers), and the result was high-passed to remove any DC offset from the quadrature sum.

[3]For this measurement additional GLD360 data was provided by Vaisala for the week of July 8 to 14, 2019 as well as December 29, 2021 to January 3, 2022, January 25 to 27, 2022, and February 3 to 5, 2022.

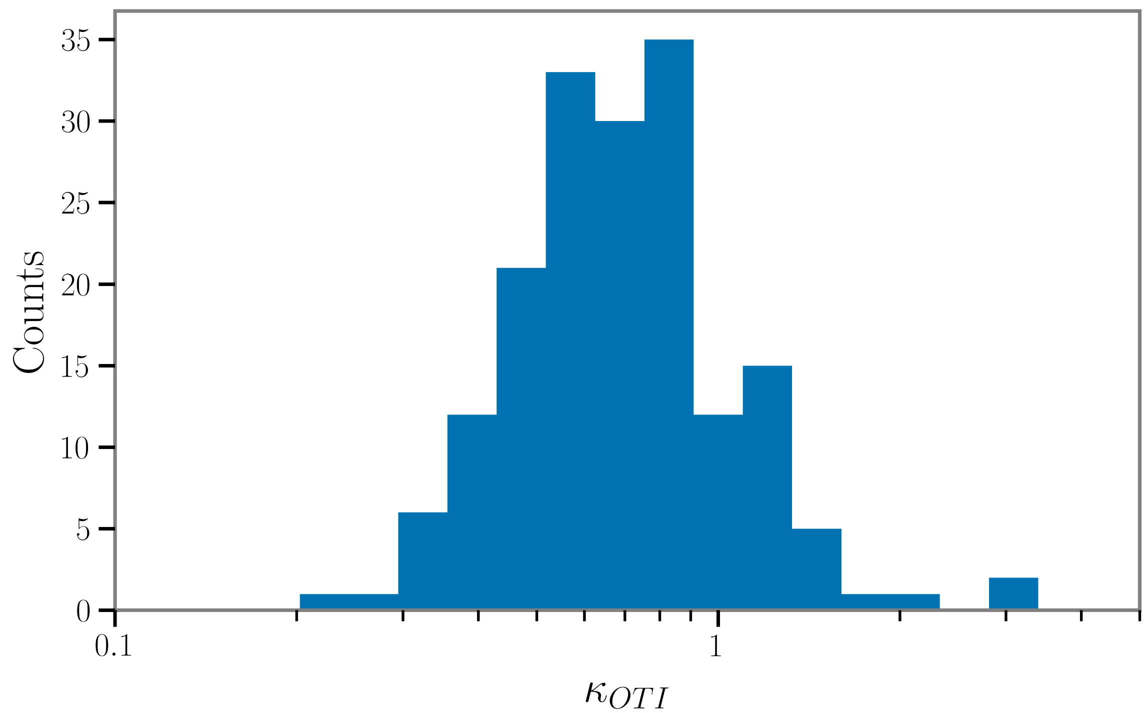

Figure 26. Histogram of outside-to-inside coupling function values estimated from individual lightning strokes.

Time series of an example lightning event are shown in the two top panels of Fig. 27. The ratio of the peak amplitudes of these processed time series was used to estimate a scalar value for the outside-to-inside coupling function. Using multiple lightning events results in a log-normal distribution of coupling values with mean value $0.7^{+0.4}_{-0.3}$ nT/nT (Figure 26). The power-law estimate from static coil injections discussed earlier agrees strongly with this estimate, falling within the uncertainty limits for our frequency range.

Some interior magnetometers witnessed significant vertically-oriented magnetic fields for some lightning signals, primarily at LLO. Significant vertical fields are not expected for distant lightning (Silber, Price, Galanti, & Shuval, 2015) and are not monitored by the external magnetometers. Horizontal fields may produce vertical fields through induced currents or field distortions associated with ferromagnetic structures. The vertical fields that were observed in the building were roughly consistent with a simple model in which the distant lightning would induce currents in a loop consisting of the beam tube, the beam tube grounding, and the earth beneath the beam tube. This induced current would generate fields around the beam tube inside of the buildings. The existence of beam tube current transients coincident with distant lightning was confirmed using current probes clamped on beam tube grounding cables. GLD360 lightning events from distances greater than 200 km from the site were selected and the magnetic fields measured on site for these events were identified in our magnetometers in coincidence with currents measured on the beam tube. Fig. 27 shows one such signal witnessed by both exterior and interior magnetometers and the beam tube grounding current monitor.

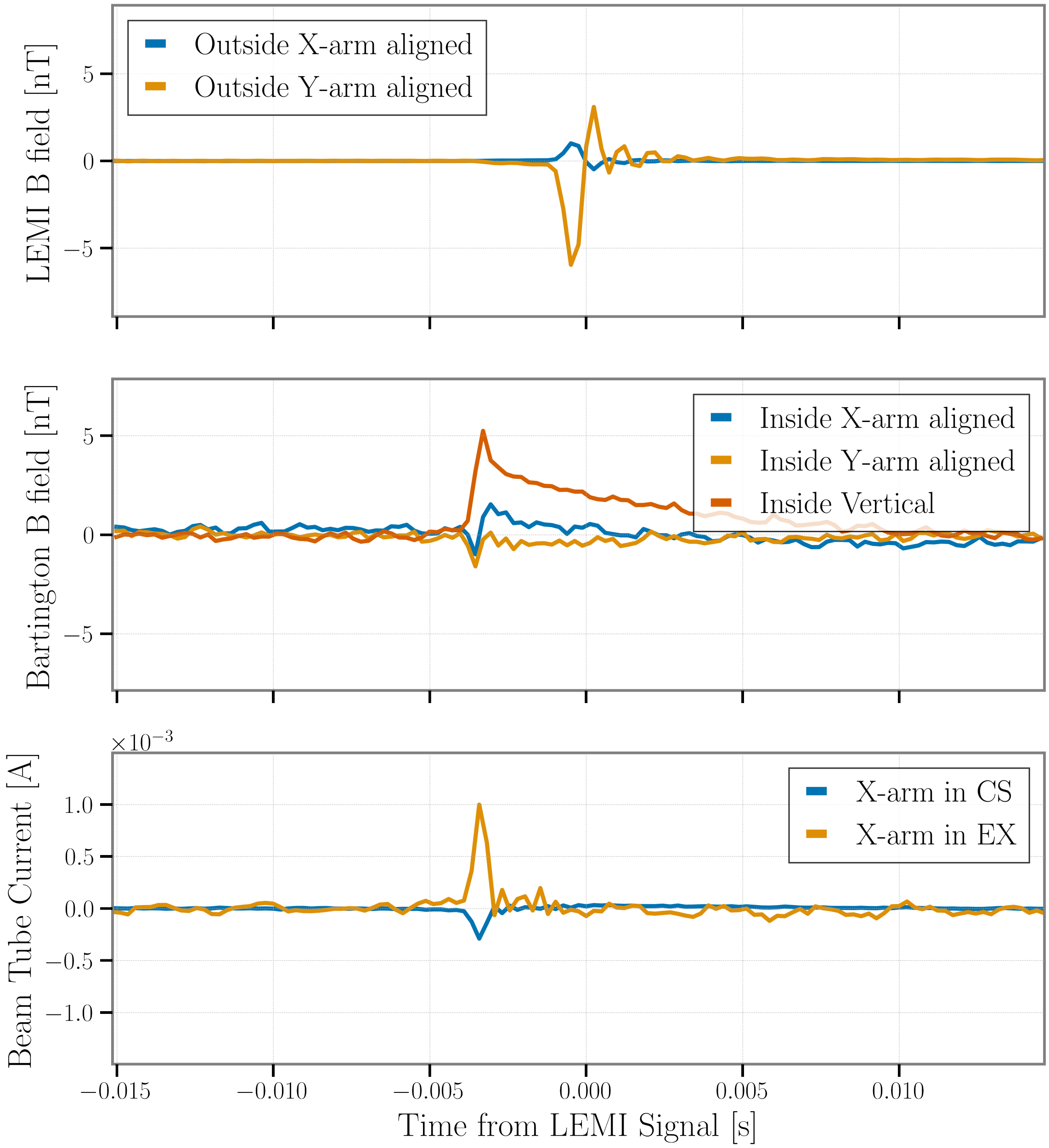

Figure 27. Top: Filtered magnetometer measurement of magnetic field believed to be from a lightning stroke as measured by outdoor magnetometers at LLO. Center: The same lightning-generated field as measured by an interior magnetometer, showing a strong vertical component. Bottom: Measurements from current probes clamped to beam tube grounding cables at various locations on the X-arm (CS: corner station, EX: X end station). At the location of the magnetometer, the field from a current on the beam tube would mainly be vertical. The observed delay in the LEMI magnetometer is believed to be an instrumental effect due to an additional fiber-optic transmission step in recording the data.

CHAPTER V

PARAMETER ESTIMATION OF GRAVITATIONAL WAVES FROM NEUTRON STAR F-MODE OSCILLATIONS

5.1 Forward

During my time investigating the impacts of lightning on the detectors, I began to get involved in searches for gravitational wave bursts associated with magnetar flares (specifically, I was an analyst for R. Abbott et al. (2024c)). I found the models the team considered to be fascinating, but I was disappointed by the rather underwhelming results that would be reported. Since no signals were detected, the results were simply the integrated strain of test waveforms that the searches were able to recover when injected into the data. These strain values had little physical meaning, and I questioned how the search might be able to say something more interesting, ideally regarding direct parameters of the magnetars in question. I was also disappointed when I realized that there did not seem to be a real plan for what to do *if* a signal was ever detected. I decided to attempt to answer these questions myself with this project. This section contains material previously published in Ball, Frey, and Merfeld (2024).

5.2 Abstract

Magnetar vibrational modes are theorized to be associated with energetic X-ray flares. Regular searches for gravitational waves from these modes have been performed by Advanced LIGO and Advanced Virgo, with no detections so far. Presently, search results are given in upper limits on the root sum square of the integrated gravitational-wave strain. However, the increased sensitivity of current detectors and the promise of future detectors invite the consideration of more astrophysically motivated methods. We present a framework for augmenting

gravitational wave searches to measure or place direct limits on magnetar astrophysical properties in various search scenarios using a set of phenomenological and analytic models.

5.3 Introduction

Magnetars are a subclass of neutron stars observed to possess magnetic fields with strengths of 10^{14} G to 10^{15} G (Duncan & Thompson, 1992) and may be responsible for the highly energetic emission of X-rays and soft γ-ray flares. Presently, there are 30 known galactic magnetars[1] found via these (and other) types of emission (Olausen & Kaspi, 2014). These flares are short duration and believed to be due to interactions between the powerful magnetic field and the exotic matter of the star (Thompson & Duncan, 1996). Flaring behavior typically falls into two primary categories: flares with equivalent isotropic energies of 10^{36} to 10^{43} ergs (see Kaspi and Beloborodov (2017) and references therein for a review) and the far rarer giant flares with isotropic energies of 10^{44} - 10^{46} ergs (Hurley et al., 2005, 1999; Mazets, Golentskii, et al., 1979). Figure 6 shows the light curve measured by Swift BAT for the 2004 giant flare of SGR 1806-20 (Palmer et al., 2005).

The detailed internal structure of neutron stars, and magnetars in particular, remains uncertain. Gravitational wave (GW) observations of merging extragalactic binary neutron star systems have already contributed to constraints on the neutron star equation of state (B. P. Abbott et al., 2017b, 2018). GWs emitted from isolated galactic neutron stars would provide a promising new method to explore neutron star astrophysics. The LIGO-Virgo-KAGRA network of GW detectors has carried out a series of searches for GWs associated with magnetar X-ray flares (Abadie et al., 2011a; B. Abbott et al., 2007; B. P. Abbott et al.,

[1] http://www.physics.mcgill.ca/~pulsar/magnetar/main.html

2019; R. Abbott et al., 2024b; Macquet, Bizouard, Burns, et al., 2021). While no direct detections have resulted and only limits on the integrated root sum squared GW strain at 50% and 90% detection efficiencies have been placed, the increasing sensitivity of the detectors begs the question whether such observations are likely in the near future, or with proposed next-generation detectors such as Cosmic Explorer (CE), Einstein Telescope (ET), or the Neutron Star Extreme Matter Observatory (NEMO) (Ackley et al., 2020; Hild et al., 2011; Srivastava et al., 2022).

Unlike binary neutron star mergers, the mechanism(s) for transient GW emission from isolated neutron stars is uncertain. Given the uncertainties, the GW searches to date have made few assumptions regarding specific waveform models. However, Giant flares present a uniquely promising scenario of observing GW emission in the form of f-modes with the extreme energy release from magnetars observed as giant X-ray flares.

Giant flares in particular are thought to be due to two connected mechanisms: powerful magneto-hydrodynamic deformations within the interior of star triggered by the cracking of the thin crust of the star, and a reconfiguration of the exterior magnetosphere (Levin & Van Hoven, 2011). Magneto-hydrodynamic deformation models predict that a neutron star has fundamental equilibrium states and can suddenly experience a reconfiguration of the internal structure when changing to a different state. This reconfiguration can potentially release an enormous amount of energy emitted through flares and gravitational waves created by the deformation (Corsi & Owen, 2011; Ioka, 2001). Such deformation can be triggered by a large-scale cracking of the crust (de Freitas Pacheco, 1998; Thompson & Duncan, 1995), which also serves to provide a channel for the magneto-hydrodynamic wave to propagate from inside the star to the exterior magnetosphere (Gill & Heyl, 2010; Levin & Van Hoven, 2011; Lyutikov, 2006).

The vibrational modes excited within the neutron star are believed to be predominately fluid pressure modes. The fundamental mode (f-mode) is the lowest order ($l = m = 2$) quadrupole pressure mode, potentially being the strongest contribution to the generation of gravitational waves (McDermott et al., 1988), expected to be nearly monochromatic in the approximate range of 1 to 3 kHz (de Freitas Pacheco, 1998; Lindblom & Detweiler, 1983). These excitations are expected to be short-lived since pressure oscillations within the star are expected to couple with the core and primarily decay through GW emission, causing the oscillations to potentially last for between a fraction of a second and a few seconds (Levin, 2006).

Theoretical calculations have estimated the total energy released during a giant flare and predict that the GW energy could be high enough to be detectable by near-future detectors by assuming that all available flare energy is released in the GW channel (Corsi & Owen, 2011). Other, less optimistic calculations give GW energies far below what is detectable for sources at around 1 kpc with even proposed future GW detectors (Ciolfi & Rezzolla, 2012; Levin & Van Hoven, 2011; Zink, Lasky, & Kokkotas, 2012).

In previous analyses (B. P. Abbott et al., 2019; R. Abbott et al., 2024b), short-duration, targeted searches use the coherent analysis algorithm X-Pipeline (Sutton et al., 2010; Wąs, Sutton, Jones, & Leonor, 2012). Other analyses have considered longer duration signals using PySTAMPAS (Macquet, Bizouard, Burns, et al., 2021) (see, for instance Macquet, Bizouard, Christensen, and Coughlin (2021)) or all-sky, untargeted searches for f-modes associated with pulsar glitches using Coherent WaveBurst (Drago et al., 2021; Lopez et al., 2022). Here, we focus on X-Pipeline for consistency with previous targeted, short-duration searches. X-Pipeline is a targeted, minimally-modeled, coherent search algorithm. Data from multiple detectors are transformed into time-frequency coherence maps, and the most energetic clusters of pixels which still meet pipeline coherence thresholds after data quality vetoes are recorded. For a nearly monochromatic signal, one might expect a detection to appear as a line of constant-frequency pixels centered on the central frequency of the signal with a narrow bandwidth of only a few Hz. Given the astrophysical uncertainties associated with magnetars and their potential GW emission, we assume here that f-mode emission will be identified by such a minimally-modeled search.

In this paper, we explore the detectability of these f-mode signals. As detector sensitivity improves, the probability of detecting a GW signal from a non-compact-binary event increases. In the event such a signal is confidently observed, more sophisticated analysis, possibly including detailed waveform models, will be required to properly understand the underlying astrophysics. The goal of this paper is to provide a framework for follow-up study and potential parameter estimation for a future f-mode detection.

This paper is organized as follows: In Section 5.4, we discuss the various fitting functions and analytic models that can allow us to create a fuller picture of the gravitational waves from an f-mode. In Section 5.5 we will explore how this picture can be used to evaluate the plausibility of f-mode emission for detection candidates identified in a minimally modeled search such as X-Pipeline. In Section 5.5.1, we perform Bayesian analysis similar to that done by Clark, Heng, Pitkin, and Woan (2007) but extended to a larger frequency/damping time space and focused more on direct parameter estimation and future detector sensitivity. This section is also similar to recent work done by Pradhan, Pathak, and Chatterjee (2023); however, we focus on EOS-independent relations for f-modes from X-ray flares and consider recovery in the context of an initial, unmodeled search result. Finally, in Section 5.6, we will explore how these measurements stand to be improved with future detectors.

5.4 Methods

We consider a magnetar with a monochromatic oscillatory mode at frequency ν_{GW} spontaneously excited at time $t = 0$ and decaying with a timescale τ_{GW}. Following the derivation of Echeverria (1989) and Finn (1992), we can express the gravitational wave emission of an f-mode as a damped sinusoid of the form in Equation 5.1.

$$h(t) = \begin{cases} 0 & \text{for } t < 0 \\ h_0 e^{-t/\tau_{GW}} \sin\left(2\pi\nu_{GW} t\right) & \text{for } t \geq 0 \end{cases} \tag{5.1}$$

The emission is then characterized by an amplitude h_0, a characteristic frequency ν_{GW}, and a characteristic damping time τ_{GW}. While no model currently exists that properly describes the parameters (mass, radius, magnetic field strength) of this system due to the unknown neutron star equation of state (EOS), attempts have been made to form EOS-independent fitting functions to approximate these parameters. These fitting functions utilize numerical simulations to map such physical parameters to measurable quantities.

5.4.1 Frequency and Damping Time Fitting Functions.

A variety of attempts have been made to compute relationships between GW observables like frequency and damping time and physical properties like mass and radius. These typically involve performing numerical simulations at a variety of different EOS's and finding a best-fit function that relates these properties (see eg. Andersson et al. (2011); Andersson and Kokkotas (1996); Benhar, Ferrari, and Gualtieri (2004); Doneva, Gaertig, Kokkotas, and Krüger (2013); Gaertig and Kokkotas (2011); K. D. Kokkotas, Apostolatos, and Andersson (2001); Krüger and Kokkotas (2020); Tsui and Leung (2005)). We choose to consider the fitting functions of Andersson and Kokkotas (1998) (with an updated frequency function provided by K. Kokkotas (2023)) as most other calculations either arrive at similar results or they expand to include fast rotation – which we do not consider as none of the known magnetars are in this fast regime and the rotating fits converge to the non-rotating models in the zero spin limit. These fitting functions are shown in Equations 5.2 and 5.3 where $\overline{M} = M/1.4M_\odot$ and $\overline{R} = R/10\,\text{km}$.

$$\nu_{GW}(kHz) \approx 0.22 + 2.16\left(\frac{\overline{M}}{\overline{R}^3}\right)^{1/2} \tag{5.2}$$

$$\frac{1}{\tau(s)} \approx \frac{\overline{M}^3}{\overline{R}^4}\left[22.85 - 14.65\left(\frac{\overline{M}}{\overline{R}}\right)\right] \tag{5.3}$$

Assuming a mass range of [0.8 $M_\odot$, 2.5 $M_\odot$] and a radius range of [8 km, 20 km], this model allows f-modes to exist in the frequency range [0.80 kHz, 3.58 kHz] and damping time range [0.087 s, 10 s]. This includes constraints on the parameter space requiring the damping time and frequency to be positive (as the algebraic fitting functions would technically allow negative values) and for the mass and radius to satisfy Buchdahl's bound (Buchdahl, 1959). Since the algebraic fitting functions would technically allow damping times as high as 2500 s, we impose a constraint when sampling this parameter space that the damping time must be less than 10s as calculations predict damping times below this limit (Levin, 2006), and the numerical simulations the fitting functions were drawn from do not give damping times greater than this (Andersson & Kokkotas, 1998).

We note here that these relations do not give unique solutions for all frequency/damping times. For a small part of parameter space (roughly between 1800 − 2800 Hz and damping times below around 0.23 s), the same frequency/damping time can correspond to multiple mass/radius values.

5.4.2 Theoretically motivated amplitude model.

A simple Newtonian model can describe the amplitude of the oscillation. By modeling the oscillation as a reconfiguration of the internal magnetic field triggered by some impulse, the energy of an f-mode oscillation can be expressed as (Levin & Van Hoven, 2011)[2]

$$E_f = \frac{\epsilon_0^2 c^4}{128\pi^2} \frac{\alpha_n^2 B^4 R^4}{q_M M \nu^2} \tag{5.4}$$

where ϵ_0 is vacuum permittivity. Here, α_n represents the scale of the magnetic field reconfiguration, with $\alpha_n = 1$ corresponding to a complete reconfiguration of the entire field, and the quantity $q_M M$ is the effective mass of the oscillating mode, which is dependent on the specific equation of state, the mass, and the radius. The magnetic field strength B here is a characteristic value of the surface magnetic field of the magnetar[3].

[2] While the model presented by Levin and Van Hoven (2011) is Newtonian and the universal relations from Andersson and Kokkotas (1998) were constructed from fully general relativistic simulations, we believe that the uncertainty in how neutron star matter behaves outweighs these model differences. This same argument is made by Levin and Van Hoven (2011) when they combine the two sets of functions.

[3] This may not be the same magnetic field as estimated from spindown measurements which assume a dipole field subject to magnetic braking. The spindown measurements are where field strengths of order 10^{14} G come from, but this surface field value may be different.

We connect this energy to the peak amplitude in Equation 5.1 via the gravitational wave luminosity as a function of source distance given in equation 21 of Owen (2010) when including a damping term, and integrating from $t = 0$ to $t = \infty$ which gives Equation 5.5 as in (Ho et al., 2020).

$$h_0 = \frac{1}{\pi d \nu_{GW}} \left(\frac{5G}{c^3} \frac{E_{GW}}{\tau_{GW}} \right)^{1/2} \tag{5.5}$$

If we assume that all of the energy of the f-mode is radiated as gravitational waves (Detweiler, 1975; K. S. Thorne, 1969), then we can let $E_f = E_{GW}$ and combine Equations 5.4 and 5.5 to get a full description of the wave amplitude.

Given that α_n, q_M, and the magnetic field strength B are degenerate with each other, we can improve things by fixing B to the dipole magnetic field strength estimated from measurements of the spindown of the source magnetar (Olausen & Kaspi, 2014); however, this may not be the best choice since the surface field and the dipole field may be quite different. Nonetheless, if we let these fields be comparable, this constraint would allow us to incorporate information on the source magnetar into analyses and focus on the ratio of the reconfiguration scale α_n to the effective mode mass q_M which is related to the equation of state (Levin & Van Hoven, 2011). In the limit of a complete magnetic field reconfiguration ($\alpha_n \to 1$) and a mode mass in the range $0.02 < q_M < 0.07$, the amplitude of an f-mode oscillation computed using the above model agrees with the results of numerical simulations for oscillations due to magnetic re-configurations performed by Lasky et al. (2012).

The degeneracy in mass/radius mentioned in Section 5.4.1 can be potentially broken by this amplitude term. Since the amplitude has a dependence on these parameters through the frequency and damping time, the degeneracy can be eliminated to some extent by constraining the magnetic field if that information is known.

5.5 Applications in GW Scenarios

In the event search pipelines do find an astrophysical candidate, it is desirable to connect the putative candidate with astrophysical source parameters. We can construct three levels of analysis for different degrees of candidate strength. In the event the candidate is of high enough amplitude to perform full Bayesian parameter estimation, we need to know what level of precision source parameters can be extracted and what thresholds need to be met to perform further analyses. In the event a candidate event is detected, but too weak for full Bayesian parameter estimation, we need some method of determining source parameters without full parameter estimation. Finally, in the event a search returns no GW candidates, we consider any interesting limits on astrophysical parameters.

5.5.1 Usage in a Full Detection. A full detection would take the form of a search result with sufficiently high probability of an astrophysical source. In this case, we consider how to extract astrophysical information from the data. In particular, we can make statements on the consistency of the signal with an f-mode with reasonable astrophysical parameters.

$$\begin{aligned} h_+(t) &= \frac{1}{2}\left(1+\cos^2\iota\right)h(t) \\ h_\times(t) &= \cos\iota\, h(t) \end{aligned} \tag{5.6}$$

If we include a Newtonian quadrupole inclination term in our model to transform from the linearly polarized source frame to the detector frame, we differentiate plus and cross polarization amplitudes (Equation 5.6 where ι is the angle between the quadrupolar axis and the line of sight – see K. Thorne (1987)).

This allows us to use the fitting functions as forward model for full parameter estimation.

We evaluate the recoverability of various f-mode waveforms using the BILBY Markov-Chain Monte Carlo infrastructure (Ashton et al., 2019) and the LALINFERENCE package (Veitch et al., 2015). This lets us identify the range of parameter space where a signal inserted into simulated detector noise can be recovered and with what level of confidence. A range of signals was generated using the model presented above and coherently injected into simulated, Gaussian detector noise using packages in LALINFERENCE with noise sensitivity estimates for the third observing run (Buikema et al., 2020). Using the known location and sensitivity of the two LIGO detectors, we construct simulated background noise for each detector. The source orientation and sky location of injected signals were chosen to optimize the response of this network of detectors. We consider a galactic source at a distance of 10 kpc. We then used BILBY to attempt to recover the parameters of the injected signals.

Injections were performed over a somewhat physically motivated parameter space, with masses ranging from 1.0 to 2.6 $M_{\odot}$, radii ranging from 10 to 14 km, and surface magnetic field strengths ranging from 10^{14} to 10^{17} G – which is beyond what is generally considered possible, but may not be that optimistic in light of more recent measurements of field strengths above 3×10^{16} G (Sob'yanin, 2023). All injections were performed assuming a fixed distance of 10 kpc as mentioned above, an optimal inclination angle, and a fixed sky location, chosen to maximize the antenna response in both LIGO detectors. This represents a best-case detection scenario such that the limiting factors of recovery would be intrinsic source parameters. This is also consistent with previous GW searches (B. P. Abbott et al., 2019; R. Abbott et al., 2024b).

For our simulated recoveries, the prior distributions for the core parameters were as follows: mass was uniform from 0.5 to 3.0 $M_\odot$, radius was uniform from 8 to 16 km, and the magnetic field was log uniform from 10^{13} to 10^{17} G. We also assumed a full magnetic field reconfiguration such that $\alpha_n = 1$, as this gives the maximum f-mode amplitude in this model. These priors are wider than the range of injections to allow for proper sampling.

A general quantity used to reflect the amplitude of a signal is the integrated root sum squared strain $h_{\rm rss}$ (Equation 5.7). This quantity can be compared to the background amplitude spectral density of the detectors at the peak frequency of the signal (see eg. R. Abbott et al. (2021a) and R. Abbott et al. (2024b) for recent analyses).

$$h_{\rm rss}^2 = \int_{-\infty}^{\infty} \left|\tilde{h}_+(f)\right|^2 + \left|\tilde{h}_\times(f)\right|^2 \mathrm{df} \tag{5.7}$$

For each injection recovery, BILBY produced a log Bayes factor [4] for how well the model was preferred over the null hypothesis. The set of injection recoveries are shown in Figure 28. Each injection is shown as a single point in frequency-$h_{\rm rss}$ parameter space, corresponding to the frequency of the damped sinusoid (Equation 5.2) and the $h_{\rm rss}$ of the waveform (Equation 5.7), respectively. The points are colored by the log Bayes factor with a color scale centered on a log Bayes factor of 8. This value of 8 is typically chosen as the threshold of 'strong evidence' (Jeffreys, 1998), so we consider this our threshold for recovery. In this regime, injections that were recovered with confidence are colored red, and those

[4] All log Bayes factors reported in this paper are in the natural log.

that were not recovered are blue. This gives an approximate $h_{\rm rss}$ threshold of 3×10^{-23} Hz$^{-1/2}$. In a frequency-independent picture, Figure 29 shows how the log Bayes factor directly compares to the optimal matched-filter signal-to-noise ratio (SNR) of the injections and shows the clear recoverability threshold SNR of 8. The SNR is computed in the standard method in Equation 5.8 where $\tilde{h}(f)$ is the Fourier transform of the waveform and $S_h(f)$ is the background noise spectral density. This is similar to the thresholds estimated by Clark et al. (2007).

$$\rho^2 = 4 \int_0^\infty \frac{\tilde{h}^*(f)\tilde{h}(f)}{S_h(f)} \mathrm{df} \tag{5.8}$$

Due to fluctuations in detector noise, the log Bayes Factor is not a fixed value. We performed 100 additional injection recoveries with different realizations of the background noise for a single set of parameters near the recovery threshold and find that the log Bayes Factor can fluctuate with a standard deviation of $\pm 35\%$. When we repeat this for a set of parameters recovered with higher confidence (log Bayes Factor of around 1000), the effect decreases to $\pm 4.5\%$. This level of error does not significantly affect our results.

In terms of recovery accuracy, above an SNR of 8, the true injected mass and radius values were within the 90% confidence interval of the recovered posterior distributions for each injection but the width of this confidence interval was frequency-dependent due to detector sensitivity. For example, one injection with $(\mathrm{M}, \mathrm{R}) = (1.0 M_\odot, 14\mathrm{km})$ at a frequency of approximately 1600 Hz with a magnetic field of 3×10^{16}G had an SNR of 13. This injection was recovered with a 90% confidence interval $(\mathrm{M}, \mathrm{R}) = (1.13^{+0.18}_{-0.18} M_\odot, 14.9^{+0.9}_{-1.0}\mathrm{km})$. Another injection with $(\mathrm{M}, \mathrm{R}) = (1.8 M_\odot, 14\mathrm{km})$ at a frequency of approximately 1900 Hz with a magnetic field of 3×10^{16}G had an SNR of 16. This injection was recovered with

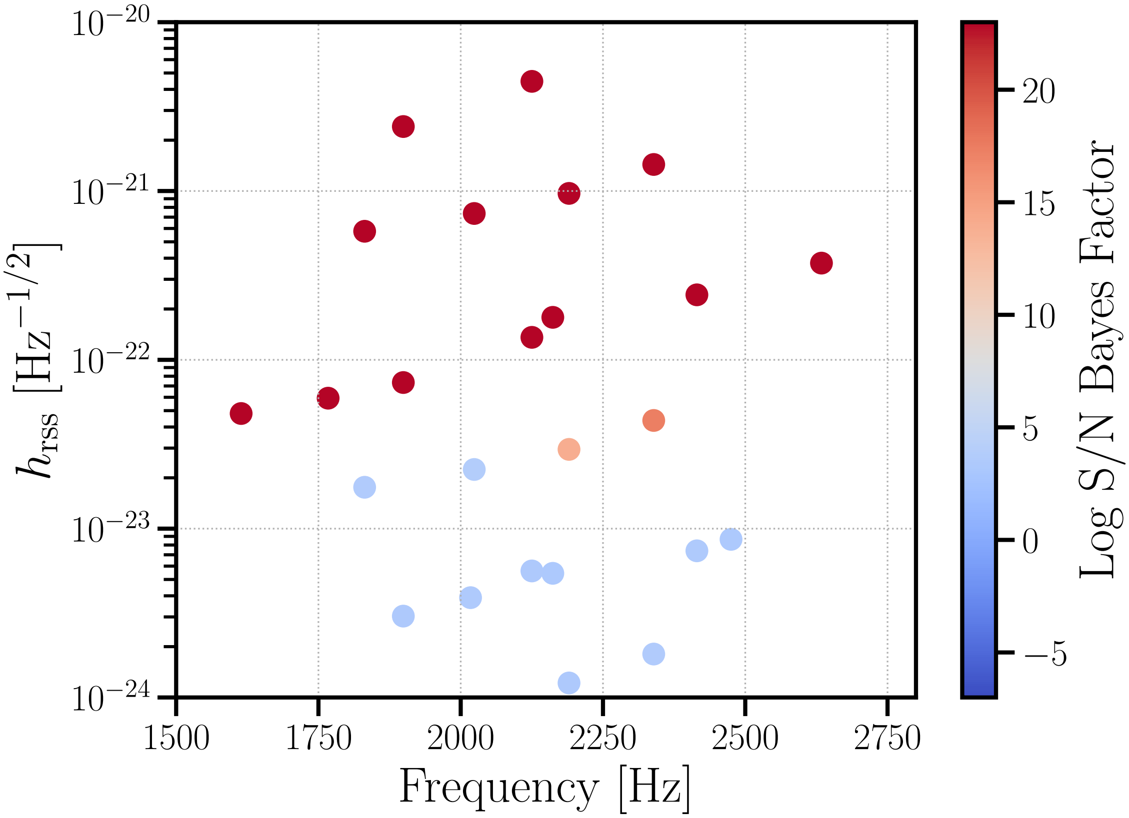

Figure 28. Frequency space representation of injection recoverability for the LIGO H1-L1 network at the sensitivity of the third observing run (Buikema et al., 2020). Each point represents one injection, identified by the frequency and $h_{\rm rss}$ of the signal and the log Bayes factor of the recovery. The $h_{\rm rss}$ threshold for recovery is around 3×10^{-23} Hz$^{-1/2}$. The color scheme of the log Bayes factor is truncated at 22 to emphasize the recovery point despite many injections recovered with far higher log Bayes factors.

$(\mathrm{M}, \mathrm{R}) = (1.9^{+0.5}_{-0.4} M_\odot, 14.7^{+1.1}_{-1.4}\mathrm{km})$. The difference in SNR here is due to the effect of the mass and the frequency on the amplitude.

Since real detector noise contains non-Gaussian elements (Davis et al., 2021), the use of Gaussian noise here means this represents an optimistic scenario, and any attempts to recover a signal from real data will likely see a higher $h_{\rm rss}$ threshold for recovery. The analysis done here is meant to form a baseline for later examination of predicted sensitivity curves of future detectors (see Section 5.6).

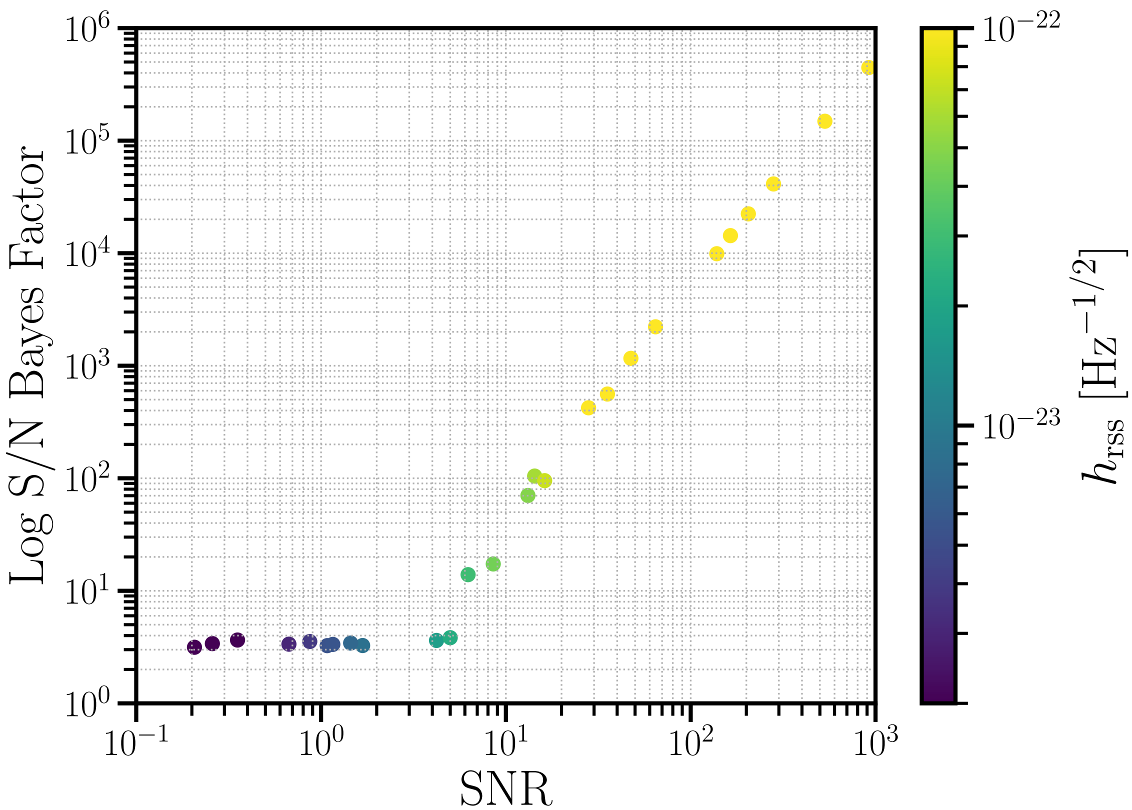

Figure 29. Matched-Filter SNR vs log Bayes factor for a range of signals injected into simulated Gaussian noise for the LIGO H1-L1 network at the sensitivity of the third observing run (Buikema et al., 2020). Injected signals ranged in mass, radius, and magnetic field strength, but given a known distance of 10 kpc. The log Bayes factor sharply increases at an SNR of 8.

5.5.2 Usage in a Marginal Detection.

A marginal detection may take the form of a search result where a pixel cluster is identified by X-Pipeline as a candidate, but the probability of an astrophysical source is near or just below the threshold for proper detection. In this case, full Bayesian parameter estimation is unlikely to give log Bayes factors above 8, and analyses will be limited to what could be allowed given the time-frequency range identified by the search. Preliminary estimates of the signal morphology could be made with an unmodeled, coherent signal reconstruction algorithm like BayesWave (Cornish & Littenberg, 2015) which attempts to reconstruct a signal coherent between different detectors using Morlet–Gabor wavelets. If this reconstruction results in a waveform similar in morphology to the model discussed earlier, we can use it to make estimates for the range of astrophysical parameters permitted by the time-frequency shape of the candidate despite not being able to perform full Bayesian parameter estimation.

Under a hypothetical analysis, we can use Monte Carlo techniques to generate random f-mode waveforms based on physically motivated source distributions and check if these could match the time-frequency range of a marginal candidate. Without amplitude restrictions (as search algorithms rely nearly entirely on coherence statistics), the frequency range of a marginal candidate can be used to place constraints on what astrophysical parameters would allow such a candidate if it were an f-mode. Figure **??** shows what the mass-radius restriction looks like for hypothetical frequency ranges centered on different central frequencies of 1.5, 2.0, and 2.5 kHz using Equation 5.2.

Including damping time constraints using Equation 5.3 could allow analyses to focus in on where in the mass-radius band the source could exist, but determining damping time from the time duration of the trigger is not an obvious task. Time-frequency pixel clusters identified by X-Pipeline show the precise amount of time that the loudest 1% of pixels were clustered together, which is not necessarily the decay time of a damped sinusoid. We can make preliminary estimates for an analysis, such as limiting the damping time to some range of values estimated from the cluster duration. We may be able to increase accuracy via signal reconstruction algorithms like BayesWave, which may be able to more precisely estimate the damping time and constrain our model estimates. If there is a candidate duration of several tens of seconds, it is unlikely that it could be adequately explained by this model. In Figure **??**, we demonstrate how the parameter space can be constrained with estimates of frequency and damping time. Shaded regions show examples of how a frequency-only limit can constrain the mass-radius parameter space. This constraint can be further refined with the damping time constrained to some range, representative of a limit consistent with uncertainties from X-Pipeline. This is shown by the black-dashed regions in the plot.

5.5.3 Usage in a Non-Detection. In the event that there are no confident candidates returned by the search, astrophysical information can still be extracted from the non-detection. Previous searches (Abadie et al., 2011a; B. Abbott et al., 2007; B. P. Abbott et al., 2019; R. Abbott et al., 2024b; Macquet, Bizouard, Burns, et al., 2021) have placed h_{rss} limits at 50% and 90% detection efficiency on the signal via injections at different frequencies (which we will refer to as "50%" or "90% upper limits" respectively for the remainder of this paper). In our hypothetical analysis, we use the 50% upper limits to constrain the amplitude of a signal and sample our physically motivated parameter space with the only restriction being that the h_{rss} at some frequency is below the upper limits set by

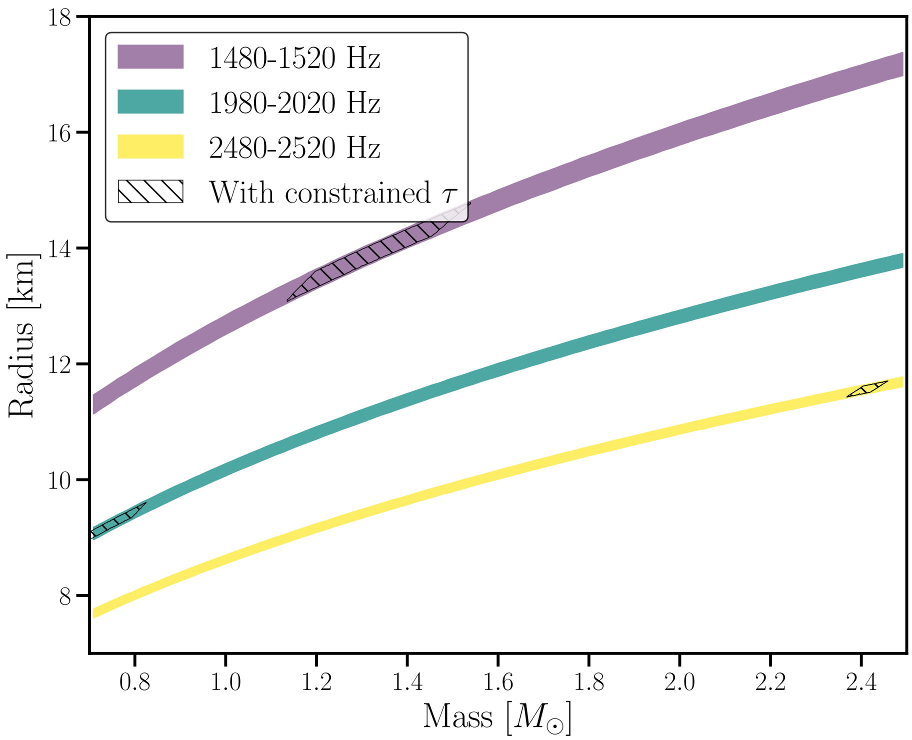

Figure 30. Physically plausible parameter space for a signal given frequency limits from a targeted, unmodeled, search using simulated data. Masses and radii for different f-modes were generated and those with frequencies permitted by simulated search results are shown. Narrow frequency ranges around central frequencies of 1500, 2000, and 2500 Hz show clear mass-radius relations that can be extracted from a potential marginal detection. Marked regions are when we assume the damping time can be constrained to a range of $0.3\,\mathrm{s} < \tau < 0.4\,\mathrm{s}$, representative of limits that might be placed from an X-Pipeline detection.

the search and a maximum damping time of 10 s. Since the source distance is likely known, this primarily can place limits on the three degenerate terms: magnetic field strength B, scale of magnetic reconfiguration α_n, and oscillation mode mass fraction q_M.

If the dipole magnetic field estimated from spindown measurements is assumed to be equal to the surface magnetic field that modulates the amplitude of the f-mode, some of the degeneracy of the model can be removed. In this case, α_n and q_M may have limits placed. Further constraints can be placed by restricting the mode mass to values calculated for modern equations of state allowing for limits to be placed on the scale of magnetic reconfiguration.

Figure 31 shows an example of a comparison we can make in the event of a non-detection in a hypothetical analysis. 50% upper limits for the h_{rss} of short-duration waveforms for a non-detection from a flare potentially associated with 1 RXS J170849 (as done in R. Abbott et al. (2024b)) at a distance of 3.8 kpc are compared to what the model would allow for a hypothetical magnetic field of 10^{15} to 10^{16} G. The maximum allowed h_{rss} meets the search upper limits at low frequencies in this example, which might suggest that a low-mass, high-radius neutron star (required for a lower frequency) is right at the threshold of detectability. The upper limits are also scaled to the predicted sensitivity of future observing runs and detectors (Barsotti et al., 2018a; Buikema et al., 2020; Srivastava et al., 2022; The LIGO Scientific Collaboration, 2022). LIGO A+ (O5) and 3rd generation detectors like Cosmic Explorer (CE) will have the potential to place strong exclusion limits on the allowed parameter space in the event of non-detections. This is a very optimistic scenario, as of the 30 known magnetars, only one has a magnetic field in this range, and of the magnetars with known distances,

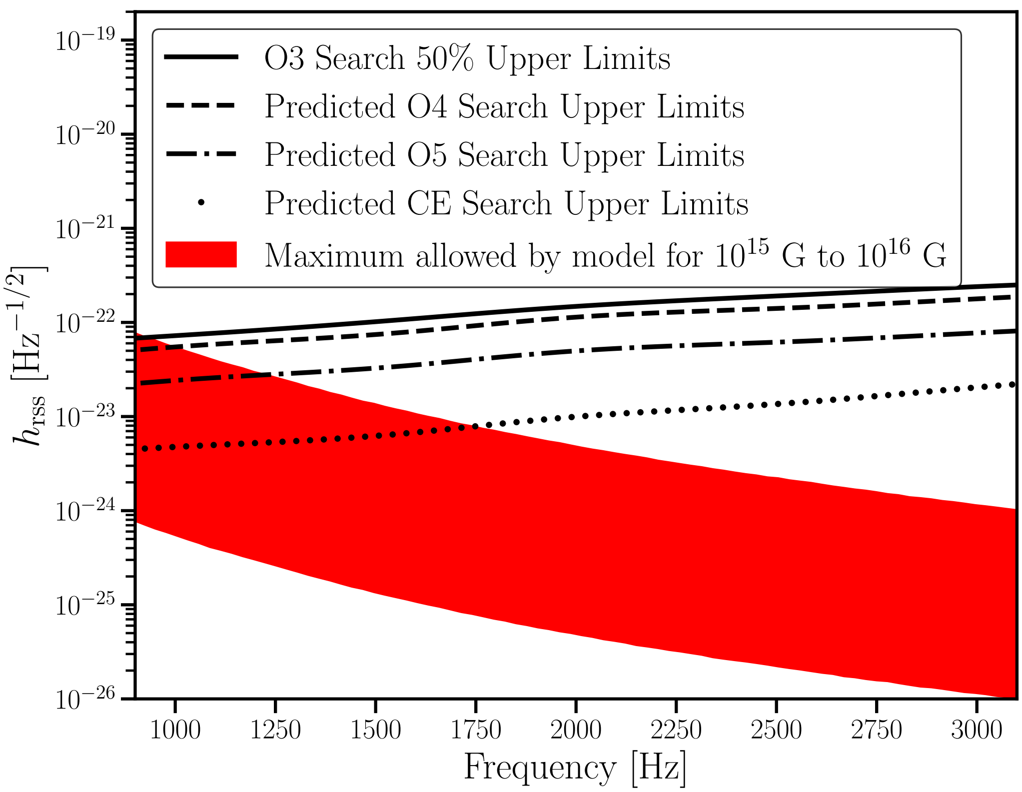

Figure 31. Example results using interpolated 50% upper limits from one target of the search in the third observing run (R. Abbott et al., 2024b) with an estimated source distance of 3.8 kpc, assuming a magnetic field of between 10^{15} to 10^{16} G (far greater than the estimated field strength of the original source). The red region shows the maximum allowed $h_{\rm rss}$ when forcing the mode mass fraction to be 0.046 for the SLy equation of state (as calculated in Levin and Van Hoven (2011)) and the magnetic field reconfiguration scale to be 1 for a complete field reconfiguration. The damping time was only constrained to less than 10 s, allowing for multiple mass/radius combinations per frequency. Projections of these upper limits onto future detector sensitivities are also shown.

only about six are comparable to or nearer than this distance (Olausen & Kaspi, 2014).

5.5.4 Something Unexpected. In the event a candidate is present that exists outside of the parameter space allowed by f-mode models, a few scenarios can be considered. A first approach for an unexpected candidate would be to attempt to extract a general waveform using an unmodeled reconstruction algorithm like BayesWave (Cornish & Littenberg, 2015). With a candidate reconstruction, the $h_{\rm rss}$ and the gravitatitonal-wave energy assuming isotropic emission from the source trigger distance can be calculated. From this energy estimate, energetics arguments could be made about whether or not the candidate is astrophysically plausible. Corsi and Owen (2011) estimated the limits of energies that an internal magnetic reconfiguration could reach. The energy of an f-mode is limited by the energy released by changes in magnetic deformation, so a magnetic reconfiguration that drives an f-mode cannot expend more energy than available in the reservoir. If the energy of a candidate exceeds what can possibly be stored in the deformation reservoir, it is unlikely to be physical.

If a short-duration, monochromatic candidate is found that occurs outside of the allowed frequency space of this model, it may be possible to make arguments that the candidate was due to a different vibrational mode of the neutron star. While the f-mode models considered here are believed to be most likely for GW emission (Detweiler, 1975; McDermott et al., 1988), frequencies above a few kHz are expected to be where one might find higher order pressure modes (p-modes) (Andersson & Kokkotas, 1998). Frequencies below 1 kHz are where Alfvén modes are predicted that are potentially associated with quasi-periodic oscillations observed in electromagnetic measurements. However, these are complex and have not been fully modeled (Lasky et al., 2012). Crustal and shear modes are also hypothesized to occur in this range (Duncan, 1998; Piro, 2005), as are g-modes with buoyancy as the restoring force (Reisenegger & Goldreich, 1992), though these are unlikely to decay via the emission GWs as efficiently as the f-mode (McDermott et al., 1988).

Another possibility is a candidate with appropriate frequency and duration but with an amplitude exceeding what the model allows. In the search for GWs associated with flaring magnetars in the third observing run of the LIGO-Virgo-KAGRA collaboration, the most significant candidate was a short burst of bright coherent pixels between 1560 and 1608 Hz lasting 63 ms (R. Abbott et al., 2024b). The frequency and duration fall right in the region expected for an f-mode, but the burst candidate was excluded as an astrophysical candidate for data quality reasons. However, it is instructive to consider what it would imply if the burst candidate had not been a data quality artifact.

While the frequency constraint of 1560 - 1608 Hz fits well within the model discussed here, a damping time of 63 ms is below the minimum damping time allowed by the model. If we consider the case where less than one complete damping time was detected by a search pipeline, then we could have a damping time greater than this value. The source magnetar for the triggering flare was SGR 1935+2154 which has an estimated dipole magnetic field strength of 2.2×10^{14} G (Israel et al., 2016) and an estimated distance of 9.0 ± 2.5 kpc (Zhong, Dai, Zhang, & Deng, 2020). If we sample this physically motivated part of parameter space, we get a maximum h_{rss} of $\sim 7 \times 10^{-27}$ Hz$^{-1/2}$ and a maximum isotropic energy of 1.5×10^{31} ergs at 9.0 kpc. This is well below the 50% upper limits set by the search at 1.1×10^{-22} Hz$^{-1/2}$ at 1600 Hz (R. Abbott et al., 2024b). If an astrophysically motivated model with the same time-frequency shape as a candidate has an h_{rss} over 4 orders of magnitude below the candidate, the candidate is either not astrophysical, or not described by the f-mode model. The discrepancy here demonstrates the ability of the model to help vet potential candidates with a more astrophysical motivation.

Another way of thinking about the burst candidate is that to get the astrophysically motivated model to match the amplitude set by the upper limits of the search, the magnetic field strength would need to be increased by about 2 orders of magnitude and the distance reduced to about 4 kpc. While not astrophysically feasible as an f-mode event for the targeted magnetar (SGR 1935+2154 at 9.0 ± 2.5 kpc), the burst candidate would not be unfeasible within the context of this f-mode model for a magnetar at the distance of 1 RXS J170849 (3.8 kpc) but with a magnetic field of $\sim 10^{16}$ G, which is at the very upper limit of what magnetars could reach in some estimates (Sob'yanin, 2023). Likewise, if it were due to magnetar with 10^{15} G at a distance of 10 pc – which is about 100 times closer than the nearest magnetar, it could also be consistent with the model.

5.6 Discussion and Conclusions

The relationship between SNR and log Bayes factor shown in Section 5.5.1 allows us to estimate sensitivity to potential signals for future detectors. Using predicted detector sensitivities (Barsotti et al., 2018a; Buikema et al., 2020; Srivastava et al., 2022), we can quantify how future detectors will improve searches for these signals.

Figure 29 shows that at a matched-filter SNR of about 8, the log Bayes factor spikes to nearly 10 for injection recovery. We can compute what signal parameters would give a particular SNR using predicted future detector sensitivity estimates to investigate the prospects for future observing runs. Figure 32 shows the frequency-distance parameter space for a giant flare-induced f-mode with a fixed surface magnetic field strength of 10^{16} G and magnetic reconfiguration scale of 1, allowing the mass, radius, and effective mass of the oscillating mode to vary within astrophysically motivated ranges, where at least 10% of the randomly generated waveforms in a distance-frequency bin have an SNR greater than 3. This $3\,\sigma$ threshold was chosen to correspond to the p-value threshold used for potentially interesting X-pipeline clusters to follow-up on, which is about 1% (Sutton et al., 2010). A giant flare from a high-magnetic field magnetar is similar to what was observed from SGR 1806-20 – though it has a slightly weaker field strength (Hurley et al., 2005). The strong frequency dependence is primarily due to the frequency dependence of the sensitivity curves of the detectors. This parameter space represents what searches might expect to see in the event of a possible candidate: a known source distance, and a frequency space for the candidate. By comparing a potential candidate with the potential detection ranges for different detectors, we can make astrophysical arguments about why a signal may or may not be an f-mode. The loudest candidate from the third observing run (R. Abbott et al., 2024b) described in Section 5.5.4 is included for comparison.

Here, we have demonstrated applications for a more complete description of the gravitational wave emission from neutron star f-modes associated with magnetar X-ray flares. We have shown that in simulated LIGO noise, full parameter estimation may be possible above a matched-filter SNR of 8 which occurs at an h_{rss} of around $3 \times 10^{-23}\,\mathrm{Hz}^{-1/2}$ at the sensitivity of the third observing run. We have shown the limits that could be placed on a mass-radius relation in the event of a marginal detection with just frequency information. We have

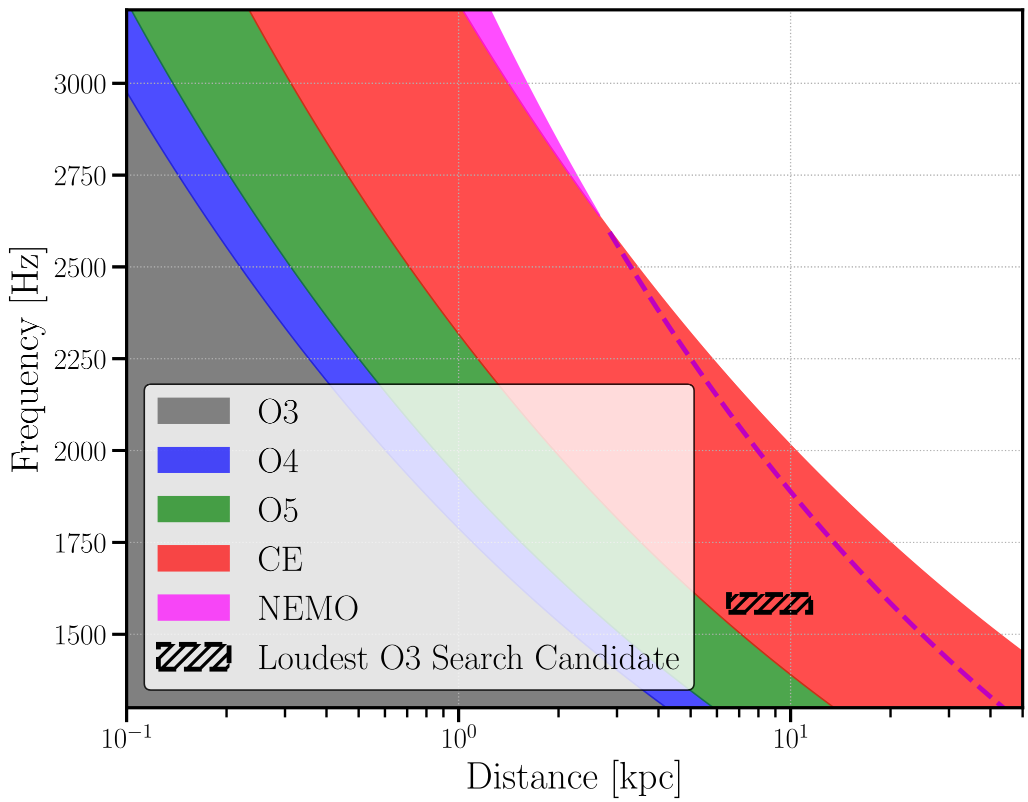

Figure 32. Regions of the distance-frequency parameter space that future detectors could be sensitive to assuming a complete magnetic field reconfiguration and source magnetic field strength of 10^{16} G. The parameter space used in section 5.5 was sampled and binned in signal frequency and distance. The fraction of samples in each bin with an expected SNR above a threshold of 3 was calculated, and the region where at least 10% meet this threshold are shaded. The strong frequency dependence is primarily due to the frequency dependence of the sensitivity curves of the detectors. Potential detections can be compared to such a calculation to vet the plausibility of a real signal. The loudest candidate from the analysis in the third observing run (O3) is marked as a dotted box and falls squarely within the Cosmic Explorer and NEMO detection thresholds. This suggests that for such a candidate to have been from a magnetar f-mode with realistic source parameters, the detector would have needed to be at third generation detector sensitivity. Due to the considerable similarity in this frequency regime between Cosmic Explorer and the Einstein Telescope, only the Cosmic Explorer estimate is shown to represent these third generation detectors (Hild et al., 2011; Srivastava et al., 2022). It is also worth noting that NEMO is comparable to third generation detectors in the frequency space of these signals and should prove quite useful in future analyses (Ackley et al., 2020).

demonstrated how non-detections may be able to constrain the astrophysical parameter space as sensitivity improves. We have also explored how this model can be used to vet potential candidates using astrophysically motivated predictions. Lastly, we have shown how the available search space will improve with the increased sensitivity of future detectors.

CHAPTER VI

METHODS FOR ESTIMATING NEUTRON STAR PARAMETERS USING MULTIPLE MECHANISMS FOR GRAVITATIONAL WAVE EMISSION ASSOCIATED WITH PULSAR GLITCHES

6.1 Forward

Motivated by news of the April 2024 Vela glitch, this chapter expands upon the methods developed in the previous chapter for deriving astrophysical implications from a neutron star f-mode. The f-mode model is slightly different due to the different source (pulsar glitch vs magnetar flare). This source was promising due to how close the Vela pulsar is (287 pc compared to > 1 kpc for the average magnetar). Since the LIGO Continuous Wave subgroup was planning on running a search as well, I decided to look into how I might be able to fold their search results in as well. This chapter contains as yet unpublished work (Ball & Frey, in prep.).

6.2 Abstract

Pulsar glitches are believed to be associated with the emission of gravitational waves (GWs). This emission may be split between long duration continuous waves and short duration bursts. Searches for GWs associated with pulsar glitches have previously only considered one emission mechanism and place observational limits based only upon that mechanism. The increasing sensitivity of the detectors and the prospects of future detectors suggest that more astrophysically motivated analyses may be necessary. Here, we present a framework for combining two simple models for GW emission - long duration continuous waves and short duration bursts - to derive more constraining astrophysical implications than a single model would allow. We apply these methods to the December 2016 Vela pulsar glitch and make predictions for how well future observing runs and

detectors would improve results. As part of this analysis, we performed a direct search for GW bursts associated with this glitch and find no signal.

6.3 Introduction

Neutron stars are comprised of matter potentially exceeding nuclear density, but the details are poorly understood. Gravitational waves (GWs) present a promising probe into this exotic matter. There are many methods through which a neutron star can emit GWs, but one particularly promising mechanism is a glitching pulsar (Haskell, 2017; Link, Epstein, & Van Riper, 1992).

Pulsar rotation is typically a slowly varying process, but glitches are sudden changes in the rotation rate without a clear cause (Fuentes et al., 2017). Models have been proposed (Haskell & Melatos, 2015), but the precise mechanism is still poorly understood. These models typically describe some purely internal mechanism that induces a spontaneous change in the star's moment of inertia. This would account for the lack of measurable emission and the sudden change in the rotation rate. A rearrangement of matter capable of changing the moment of inertia could create the necessary conditions for the emission of GWs.

Pulsar glitches have been considered for gravitational wave sources since the early days of LIGO (Abadie et al., 2011b). Modern searches are designed to separately target both long and short duration GWs using dedicated search algorithms. Long duration searches focus on GWs with durations lasting from hours to months (Keitel et al., 2019), and no targeted short duration searches have been performed on pulsar glitches recently (although all-sky searches for GWs potentially associated with pulsar glitches have been performed (R. Abbott et al., 2021b; Lopez & the LIGO, Virgo, and KAGRA collaborations, 2024; Lopez et al., 2022)). The techniques that would be used to search for short-duration GWs from pulsar glitches would be similar to or the same as searches that target other transient neutron star phenomena such as magnetar flaring (see e.g. R. Abbott et al. (2024c); Macquet, Bizouard, Burns, et al. (2021)), and as described in the previous chapter.

Given that there is interest in both long and short duration GWs from pulsar glitches, the question may naturally arise: what information is gained by combining these emission mechanisms? Both types of emission are potentially attributable to the same type of object, so in the event of a pulsar glitch, the same source could emit both long and short duration GWs. This means that there should be an overlapping set of astrophysical parameters, and the combination of measurements from both types of search should place stronger limits on parameters of the pulsar. This paper seeks to combine measurements of both long and short duration GWs from a common pulsar glitch to place stronger constraints on the astrophysical parameters than those attainable by considering the two sets of results separately.

This paper is organized as follows. In Section 6.4.1, we describe the analysis techniques that would be used in a targeted glitch search. Then, in Section 6.4.2, we detail the GW waveform models we will consider for astrophysical implications. In Section 6.5, we describe how we use the results of a search to inform a Monte Carlo simulation to explore the parameter space permitted by the observations. In Section 6.6, we apply these methods to the 2016 Vela pulsar glitch, which occurred during LIGO's second observing run. Finally, in Section 6.7, we consider what measurements made with more sensitive detectors may teach us.

The analysis we consider here consists of two distinct steps: an initial set of searches and the inference of astrophysical parameters from the search results. We give a brief overview of standard search techniques, but the main focus of this work is the interpretations step.

6.4 Background

6.4.1 Search Techniques. Since the two GW emission models are very different in time scale, they require different search techniques. Here, we discuss the search techniques used for each type of signal and give a more detailed description of the waveforms of interest.

The two primary waveforms take the form of slowly decaying sinusoids: a longer duration, continuous wave created by the decay of an induced ellipticity in the neutron star, and a very short duration wave created by pressure oscillations within the neutron star.

The slowly decaying waveform is expected to occur at twice the rotation rate and damp out on the scale of days. This model is often referred to as the "mountain" model.

The short-duration waveform is expected to occur in the range of 1000 to 3000 Hz and damp out in under a second. This oscillation is referred to as the "f-mode."

6.4.1.1 Search for Continuous Waves. The long-duration search for Continuous Waves (CW) integrates days of data to perform a very narrowband search around 1× and 2× the neutron star rotation frequency. The primary search pipeline is the matched-filter transient $\mathcal{F}$-statistic search algorithm (implemented in PyFstat) (Ashton, Keitel, Prix, & Tenorio, 2020). This algorithm is designed to report the dimensionless strain amplitude h_0 of the GW with a maximum likelihood (Jaranowski, Królak, & Schutz, 1998; Prix, Giampanis, & Messenger, 2011).

In the event of a non-detection, the pipeline places limits on the amplitude that could have been detected. PyFstat performs signal injections of different durations to measure how well the algorithm recovered them. These take the form of sigmoid-like curves of the fraction of recovered waveforms at different values of h_0. The value of h_0 at around 90% detection efficiency is usually reported as the "upper limit."

In previous searches, astrophysical implications generally take the form of estimating what fraction of the glitch energy could have been emitted as gravitational waves. Upper limits are compared to the spindown limit assuming that all available glitch energy was radiated away through the GW emission. The energy of the spindown limit is given by Equation 6.1 (eg. Prix et al. (2011)) where $h_0(t)$ is the time-dependent peak amplitude of the signal. The upper limits of the search are then compared to this spindown limit (see eg. Keitel et al. (2019)).

$$E_{\mathrm{GW}} = \frac{2\pi^2 c^3}{5G} d^2 f^2 \int^T h_0(t)^2 \mathrm{dt} \tag{6.1}$$

6.4.1.2 Search for Gravitational Wave Bursts. The short-duration search for burst signals looks at multi-detector time-frequency correlations in the seconds to minutes after the glitch time, targeting GW frequencies in the range of $\sim$ 100Hz to 4000Hz. These searches are minimally modeled to account for unexpected waveforms. Two primary algorithms for this are Coherent WaveBurst (cWB) (Drago et al., 2021; Lopez et al., 2022) and X-Pipeline (Sutton et al., 2010; Wąs et al., 2012). Both of these searches, in the case of a detection, would return time-frequency ranges of the signal with an associated integrated root-sum-square strain h_{rss} (Equation 6.2).

$$h_{\mathrm{rss}}^2 = \int_{-\infty}^{\infty} \left|\tilde{h}_+(f)\right|^2 + \left|\tilde{h}_\times(f)\right|^2 \mathrm{df} \tag{6.2}$$

In the case of a non-detection, waveform injections are performed over a range of different signal morphologies. For the purposes of this analysis, we will only consider the ringdown waveforms, as they are most similar to the damped sinusoid shape associated with f-modes.

Standard analyses report upper limits on the strain and compare them to the energy estimated by electromagnetic observations. For burst searches, the h_{rss} upper limits would be converted to an energy assuming emission via Equation 6.3 (Sutton, 2013). This would then be converted to an estimate of the glitch energy (Equation 6.4) using a fiducial value for the moment of inertia (for instance $\mathcal{I}_{zz} = 10^{45}\mathrm{g\,cm^2}$) to predict how close to detection the source was (see eg. **?**).

$$E_{\mathrm{GW}} = \frac{2\pi^2 c^3}{5G} d^2 f_0^2 h_{\mathrm{rss}}^2 \tag{6.3}$$

6.4.2 GW Waveform Models. In order to make quantitative claims about neutron star source parameters when there is no detection, we need to make an assumption of a model for each emission mechanism. Here, we consider the "mountain" model for CW emission, where the glitch induces some ellipticity that slowly damps out, and a simple damped sinusoid for the f-mode emission.

In both cases, we assume some fraction of the total glitch energy E_{Glitch} is emitted in the respective channel. The total glitch energy is given by Equation 6.4 where $\mathcal{I}_{zz}$ is the moment of inertia, ν_s is the rotation rate of the neutron star, and $\Delta\nu_s$ is the change in rotation rate from the glitch.

$$E_{\mathrm{Glitch}} = 4\pi^2 \mathcal{I}_{zz} \nu_s \Delta\nu_s \tag{6.4}$$

Whereas previous searches have used a fiducial value of $10^{45}\mathrm{g\,cm}^3$ for $\mathcal{I}_{zz}$, we will use the equation of state independent relation in Equation 6.5 to relate the moment of inertia to direct mass and radius estimates (in geometric units where $a_1 = 1.317$, $a_2 = -0.05043$, $a_3 = 0.04806$, and $a_4 = -0.002692$) (Yagi & Yunes, 2017).

$$\frac{I_{zz}}{M^3} = \sum_{k=1}^{4} a_k \left(\frac{M}{R}\right)^{-k} \tag{6.5}$$

6.4.2.1 CW Waveform. The mountain model suggests that the sudden change in rotation rate associated with the glitch induces an ellipticity ϵ which slowly damps out through the emission of GWs, initially suggested by Prix et al. (2011). This amplitude is parameterized in Equation 6.6, where ϵ is the ellipticity.

$$h_{0,mtn} = \frac{4\pi^2 G}{c^4} \mathcal{I}_{zz} \frac{(2\nu_s)^2}{d} \epsilon \tag{6.6}$$

Note that this is independent of the decay time. The amplitude limits set by these searches in the past are often compared to the spin-down limit, which is the limit where all energy from the loss of angular momentum in the glitch (Equation 6.4) is emitted over the course of some damped decay.

An amplitude can be calculated by integrating the GW luminosity as a function of distance for a damped sinusoid. We use the relatively simple model proposed by Yim and Jones (2020) to parameterize the emission. Equation 6.7 shows the spindown limit and its relation to the total energy emitted by the waveform. Here, τ_{CW} is the damping time of the waveform. Previous searches for CWs near Vela pulsar glitches have placed upper limits on h_0 at approximately $1 - 2 \times 10^{-24}$ for signal durations of around 100 days (Keitel et al., 2019).

$$h_{0,SD} = \frac{1}{2\pi d\nu_s}\sqrt{\frac{5GE_{\text{Glitch}}}{c^3\tau_{CW}}} \tag{6.7}$$

6.4.2.2 f-mode Waveform. We consider f-mode GW emission in the form of a monochromatic damped sinusoid parameterized by a frequency ν_f and a damping time τ_f, excited at time $t = 0$. This follows the parametrization of Echeverria (1989) and Finn (1992) and is shown in Equation 6.8.

$$h(t) = \begin{cases} 0 & \text{for } t < 0 \\ h_{0,f}e^{-t/\tau_f}\sin(2\pi\nu_f t) & \text{for } t \geq 0 \end{cases} \tag{6.8}$$

We can relate the f-mode frequency ν_f and damping time τ_f to the mass via the equation-of-state independent fitting functions in Equations 6.9 and 6.10, where $\overline{M} = M/1.4M_{\odot}$ and $\overline{R} = R/10$ km (Pradhan, Chatterjee, Lanoye, & Jaikumar, 2022).

$$\nu_{f,0}(kHz) \approx 0.535 + 1.646\left(\frac{\overline{M}}{\overline{R}^3}\right)^{1/2} \tag{6.9}$$

$$\frac{1}{\tau_f(s)} \approx \frac{\overline{M}^3}{\overline{R}^4}\left[21.19 - 13.41\left(\frac{\overline{M}}{\overline{R}}\right)\right] \tag{6.10}$$

As any targeted pulsar would have a measured rotational period, we include a slight shift to the f-mode frequency from Krüger and Kokkotas (2020). We assume a co-rotating oscillation, as this is the "stable" case. For slowly rotating pulsars, this effect is almost negligible, but we include it here for completeness in

Equation 6.11, where ν_f is the frequency of the f-mode GW, $\nu_{f,0}$ is the non-rotating f-mode frequency, and Ω is the rotation frequency of the neutron star, all in units of kHz.

$$\nu_f = \nu_{f,0}\left(1 + 0.220\left(\frac{\Omega}{\nu_{f,0}}\right) - 0.0170\left(\frac{\Omega}{\nu_{f,0}}\right)^2\right) \tag{6.11}$$

Similar to the CW case, and as calculated by Owen (2010), the amplitude of the f-mode is calculated by integrating the GW luminosity for a damped sinusoid (Equation 6.12). It is quite similar to Equation 6.7 as both start with the assumption of a simple damped sinusoid, but here, the f-mode frequency ν_f is not twice the rotation rate.

$$h_{0,f} = \frac{1}{\pi d \nu_f}\left(\frac{5G}{c^3}\frac{E_{GW,f}}{\tau_f}\right)^{1/2} \tag{6.12}$$

We can also assume that the energy carried by the f-mode $E_{GW,f}$ is equal to the glitch energy in Equation 6.4 if it is the only emission.

To simplify things a bit, we will only be considering the mountain model parameterized by Yim and Jones (2020) discussed above as a potential CW emission, even though other forms of long-duration emission have been considered (see eg. Haskell and Jones (2024); Yim, Shao, and Xu (2024)). We will also assume that the only short duration burst emission is the f-mode, ignoring other potential emissions.

We treat each emission mechanism independently, and model the available energy for a particular channel as some fraction $\mathcal{F}$ of the total pulsar glitch energy in Equation 6.4. The fraction of the energy in the CW channel is $\mathcal{F}_{\mathrm{CW}}$ and the fraction of the energy in the f-mode channel is $\digamma_{\text{fmode}}$. These fractions are not required to add up to 1. The total energy of the system is then:

$$E_{\text{GW}} = E_{\text{CW}} + E_{\text{fmode}} = \digamma_{\text{CW}} E_{\text{Glitch}} + \digamma_{\text{fmode}} E_{\text{Glitch}} \tag{6.13}$$

Previous searches for continuous GWs near a Vela pulsar glitch placed upper limits on $h_{0,mtn}$ that approach but do not quite meet the spindown limit (Keitel et al., 2019).

In the event that the total energy of the glitch is not sufficient to explain the observations, we can let $\digamma_{\text{CW}}$ and $\digamma_{\text{fmode}}$ exceed unity.

The inclusion of $\digamma_{\text{CW}}$ and $\digamma_{\text{fmode}}$ explicitly gives Equations 6.14 and 6.15.

$$h_{0,SD} = \frac{1}{2\pi d\nu_s}\sqrt{\frac{5G\digamma_{\text{CW}} E_{\text{Glitch}}}{c^3 \tau_{CW}}} \tag{6.14}$$

$$h_{0,f} = \frac{1}{\pi d\nu_f}\left(\frac{5G}{c^3}\frac{\digamma_{\text{fmode}} E_{\text{Glitch}}}{\tau_f}\right)^{1/2} \tag{6.15}$$

6.5 Methods

Each type of search has a unique type of output and will require a different approach to use the result for source parameter estimation. Here, we consider different cases for the outcomes of the different searches and how the result can be used for follow-up analysis.

6.5.1 Parameter Estimation. We perform Monte Carlo simulations to generate random samples of astrophysical parameters. Since the CW and f-mode models we use should have common parameters for a common source, we have shared prior distributions for mass, radius, glitch size, distance, the mountain energy fraction $\mathcal{F}_{\rm CW}$, the f-mode energy fraction $\mathcal{F}_{\rm fmode}$, and the inclination angle ι. The CW likelihood will require an additional prior for τ_{CW}.

We can use Bayes' Theorem to compute a posterior distribution on the astrophysical parameters of the source pulsar. More detailed methods for how this is done in practice are given in Section 6.6.2.

6.5.2 Adapting Continuous Wave Search Results. A CW detection will likely take the form of a posterior distribution on $h_{0,mtn}$ and τ_{CW}. To convert this posterior into a likelihood for follow-up analysis, we need to normalize by the prior. Bayes' theorem in the context of gravitational-wave parameter estimation takes the form

$$p(\theta|\mathbf{d}) = \frac{L(\mathbf{d}|\theta)\pi(\theta)}{Z} = \frac{L(\mathbf{d}|\theta)\pi(\theta)}{\int L(\mathbf{d}|\theta)\pi(\theta)d\theta} \tag{6.16}$$

where $p(\theta|\mathbf{d})$ is the posterior probability density function of the source parameters θ given the data $\mathbf{d}$, $\pi(\theta)$ is the prior probability density function, $L(\mathbf{d}|\theta)$ is the conditional probability density function of the data given the source parameters, and Z is the evidence, which is just a renormalization factor, only dependent on the data which can be folded into the likelihood. To use an existing posterior distribution for our purposes, we need to calculate the conditional likelihood $L(\mathbf{d}|\theta)$. We can then treat this as any ordinary likelihood in our MCMC code. The piece we want is simply

$$\frac{L_{CW}(\mathbf{d}|\theta)}{Z} = \frac{p_{CW}(\theta|\mathbf{d})}{\pi(\theta)}. \tag{6.17}$$

We can perform this operation to extract the likelihood of different values of $h_{0,mtn}$ and τ_{CW}, which we can evaluate based on computed values from the prior distribution. This likelihood function can be used with conventional MCMC analysis techniques to compute the posterior distribution for astrophysical source parameters. This likelihood function can be combined with the relevant likelihood from a burst search result to create a joint likelihood function that appropriately combines both searches.

A non-detection by a pipeline such as PyFstat will be reported as upper limits on $h_{0,mtn}$ from injection recovery at different amplitudes and signal durations. These upper limits are computed by performing injections at different amplitudes and fitting a sigmoid curve to the recovery fractions. We can combine these detection efficiencies through simple linear interpolation to create a function that gives a detection efficiency for any set of astrophysical parameters. In the event of a non-detection, we will use this function subtracted from unity to weigh a set of sampled parameters (using the priors in Table 3) by how likely they were to not be detected by the search. This process is explained in more detail in Section 6.6.

6.5.3 Adapting Burst Search Results. A burst detection (from X-Pipeline specifically) will take the form of a time-frequency box centered on the f-mode frequency. For a narrow-band signal like the damped sinusoid of an f-mode, the bandwidth should be quite small, only a few Hz at most. The duration should be comparable to the f-mode damping time.

In this case, we use a conventional noise-weighted likelihood for the f-mode model on the GW data directly. We choose an 8 second on-source window such that the trigger start time is 2 seconds into the window and 32 times as long for an off-source window to compute the background spectra. Within the on-source window, we set our signal start time prior to be the trigger time from the search pipeline, and perform MCMC sampling, marginalizing over the start time.

A non-detection from the burst search will be reported as upper limits on the h_{rss} for different waveforms. Specific waveforms are injected into data at different amplitudes to determine how well the search pipeline recovers them. For the purposes of this analysis, we only consider "ringdown" waveforms, which are damped sinusoids, similar to the expected form of an f-mode. Each unique injection waveform is set at different frequencies and damping times to build an estimate of the parameter-dependent sensitivity. For each waveform, a detection efficiency curve is generated, representing the amplitude at which some fraction of injected waveforms were recovered. We can perform a linear interpolation of the curves at each parameter to construct a proper function of the signal parameters. With this, we can estimate the detection efficiency for any set of parameters, computing the frequency with Equation 6.9, the damping time with Equation 6.10, and the h_{rss} with Equation 6.2.

Since parts of the astrophysical parameter space may create frequencies or damping times outside of what was considered for the injections performed by the search pipelines, we use a nearest-neighbor approximation for parts of parameter space outside of the linear interpolation.

6.6 Example: The 2016 Vela Glitch

Let us consider the 2016 Vela glitch as an example. At 11:38:23.188 UTC on December 12, 2016, the Vela pulsar underwent a glitch with fractional change in the rotation rate $\Delta\nu/\nu = 1.431 \times 10^{-6}$ (Basu et al., 2019, 2021; Gügercinoğlu, Ge, Yuan, & Zhou, 2022; Palfreyman, Dickey, Hotan, Ellingsen, & Van Straten, 2018).[1] This glitch occurred during LIGO's second observing run and was analyzed for long-duration transient GWs (Keitel et al., 2019). However, the LIGO Livingston

[1] Aggregate glitch time and glitch size taken from `http://www.jb.man.ac.uk/pulsar/glitches.html`

detector was not taking data at the exact time of the glitch, so no search for short-duration GW bursts was performed at the time.

The long-duration transient search set upper limits at 90% detection efficiency for waveforms at twice the pulsar rotation frequency with durations of up to 120 days.

6.6.1 Targeted Burst Search. Since we lack two-detector coincidence at the exact time of the glitch, we assume there would have been no detection. This is a reasonable assumption since, given a fiduciary moment of inertia of $10^{45}\,\mathrm{g\,cm^2}$, this glitch would signify a loss of approximately 7.07×10^{42} ergs in rotational energy. Assuming all of this energy goes into a short-duration GW burst, this would give an approximate $h_{\mathrm{rss}} = 7.51 \times 10^{-23}$ at 1 kHz (from Equation 6.3). This is below even the most sensitive limits set during similar short duration searches performed in LIGO's third observing run (see eg. R. Abbott et al. (2024c)).

To estimate the background sensitivity near this glitch, we perform a mock search using the X-Pipeline targeted search pipeline (Sutton et al., 2010) on a window of two-detector coincidence approximately 3.5 hours after the glitch time. This should be a reasonable estimate of what limits would have been set by a proper targeted search had both detectors been observing. We run this on public data available for the second observing run (Rich Abbott et al., 2021). The quoted uncertainty on the glitch time was $\sigma = 2.5\,\mathrm{s}$ (Palfreyman et al., 2018), so we choose an on-source window to cover the 3σ region of $\pm 7.5\,\mathrm{s}$.

To estimate the sensitivity of the search, we perform injections of ringdown waveforms - damped sinusoids with a smooth ramp. We inject at frequencies ranging from 650 Hz to 3100 Hz with damping times of 0.1 s, 0.5 s, and 1.0 s. This

Central Frequency [Hz]	$h_{\text{rss},90}$ ($\text{Hz}^{-1/2}$)
850	2.547×10^{-22}
1100	3.640×10^{-22}
1350	3.310×10^{-22}
1600	3.489×10^{-22}

Table 1. The h_{rss} values at 90% detection efficiency for ringdown waveforms with damping times of 0.5 s for the off-source targeted search. This search was intended to estimate the detector network sensitivity had both interferometers been in observing at the time of the glitch.

Central Frequency [Hz]	$h_{\text{rss},90}$ ($\text{Hz}^{-1/2}$)
850	1.837×10^{-21}
1100	3.286×10^{-21}
1350	2.593×10^{-21}
1600	3.338×10^{-21}

Table 2. The h_{rss} values at 90% detection efficiency for ringdown waveforms with damping times of 0.5 s for the single detector on-source targeted search.

should cover the majority of the potential parameter space of f-modes and capture the most important frequency and duration based effects. The h_{rss} value at 90% detection efficiency are shown in Figure 33. For ringdown waveforms with damping times of 0.5 s, we place 90% upper limits on the h_{rss} as shown in Table 1.

For completeness, we also performed a single-detector search at the exact glitch time, using only used LIGO Hanford data. This search did not result in any candidate events. For ringdown waveforms with damping times of 0.5 s, we place the 90% upper limits on the h_{rss} shown in Table 2.

6.6.2 Joint Implications. We linearly interpolate the X-Pipeline detection efficiency curves for ringdown waveforms at multiple different frequencies and damping times to estimate the detection efficiency as a function of the frequency, the damping time, and the h_{rss}.

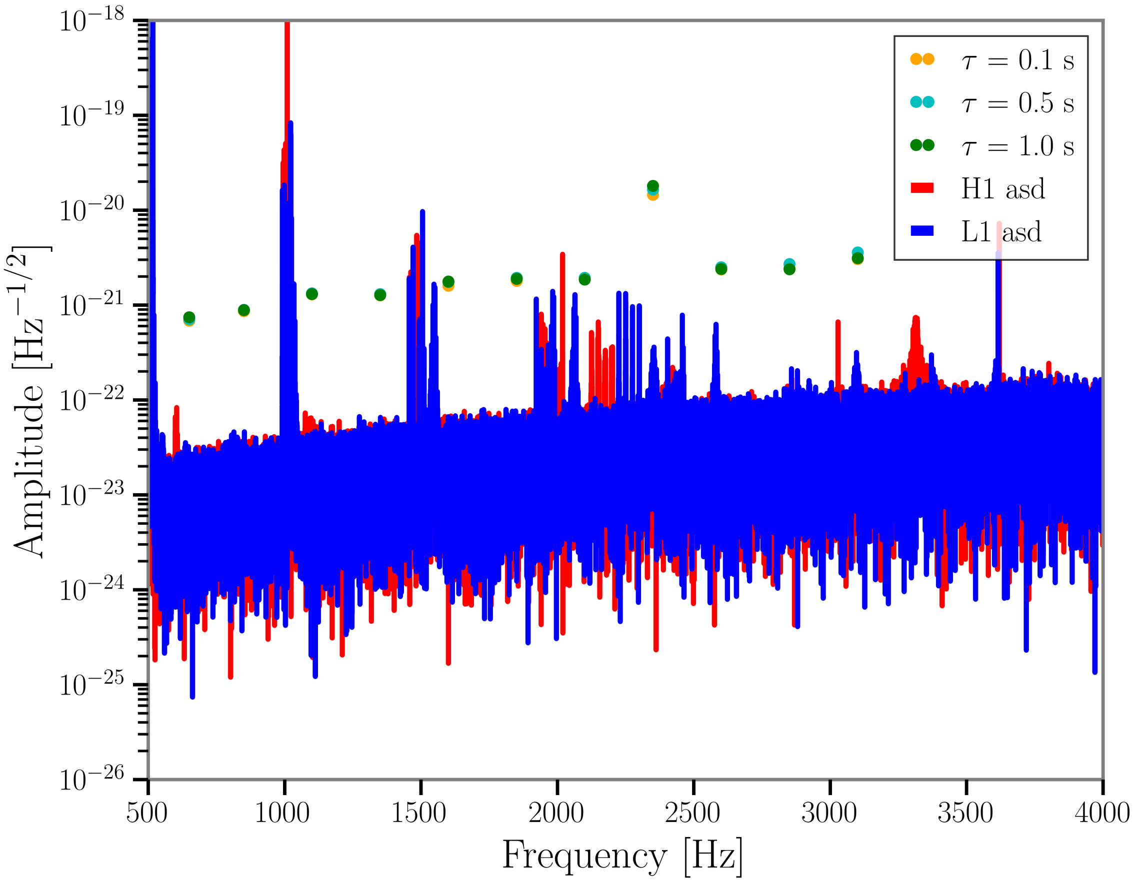

Figure 33. 90% detection efficiency limits for the targeted X-Pipeline search. Ringdown injections were used to approximate sensitivity to f-mode waveforms. Upper limits are shown for damping times of 0.1 s, 0.5 s, and 1.0 s. Background sensitivity for LIGO Hanford and LIGO Livingston are shown in red and blue, respectively.

We estimate the detection efficiency curves at different signal durations from the O2 long duration transient search (Keitel, 2024; Keitel et al., 2019). We then interpolate these to estimate the detection efficiency of a CW as a function of the duration/damping time τ_{CW} and the amplitude h_0.

In order to estimate the part of parameter space permitted by the absence of a detection, we assume that a GW was emitted in both channels but not detected by either search. Under this assumption, we want the probability that the GW associated with some arbitrary set of pulsar parameters would *not* be detected by a search.

We perform Monte Carlo simulations to generate random samples of pulsar parameters from the prior distributions in Table 3. For each sample, we compute the f-mode frequency ν_f (Equation 6.9), f-mode damping time τ_f (Equation 6.10), and f-mode amplitude $h_{0,f}$ (Equation 6.15) to compute a waveform (Equation 6.8) and the h_{rss} (Equation 6.2). We also compute the CW amplitude $h_{0,SD}$ (Equation 6.14. The f-mode h_{rss}, frequency and damping time are used to compute an estimated detection efficiency from the interpolated X-Pipeline detection efficiency curves. The CW amplitude and damping time τ_{CW} are used to compute an estimated detection efficiency from the interpolated PyFstat detection efficiency curves. This gives a probability that this sample would be detected by each search. We subtract these probabilities from unity to get the probability that the sample would not be detected by each search.

From these probabilities, we perform rejection sampling on the initial prior samples. For each sample in the prior, we start by computing the probability of non-detection by the CW transient $\mathcal{F}$-statistic search, then probabilistically reject samples based on this likelihood. For each of the samples that remain, we compute

Parameter	Meaning	Prior Distribution
M	Neutron Star Mass	$U(0.9M_\odot, 2.6M_\odot)$
R	Neutron Star Radius	$U(8\text{km}, 16\text{km})$
ν_s	Neutron Star rotation rate	$\delta(11.19Hz)$
$\Delta\nu_s/\nu_s$	Glitch-induced spin change	$\mathcal{N}(\mu = 1.431 \times 10^{-6}, \sigma = 10^{-10})$
ι	Inclination angle	$\mathcal{N}(\mu = 63.6°, \sigma = 0.6°)$
d	Distance	$\mathcal{N}(\mu = 287\,\text{pc},\ \sigma = 9.5\,\text{pc})$
τ_{CW}	CW decay time	$U(0.5, 120)$ days
$\mathcal{F}_{\text{CW}}$	Fraction of glitch energy in CW mode	$LogUniform(10^{-3}, 10)$
$\mathcal{F}_{\text{fmode}}$	Fraction of glitch energy in f-mode	$U(0, 100)$

Table 3. Prior distributions used for this analysis. The energy scaling factors $\mathcal{F}_{\text{fmode}}$ and $\mathcal{F}_{\text{CW}}$ extend to values above 1 in order to demonstrate the effects of the methodology for the search limits. Additional constraints on this prior space were enforced such that the f-mode frequency is restricted to be between 800 and 3200 kHz (or the expected frequency bounds of a GW candidate), the f-mode damping time is restricted to between 0 and 10 seconds (matching the limits from the numerical simulations of Andersson and Kokkotas (1998)), and the mass/radius values are restricted to a neutron star that obeys causality.

the probability of non-detection by the X-Pipeline search, then probabilistically reject samples based on this second likelihood. The samples that remain represent a posterior distribution according to Bayes' Theorem.

Figure 34 shows the posterior distribution on the mass, radius, $\mathcal{F}_{\text{fmode}}$, and $\mathcal{F}_{\text{CW}}$ using the mountain detection efficiency curves from (Keitel et al., 2019) and the ringdown detection efficiency curves from the X-pipeline search performed on a two-detector window near the glitch time (Figure 33).

From this result, it is easy to see that if no detection is made when $\mathcal{F}_{\text{fmode}} \approx 100$ and $\mathcal{F}_{\text{CW}} \approx 1$, then significant constraints could be placed on other parameters of the model. We consider how the constraints on the neutron star mass and radius might look if we assume that $\mathcal{F}_{\text{fmode}} = 100$ and $\mathcal{F}_{\text{CW}} = 1$ are fixed values. Figure 35 shows the 90% confidence region for the mass and radius posterior distribution when making these assumptions. We consider 3 scenarios: $\mathcal{F}_{\text{fmode}} = 100$ and $\mathcal{F}_{\text{CW}} =$

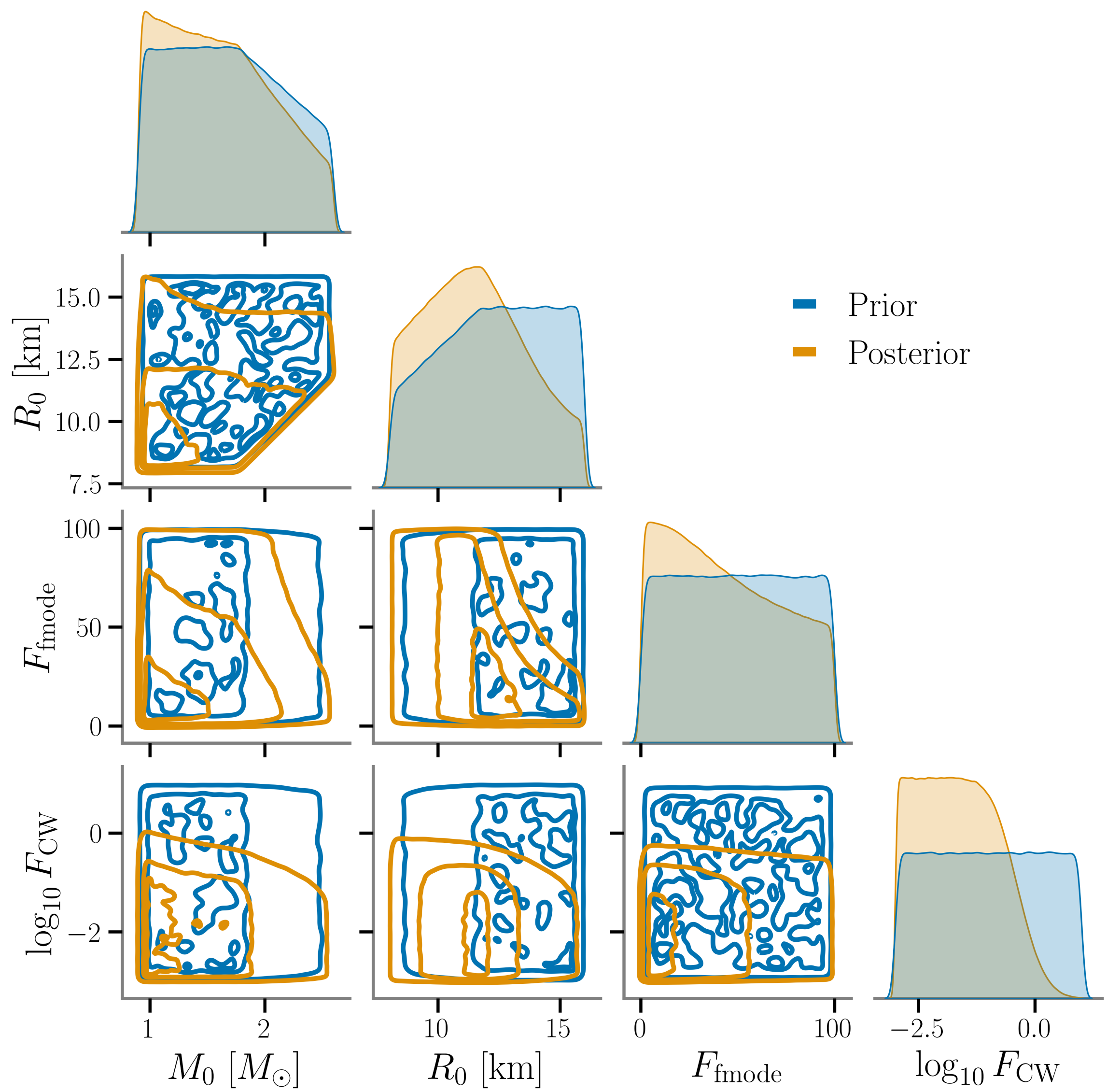

Figure 34. Mass, Radius, $F_{\rm fmode}$, and $F_{\rm CW}$ posterior distribution for the two-detector, off-source sensitivity. The different colors show how the prior space (blue) compares to the posterior (orange). Note that the $F_{\rm fmode}$ and $F_{\rm CW}$ terms are a fraction of the total glitch energy $E_{\rm Glitch}$, so values greater than 1 would imply more energy than actually released in the glitch.

0 to represent the constraints from only the f-mode upper limits, $\mathcal{F}_{\text{fmode}} = 0$ and $\mathcal{F}_{\text{CW}} = 1$ to represent the constraints from only the CW upper limits, and $\mathcal{F}_{\text{fmode}} = 100$ and $\mathcal{F}_{\text{CW}} = 1$ to represent the constraints from including both sets of limits. We also include several equations of state for reference. In this example, the H4 equation of state is permitted when only considering one model at a time but is not when considering both.

6.6.3 Hypothetical f-mode Detection. We also consider what the results might have looked like for a hypothetical detection of an f-mode near the limits of detection. In this case, we choose a $1.0 M_{\odot}$ neutron star with a 15.0 km radius with $\mathcal{F}_{\text{fmode}} = 100$. Although unrealistic for a glitch of this size, this serves as a demonstration of what the follow-up analysis of a significant candidate may look like. The black contour in Figure 35 shows what the 90% confidence region in mass-radius parameter space could look like for a detection.

6.7 Discussion and Conclusions

6.7.1 Future Observing Runs and Detectors. In order to estimate the sensitivity of future observing runs and detectors, we wanted to project optimistic results from O2 data to future detector sensitivities. Due to the nature of the CW search, we can use the same upper limits from the original search. For the burst search, we performed an additional targeted search with X-Pipeline on O2 data but using parameters for an optimally oriented source. We chose a sky location and on-source search time to maximize the quadrature sum of the plus- and cross- polarization antenna patterns for the two LIGO detectors while having similar detector noise as the Vela targeted search performed for Section 6.6. The target window was then December 12 13:25:39 UTC with a right ascension of $0.0099718°$ and a declination of $-39.3668°$.

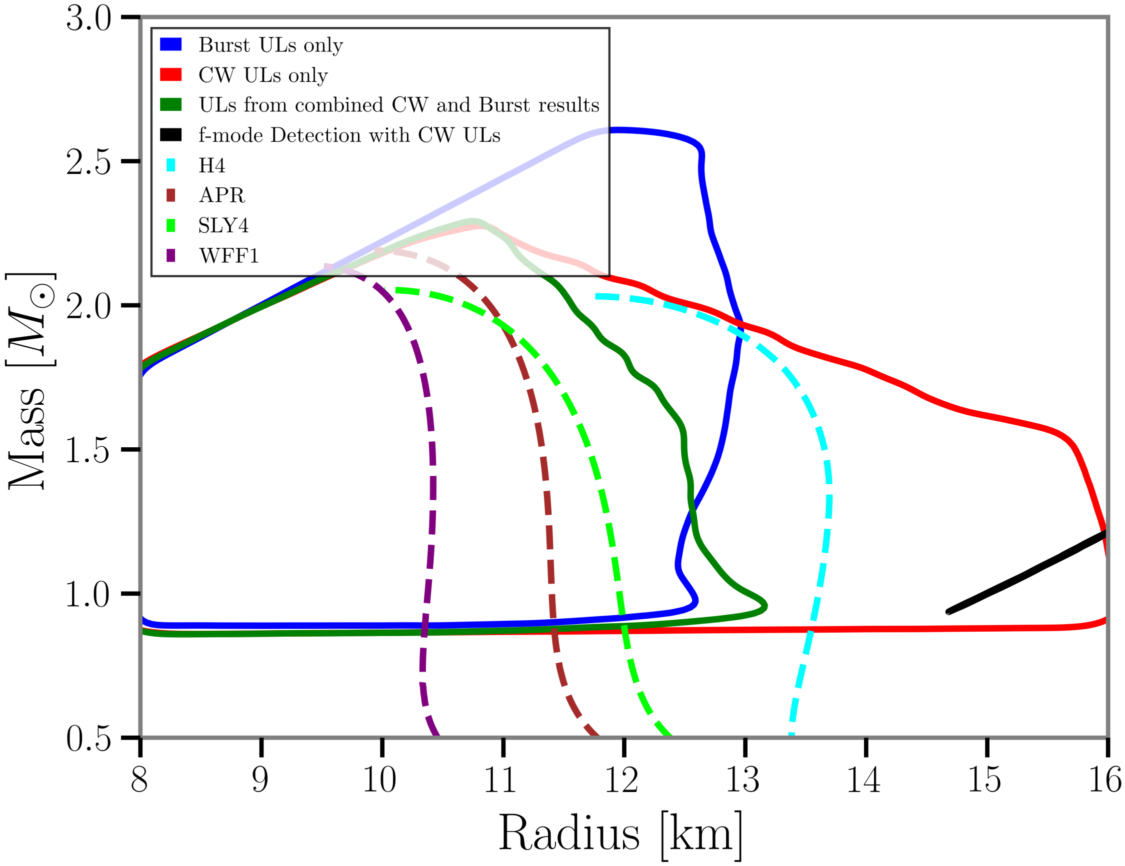

Figure 35. 90% confidence region on mass and radius for different analyses. The blue contour shows the constraints placed when only considering the upper limits from the X-Pipeline search when assuming $F_{\text{fmode}} = 100$ and without considering CW results. The red contour shows the constraints placed when only considering the upper limits from the CW search when assuming $F_{\text{CW}} = 1$ and without considering burst results. The green contour shows the constraints when considering both burst and CW limits when assuming $F_{\text{fmode}} = 100$ and $F_{\text{CW}} = 1$. Dotted lines show the mass/radius curves for different sample equations of state for reference. Notice, that in this (exaggerated) example, the H4 equation of state is consistent with the confidence intervals when considering either GW model on its own. However, when combining both models, H4 is no longer consistent. The black contour shows the constraints when an f-mode is detected. Here, an f-mode was injected into detector data for a $1.0\,M_\odot$ neutron star with a 15.0 km at $F_{\text{fmode}} = 100$.

We take the 90% confidence limits on h_{rss} (burst) and h_0 (CW) as our threshold for detection. We generate Monte Carlo samples from a restricted prior distribution. Here, we consider only a $1.0 M_\odot$ neutron star with a 15.0 km radius with $\mathcal{F}_{\mathrm{CW}} = 0.1$ and $\mathcal{F}_{\mathrm{fmode}} = 0.9$. The distance prior is uniform between 0 and 5 kpc and the fractional glitch size is logarithmically uniform between 2.0×10^{-11} and 1.0×10^{-5} to effectively span the range of glitch sizes for exhibited by the Vela pulsar[2].

These amplitudes are compared to the 90% values, interpolated across different injections, to determine if the parameters of a particular sample meet the threshold for detection. We require samples to meet the detection threshold for both types of searches simultaneously so we can assess the potential for an ideal dual-detection.

To assess future detectors, we project these upper limits to future detectors via the ratio of the ASDs at each frequency bin for each injection waveform. We compare our samples to these new thresholds to assess the dual-detectability for future detectors. Figure 36 shows the 90% confidence interval for dual-detection in current and future observing runs and detectors. Here, we compare O2 sensitivity (black) (Martynov, 2016) to O4 sensitivity (red) (Capote et al., 2025), O5 sensitivity (blue) (Barsotti et al., 2018a), and Cosmic Explorer sensitivity (green) (Srivastava et al., 2022). We predict that a glitch with the properties of the 2016 pulsar glitch (blue star) could have been simultaneously detectable by both burst and CW searches at O5 sensitivity.

6.7.2 Benefits of Joint Analysis.

We have demonstrated that for pulsar glitches, where a single object could emit multiple types of GWs, considering

[2] `http://www.jb.man.ac.uk/pulsar/glitches.html`

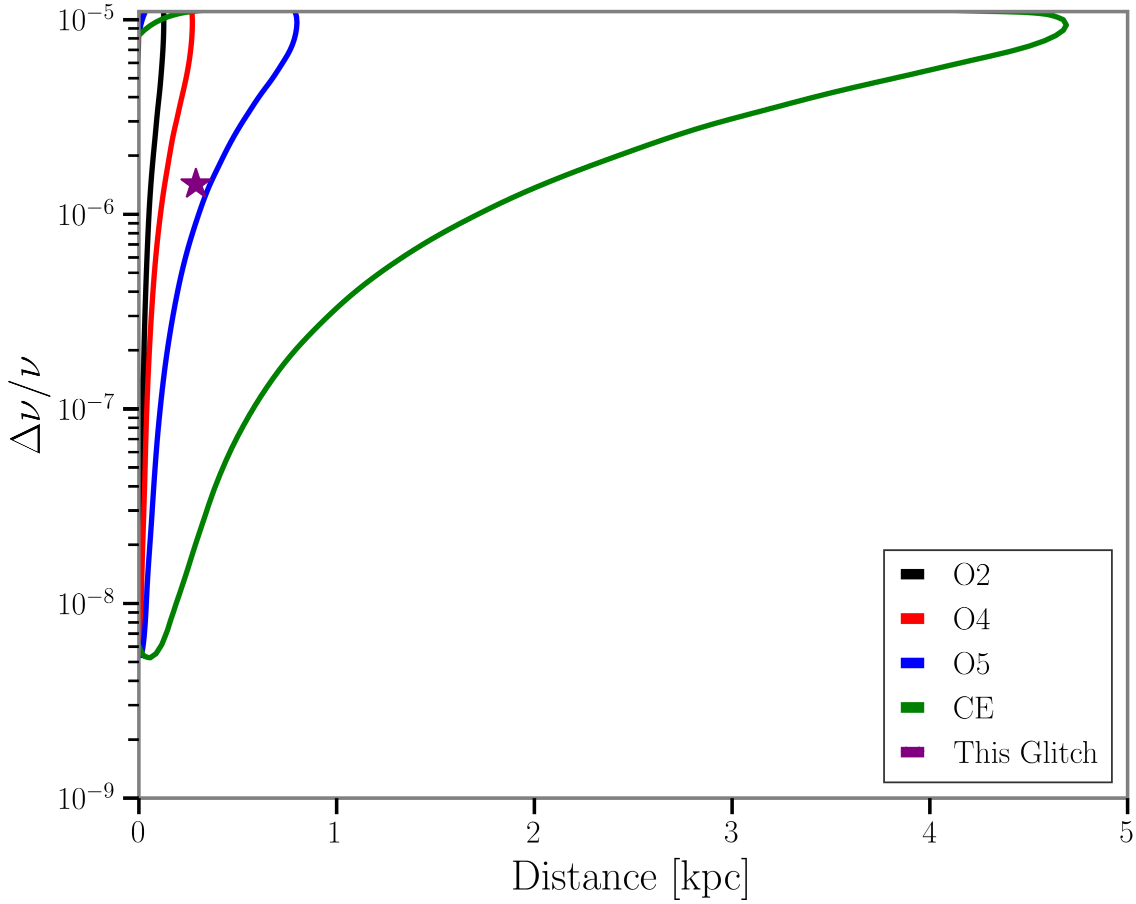

Figure 36. 90% confidence interval for the distance-glitch size parameter space for a Vela-like pulsar. This assumes a $1.0 M_{\odot}$ neutron star with a 15.0 km radius with $F_{\mathrm{CW}} = 0.1$ and $F_{\mathrm{fmode}} = 0.9$. The purple star denotes the 2016 Vela pulsar glitch, showing that, under these assumptions, this glitch could have produced fully detectable burst and CW gravitational waves at the estimated sensitivity of LIGO's fifth observing run.

both models simultaneously can place stronger constraints on the underlying astrophysics than either separately. Figure 35 shows theoretical constraints for the burst search only (blue) compared to constraints for the CW search only (red) and the constraints when considering the combined analysis (green). Each model is sensitive to different parts of the parameter space, so using both sets of search limits places stronger limits than either individual search on their own.

Considering specific models offers more interesting astrophysical implications than remaining model independent. Compared to conventional limits on h_0 for CW searches or the $h_{\rm rss}$ of ringdown waveforms for burst searches, constraints on the mass and radius of the neutron star are more tangible quantities and probe the underlying physics of the problem. The models that we have considered are not chosen at random, but instead have been chosen to best match pre-existing practices from previous GW searches. We believe that until a detection is made, the best way to improve searches for these GW sources is to begin making assumptions and placing newer, more interesting constraints.

6.8 Applying these Methods to the April 2024 Vela Pulsar Glitch

This section contains results that have not been reviewed or approved by the LIGO scientific collaboration (Abac et al., in prep.). I will not be discussing the results of the search directly, only the implications on astrophysical parameters based on the sensitivity estimates of the searches.

On April 29, 2024, the Vela pulsar experienced a large glitch, first observed (Zubieta et al., 2024; Zubieta et al., 2025) by the Argentine Institute of Radio Astronomy (Zubieta et al., 2023) and subsequently confirmed by several other observatories and precisely timed by the Mount Pleasant Observatory of the University of Tasmania (Palfreyman, 2024). This glitch happened shortly after the two Advanced LIGO detectors (The LIGO Scientific Collaboration, 2015) had restarted observations for the second half (O4b) of their fourth observing run (Capote et al., 2025) and were joined also by Advanced Virgo (Acernese et al., 2015). The searches conducted that the subsequent astrophysical limitations are based upon only include data from the Advanced LIGO detectors, as Advanced Virgo was not included.

For this analysis, we use the results of the X-PIPELINE targeted search (Sutton et al., 2010) for limits on the f-mode h_{rss} and the results of the time-domain Bayesian search (Dupuis & Woan, 2005; Pitkin, Isi, Veitch, & Woan, 2017) implemented in CWINPY (Pitkin, 2022) for limits on the CW h_0. In the case of CWINPY, we use the posterior distribution on amplitude h_0 and CW damping time τ_{CW} produced by CWINPY for an exponential decay profile, fixed orientation, and fixed at twice the pulsar rotation frequency. This likelihood distribution is interpreted as the probability that a given parameter would generate a waveform consistent with background noise. This is comparable to the CW likelihood computed from interpolated detection efficiency curves described in Section 6.6.2.

To sample the parameter space for the joint f-mode and transient mountain inference, we use the following priors. The mass prior is uniform from $0.9\,M_\odot$ to $2.6\,M_\odot$. The radius prior is uniform from 8 km to 16 km. Constraints are enforced such that the mass and radius obey causality and the neutron star does not collapse to a black hole. The prior for the glitch-induced spin change $\Delta f_{\mathrm{rot}}/f_{\mathrm{rot}}$ is a Gaussian distribution centered at 2.377×10^{-6} with $\sigma = 4.47 \times 10^{-11}$. We choose the inclination angle ι prior to be a double-peaked Gaussian distribution with peaks at 1.1048 and 2.0368 radians and $\sigma = 10.5$ mrad in order to match the prior used by the CWINPY search. The distance d prior is a Gaussian centered on 287 pc with

$\sigma = 9.5\,\text{pc}$. The mountain decay time τ_{CW} prior is uniform from 1 hour to 120 days. The prior for the mountain energy scaling factor $\digamma_{\text{CW}}$ is log-uniform from 10^{-3} to 1.0 and the prior for the f-mode energy scaling factor $\digamma_{\text{fmode}}$ is uniform between 0 and 5

Figure 37 shows that the search results set far stronger constraints on the $\digamma_{\text{CW}}$ than $\digamma_{\text{fmode}}$. The CW limits push below the spindown limit (defined in Equation 6.7 when $\digamma_{\text{CW}} = 1$). On the other hand, the burst search only pushes below the glitch energy threshold at frequencies below where this model is defined. This leads to upper limits on $\digamma_{\text{fmode}}$ at values greater than 1, implying that for an f-mode to be detected, it would have required more total energy than the glitch contained.

Given the CW-limited nature of this search, we ask what sorts of limits on the allowed mass and radius values could be placed when fixing the f-mode energy. We perform a second analysis, this time fixing $\digamma_{\text{fmode}}$ to 0.8 and allowing $\digamma_{\text{CW}}$ to freely vary. Figure 38 shows 90% confidence intervals on the mass and radius for different binned values of $\digamma_{\text{CW}}$. Larger values of $\digamma_{\text{CW}}$ lead to smaller values for both the mass and radius. This is driven by the moment of inertia relation in Equation 6.5. Increasing $\digamma_{\text{CW}}$ requires a smaller I_{zz} to compensate. This tells us that, given these search results, assuming that a CW carried a larger fraction of the glitch energy requires a smaller moment of inertia and, consequently, a smaller mass and radius.

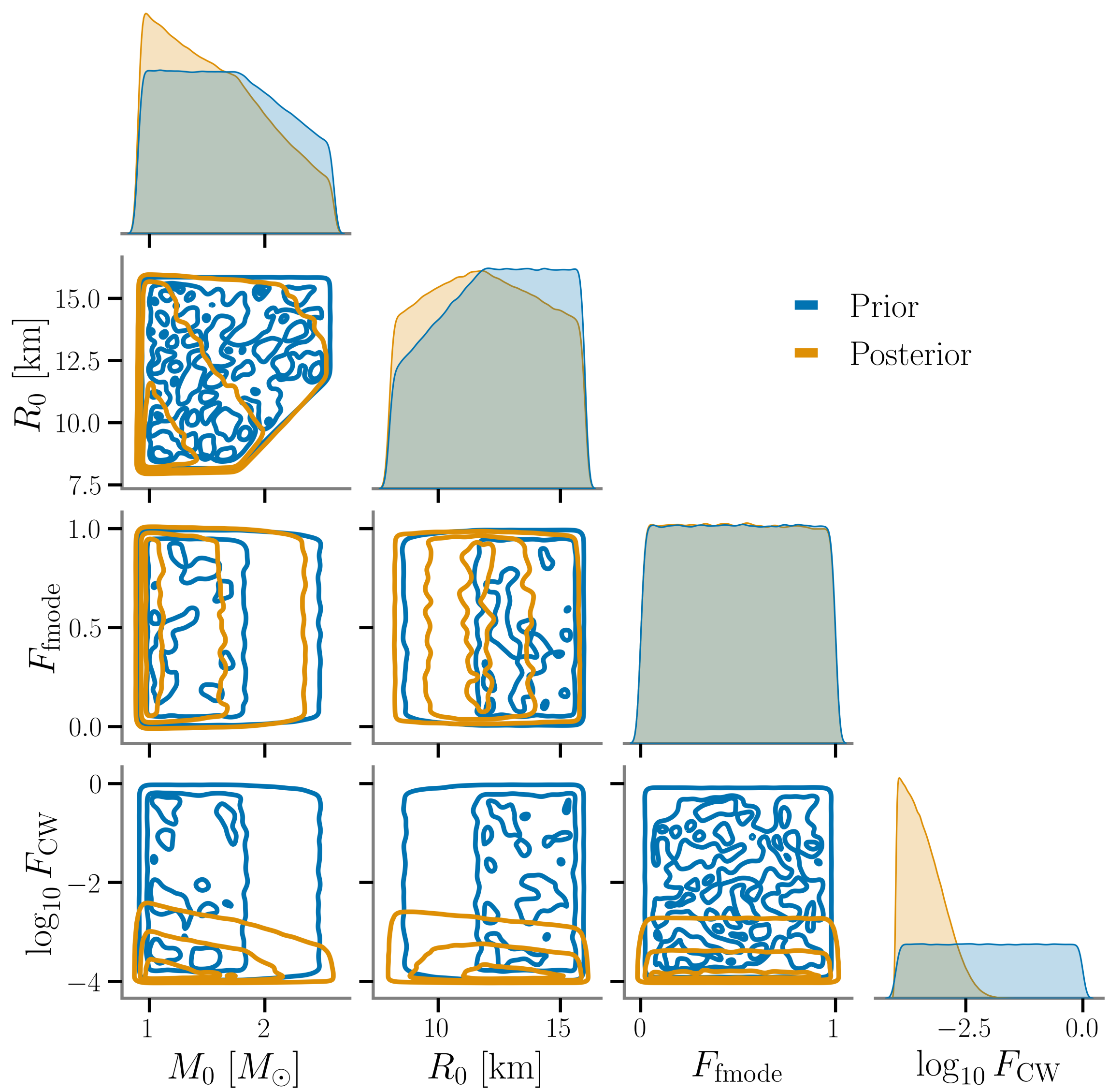

Figure 37. Posterior and prior distributions of mass, radius, $F_{\rm fmode}$, and $\log_{10}(F_{\rm CW})$ when allowing $F_{\rm CW}$ to vary between 0 and 1 and $F_{\rm fmode}$ to vary between 0 and 5. After including the search results, there is little effect on the allowed f-mode energy in the region ($F_{\rm fmode} < 1$) but a measurable effect on the allowed CW energy ($F_{\rm CW}$).

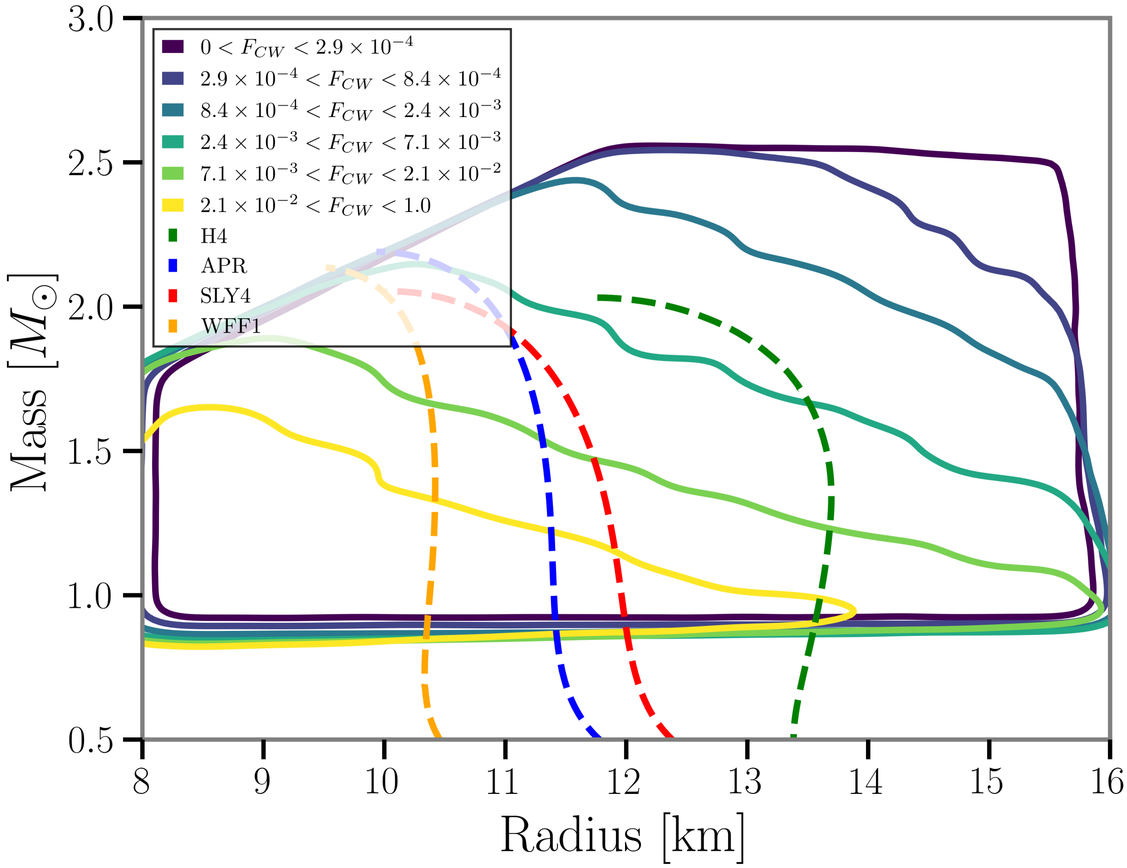

Figure 38. Mass and radius values allowed for different ranges of $\mathcal{F}_{\rm CW}$ with fixed $\mathcal{F}_{\rm fmode} = 0.8$. Under the very restrictive assumptions we have made, depending on the fraction of the pulsar glitch energy emitted in the mountain channel, the mass and radius of the Vela pulsar could be heavily constrained. The trend towards lower mass/radius values stems from the moment of inertia relationship, which peaks at higher mass/radius. For a given $\mathcal{F}_{\rm CW}$ bin, the search results favor lower energy values, so smaller moment of inertia values are more strongly supported. As the minimum $\mathcal{F}_{\rm CW}$ increases, the preferred moment of inertia decreases. Mass/radius curves for different equations of state are shown for comparison.

CHAPTER VII

CONCLUSION

The ever increasing sensitivity of gravitational wave detectors will bring great boons for astrophysics, but it will also introduce new problems that must be overcome. These problems will be unlike anything we have seen with the current generation of detectors. New noise sources that threaten the foundational assumptions of our search algorithms will need to be addressed and mitigated. Never before seen types of GW signals will need infrastructure built to properly process and derive new the new physics they will reveal. In this dissertation, I have explored several of these new concerns.

In Chapter IV, I showed how a correlated magnetic background created by global lightning strikes may cause issues with both unmodeled coherent GW searches as well as longer duration binary inspiral analyses. While it was not an issue during O3 and will not likely be an issue during O4, there is potential for magnetic contamination during O5. If third generation detectors have similar magnetic coupling mechnisms as the current generation, magnetic contamination will be a serious issue.

In Chapter V, I showed the potential for magnetar f-mode oscillations to place strong constraints on the neutron star matter equation of state. A single detection would allow for the most precise measurement of both the mass and radius of a neutron star ever. While searches for these signals are performed every observing run, no candidate events have been found. Unfortunately, at current sensitivity, even the most marginal candidates would likely correspond to unphysical magnetar parameters, so it is unlikely that the current generation of GW detectors will make a measurement for any realistic source distance ($\gtrsim 1\,\mathrm{kpc}$).

However, third generation detectors like Cosmic Explorer have the senstivity to potentially measure signals from a significant fraction of magnetars in our galaxy. When that time comes, we will be ready to process the signal and learn new physics.

But magnetars are not the only potential source of f-mode oscillations. In Chapter VI, I expanded on my previous work and explored the case of pulsar glitches. By improving on the method of processing search upper limit results, I presented a more statistically robust method of estimating astrophysical parameters in the case of a non-detection. Combining this method with a simple model for continuous gravitational radiation, I presented a new method for infering astrophysical parameters by combining two different forms of graviational waves emitted by a single object. This can significantly improve limits placed on the neutron star mass and radius should both long- and short- duration searches be possible. I performed a first-of-its-kind joint estimation on the 2016 Vela pulsar glitch using existing public data and followed it up with joint parameter estimation for the 2024 Vela pulsar glitch in a collaboration analysis. With this method, I predict that the first confident measurement of this type of object could realistically occur as soon as O5, a significant improvement over the magnetar case.

My work has shown that even though the next generation of gravitational wave detectors has not been built yet, there is still much to be done to prepare for the improvement to sensitivity. New construction methods or noise mitigation efforts will be needed to avoid unwanted contamination, and techniques for analyzing new types of signals are needed for when a new detection inevitably occurs. Even if I am not around to work on these problems, I hope that I have started a path for others to carry on this work so that gravitational wave and multimessenger astrophysics can continue to develop.

REFERENCES CITED

Aasi, J., et al. (2014, April). Constraints on Cosmic Strings from the LIGO-Virgo Gravitational-Wave Detectors. *Physical Review Letters*, *112*(13), 131101. Retrieved 2025-03-25, from `https://link.aps.org/doi/10.1103/PhysRevLett.112.131101` doi: 10.1103/PhysRevLett.112.131101

Aasi, J., et al. (2015, Mar). Advanced LIGO. *Classical and Quantum Gravity*, *32*(7), 074001. Retrieved from `https://doi.org/10.1088/0264-9381/32/7/074001` doi: 10.1088/0264-9381/32/7/074001

Abac, A. G., et al. (2024, August). Observation of Gravitational Waves from the Coalescence of a 2.5–4.5 $M_{\odot}$ Compact Object and a Neutron Star. *The Astrophysical Journal Letters*, *970*(2), L34. Retrieved 2025-04-23, from `https://iopscience.iop.org/article/10.3847/2041-8213/ad5beb` doi: 10.3847/2041-8213/ad5beb

Abac, A. G., et al. (in prep.). *Constraints on gravitational waves from the 2024 vela pulsar glitch.*

Abadie, J., et al. (2011a, June). SEARCH FOR GRAVITATIONAL WAVE BURSTS FROM SIX MAGNETARS. *The Astrophysical Journal*, *734*(2), L35. Retrieved 2024-01-05, from `https://iopscience.iop.org/article/10.1088/2041-8205/734/2/L35` doi: 10.1088/2041-8205/734/2/L35

Abadie, J., et al. (2011b, February). Search for gravitational waves associated with the August 2006 timing glitch of the Vela pulsar. *Physical Review D*, *83*(4), 042001. Retrieved 2025-03-25, from `https://link.aps.org/doi/10.1103/PhysRevD.83.042001` doi: 10.1103/PhysRevD.83.042001

Abbott, B., et al. (2007, September). Search for gravitational wave radiation associated with the pulsating tail of the SGR1806-20 hyperflare of 27 December 2004 using LIGO. *Physical Review D*, *76*(6), 062003. Retrieved 2023-08-10, from `https://link.aps.org/doi/10.1103/PhysRevD.76.062003` doi: 10.1103/PhysRevD.76.062003

Abbott, B., et al. (2016a, November). First targeted search for gravitational-wave bursts from core-collapse supernovae in data of first-generation laser interferometer detectors. *Physical Review D*, *94*(10), 102001. Retrieved 2025-03-25, from `https://link.aps.org/doi/10.1103/PhysRevD.94.102001` doi: 10.1103/PhysRevD.94.102001

Abbott, B., et al. (2016b, February). Observation of Gravitational Waves from a Binary Black Hole Merger. *Physical Review Letters*, *116*(6), 061102. Retrieved 2025-03-25, from `https://link.aps.org/doi/10.1103/PhysRevLett.116.061102` doi: 10.1103/PhysRevLett.116.061102

Abbott, B., et al. (2018, May). Constraints on cosmic strings using data from the first Advanced LIGO observing run. *Physical Review D*, *97*(10), 102002. Retrieved 2025-03-25, from `https://link.aps.org/doi/10.1103/PhysRevD.97.102002` doi: 10.1103/PhysRevD.97.102002

Abbott, B., et al. (2019, September). GWTC-1: A Gravitational-Wave Transient Catalog of Compact Binary Mergers Observed by LIGO and Virgo during the First and Second Observing Runs. *Physical Review X*, *9*(3), 031040. Retrieved 2025-03-25, from `https://link.aps.org/doi/10.1103/PhysRevX.9.031040` doi: 10.1103/PhysRevX.9.031040

Abbott, B., et al. (2020, April). Optically targeted search for gravitational waves emitted by core-collapse supernovae during the first and second observing runs of advanced LIGO and advanced Virgo. *Physical Review D*, *101*(8), 084002. Retrieved 2025-03-25, from `https://link.aps.org/doi/10.1103/PhysRevD.101.084002` doi: 10.1103/PhysRevD.101.084002

Abbott, B. P., et al. (2009, September). First LIGO search for gravitational wave bursts from cosmic (super)strings. *Physical Review D*, *80*(6), 062002. Retrieved 2025-03-25, from `https://link.aps.org/doi/10.1103/PhysRevD.80.062002` doi: 10.1103/PhysRevD.80.062002

Abbott, B. P., et al. (2017a, October). Gravitational Waves and Gamma-Rays from a Binary Neutron Star Merger: GW170817 and GRB 170817A. *The Astrophysical Journal Letters*, *848*(2), L13. Retrieved 2025-04-22, from `https://iopscience.iop.org/article/10.3847/2041-8213/aa920c` doi: 10.3847/2041-8213/aa920c

Abbott, B. P., et al. (2017b, October). GW170817: Observation of Gravitational Waves from a Binary Neutron Star Inspiral. *Physical Review Letters*, *119*(16), 161101. Retrieved 2023-07-26, from `https://link.aps.org/doi/10.1103/PhysRevLett.119.161101` doi: 10.1103/PhysRevLett.119.161101

Abbott, B. P., et al. (2017c, October). Multi-messenger Observations of a Binary Neutron Star Merger*. *The Astrophysical Journal Letters*, *848*(2), L12. Retrieved 2025-04-22, from `https://iopscience.iop.org/article/10.3847/2041-8213/aa91c9` doi: 10.3847/2041-8213/aa91c9

Abbott, B. P., et al. (2018, October). GW170817: Measurements of Neutron Star Radii and Equation of State. *Physical Review Letters*, *121*(16), 161101. Retrieved 2023-08-07, from `https://link.aps.org/doi/10.1103/PhysRevLett.121.161101` doi: 10.1103/PhysRevLett.121.161101

Abbott, B. P., et al. (2019, April). Search for transient gravitational-wave signals associated with magnetar bursts during advanced ligo's second observing run. *The Astrophysical Journal*, *874*(2), 163. Retrieved from `https://dx.doi.org/10.3847/1538-4357/ab0e15` doi: 10.3847/1538-4357/ab0e15

Abbott, R., et al. (2020, September). GW190521: A Binary Black Hole Merger with a Total Mass of 150 $M_{\odot}$. *Physical Review Letters*, *125*(10), 101102. Retrieved 2025-04-23, from `https://link.aps.org/doi/10.1103/PhysRevLett.125.101102` doi: 10.1103/PhysRevLett.125.101102

Abbott, R., et al. (2021a, Nov). All-sky search for long-duration gravitational-wave bursts in the third advanced ligo and advanced virgo run. *Phys. Rev. D*, *104*, 102001. Retrieved from `https://link.aps.org/doi/10.1103/PhysRevD.104.102001` doi: 10.1103/PhysRevD.104.102001

Abbott, R., et al. (2021b, December). All-sky search for short gravitational-wave bursts in the third Advanced LIGO and Advanced Virgo run. *Physical Review D*, *104*(12), 122004. Retrieved 2025-03-25, from `https://link.aps.org/doi/10.1103/PhysRevD.104.122004` doi: 10.1103/PhysRevD.104.122004

Abbott, R., et al. (2021c, June). Constraints on Cosmic Strings Using Data from the Third Advanced LIGO–Virgo Observing Run. *Physical Review Letters*, *126*(24), 241102. Retrieved 2025-03-25, from `https://link.aps.org/doi/10.1103/PhysRevLett.126.241102` doi: 10.1103/PhysRevLett.126.241102

Abbott, R., et al. (2021d, June). GWTC-2: Compact Binary Coalescences Observed by LIGO and Virgo during the First Half of the Third Observing Run. *Physical Review X*, *11*(2), 021053. Retrieved 2025-03-25, from `https://link.aps.org/doi/10.1103/PhysRevX.11.021053` doi: 10.1103/PhysRevX.11.021053

Abbott, R., et al. (2021e, July). Observation of Gravitational Waves from Two Neutron Star–Black Hole Coalescences. *The Astrophysical Journal Letters*, *915*(1), L5. Retrieved 2025-03-25, from `https://iopscience.iop.org/article/10.3847/2041-8213/ac082e` doi: 10.3847/2041-8213/ac082e

Abbott, R., et al. (2021f, Jul). Upper limits on the isotropic gravitational-wave background from Advanced LIGO and Advanced Virgo's third observing run. *Phys. Rev. D*, *104*, 022004. Retrieved from `https://link.aps.org/doi/10.1103/PhysRevD.104.022004` doi: 10.1103/PhysRevD.104.022004

Abbott, R., et al. (2022a, June). All-sky, all-frequency directional search for persistent gravitational waves from Advanced LIGO's and Advanced Virgo's first three observing runs. *Physical Review D*, *105*(12), 122001. Retrieved 2025-03-27, from `https://link.aps.org/doi/10.1103/PhysRevD.105.122001` doi: 10.1103/PhysRevD.105.122001

Abbott, R., et al. (2022b, November). All-sky search for continuous gravitational waves from isolated neutron stars using Advanced LIGO and Advanced Virgo O3 data. *Physical Review D*, *106*(10), 102008. Retrieved 2025-03-25, from `https://link.aps.org/doi/10.1103/PhysRevD.106.102008` doi: 10.1103/PhysRevD.106.102008

Abbott, R., et al. (2022c, June). Narrowband Searches for Continuous and Long-duration Transient Gravitational Waves from Known Pulsars in the LIGO-Virgo Third Observing Run. *The Astrophysical Journal*, *932*(2), 133. Retrieved 2025-03-25, from `https://iopscience.iop.org/article/10.3847/1538-4357/ac6ad0` doi: 10.3847/1538-4357/ac6ad0

Abbott, R., et al. (2023, December). GWTC-3: Compact Binary Coalescences Observed by LIGO and Virgo during the Second Part of the Third Observing Run. *Physical Review X*, *13*(4), 041039. Retrieved 2025-03-25, from https://link.aps.org/doi/10.1103/PhysRevX.13.041039 doi: 10.1103/PhysRevX.13.041039

Abbott, R., et al. (2024a, January). GWTC-2.1: Deep extended catalog of compact binary coalescences observed by LIGO and Virgo during the first half of the third observing run. *Physical Review D*, *109*(2), 022001. Retrieved 2025-03-25, from https://link.aps.org/doi/10.1103/PhysRevD.109.022001 doi: 10.1103/PhysRevD.109.022001

Abbott, R., et al. (2024b, May). Search for Gravitational-wave Transients Associated with Magnetar Bursts in Advanced LIGO and Advanced Virgo Data from the Third Observing Run. *The Astrophysical Journal*, *966*(1), 137. Retrieved 2024-06-10, from https://iopscience.iop.org/article/10.3847/1538-4357/ad27d3 doi: 10.3847/1538-4357/ad27d3

Abbott, R., et al. (2024c, May). Search for Gravitational-wave Transients Associated with Magnetar Bursts in Advanced LIGO and Advanced Virgo Data from the Third Observing Run. *The Astrophysical Journal*, *966*(1), 137. Retrieved 2025-01-13, from https://iopscience.iop.org/article/10.3847/1538-4357/ad27d3 doi: 10.3847/1538-4357/ad27d3

Acernese, F., et al. (2015, January). Advanced Virgo: a second-generation interferometric gravitational wave detector. *Classical and Quantum Gravity*, *32*(2), 024001. doi: 10.1088/0264-9381/32/2/024001

Acernese, F., et al. (2022). *The Virgo o3 run and the impact of the environment.* arXiv. Retrieved from https://arxiv.org/abs/2203.04014 doi: 10.48550/ARXIV.2203.04014

Ackley, K., et al. (2020). Neutron Star Extreme Matter Observatory: A kilohertz-band gravitational-wave detector in the global network. *Publications of the Astronomical Society of Australia*, *37*, e047. Retrieved 2023-08-08, from https://www.cambridge.org/core/product/identifier/S1323358020000399/type/journal_article doi: 10.1017/pasa.2020.39

Agazie, G., Anumarlapudi, A., Archibald, A. M., Arzoumanian, Z., Baker, P. T., Bécsy, B., ... The NANOGrav Collaboration (2023, July). The NANOGrav 15 yr Data Set: Evidence for a Gravitational-wave Background. *The Astrophysical Journal Letters*, *951*(1), L8. Retrieved 2025-03-27, from https://iopscience.iop.org/article/10.3847/2041-8213/acdac6 doi: 10.3847/2041-8213/acdac6

Allen, Z. A., et al. (2000, December). First Search for Gravitational Wave Bursts with a Network of Detectors. *Physical Review Letters*, *85*(24), 5046–5050. Retrieved 2025-03-03, from https://link.aps.org/doi/10.1103/PhysRevLett.85.5046 doi: 10.1103/PhysRevLett.85.5046

Alpar, M. A., Pines, D., Anderson, P. W., & Shaham, J. (1984, January). Vortex creep and the internal temperature of neutron stars. I - General theory. *The Astrophysical Journal*, *276*, 325–334. Retrieved 2025-03-25, from https://ui.adsabs.harvard.edu/abs/1984ApJ...276..325A (Publisher: IOP ADS Bibcode: 1984ApJ...276..325A) doi: 10.1086/161616

Anderson, P. W., & Itoh, N. (1975, July). Pulsar glitches and restlessness as a hard superfluidity phenomenon. *Nature*, *256*(5512), 25–27. Retrieved 2025-03-25, from https://www.nature.com/articles/256025a0 doi: 10.1038/256025a0

Andersson, N., Ferrari, V., Jones, D. I., Kokkotas, K. D., Krishnan, B., Read, J. S., ... Zink, B. (2011, February). Gravitational waves from neutron stars: promises and challenges. *General Relativity and Gravitation*, *43*(2), 409–436. Retrieved 2023-09-07, from http://link.springer.com/10.1007/s10714-010-1059-4 doi: 10.1007/s10714-010-1059-4

Andersson, N., & Kokkotas, K. D. (1996, November). Gravitational Waves and Pulsating Stars: What Can We Learn from Future Observations? *Physical Review Letters*, *77*(20), 4134–4137. Retrieved 2023-09-07, from https://link.aps.org/doi/10.1103/PhysRevLett.77.4134 doi: 10.1103/PhysRevLett.77.4134

Andersson, N., & Kokkotas, K. D. (1998, 10). Towards gravitational wave asteroseismology. *Monthly Notices of the Royal Astronomical Society*, *299*(4), 1059-1068. Retrieved from https://doi.org/10.1046/j.1365-8711.1998.01840.x doi: 10.1046/j.1365-8711.1998.01840.x

Ashton, G., Hübner, M., Lasky, P. D., Talbot, C., Ackley, K., Biscoveanu, S., ... Thrane, E. (2019, April). Bilby: A User-friendly Bayesian Inference Library for Gravitational-wave Astronomy. *The Astrophysical Journal Supplement Series*, *241*(2), 27. Retrieved 2023-05-26, from `https://iopscience.iop.org/article/10.3847/1538-4365/ab06fc` doi: 10.3847/1538-4365/ab06fc

Ashton, G., Keitel, D., Prix, R., & Tenorio, R. (2020, July). *PyFstat.* Zenodo. Retrieved from `https://doi.org/10.5281/zenodo.3967045` (`https://doi.org/10.5281/zenodo.3967045`) doi: 10.5281/zenodo.3967045

Aston, S. M., Barton, M. A., Bell, A. S., Beveridge, N., Bland, B., Brummitt, A. J., ... Wilmut, I. (2012, December). Update on quadruple suspension design for Advanced LIGO. *Classical and Quantum Gravity*, *29*(23), 235004. Retrieved 2025-05-28, from `https://iopscience.iop.org/article/10.1088/0264-9381/29/23/235004` doi: 10.1088/0264-9381/29/23/235004

Ball, M. (2019). *A2L decoupling filters.* Retrieved from `https://alog.ligo-wa.caltech.edu/aLOG/index.php?callRep=52129`

Ball, M., & Dwyer, S. (2019). *L2A rerouting.* Retrieved from `https://alog.ligo-wa.caltech.edu/aLOG/index.php?callRep=51604`

Ball, M., & Frey, R. (in prep.). *Methods for estimating neutron star parameters using multiple mechanisms for gravitational wave emission associated with pulsar glitches.*

Ball, M., Frey, R., & Merfeld, K. (2024, 08). Prospects for neutron star parameter estimation using gravitational waves from f modes associated with magnetar flares. *Monthly Notices of the Royal Astronomical Society*, *533*(3), 3090-3097. Retrieved from `https://doi.org/10.1093/mnras/stae1987` doi: 10.1093/mnras/stae1987

Barsotti, L., Fritschel, P., Evans, M., & Gras, S. (2018a). *The A+ design curve.* Retrieved from `https://dcc.ligo.org/LIGO-T1800042/public`

Barsotti, L., Fritschel, P., Evans, M., & Gras, S. (2018b). *Updated Advanced LIGO sensitivity design curve.* Retrieved from `https://dcc.ligo.org/LIGO-T1800044/public`

Barton, M., Torrie, C., Strain, K., & Robertson, N. (2012). *Models of the advanced LIGO suspensions in MATLAB.* Retrieved from `https://dcc.ligo.org/LIGO-T080188/public`

Basu, A., Joshi, B. C., Krishnakumar, M. A., Bhattacharya, D., Nandi, R., Bandhopadhay, D., ... Manoharan, P. K. (2019, November). Observed glitches in 8 young pulsars. *Monthly Notices of the Royal Astronomical Society*, stz3230. Retrieved 2025-01-13, from https://academic.oup.com/mnras/advance-article/doi/10.1093/mnras/stz3230/5637394 doi: 10.1093/mnras/stz3230

Basu, A., Shaw, B., Antonopoulou, D., Keith, M. J., Lyne, A. G., Mickaliger, M. B., ... Jordan, C. A. (2021, 11). The jodrell bank glitch catalogue: 106 new rotational glitches in 70 pulsars. *Monthly Notices of the Royal Astronomical Society*, *510*(3), 4049-4062. Retrieved from https://doi.org/10.1093/mnras/stab3336 doi: 10.1093/mnras/stab3336

Baym, G., Pethick, C., Pines, D., & Ruderman, M. (1969, November). Spin Up in Neutron Stars : The Future of the Vela Pulsar. *Nature*, *224*, 872–874. Retrieved 2025-03-25, from https://ui.adsabs.harvard.edu/abs/1969Natur.224..872B (ADS Bibcode: 1969Natur.224..872B) doi: 10.1038/224872a0

Benhar, O., Ferrari, V., & Gualtieri, L. (2004, December). Gravitational wave asteroseismology reexamined. *Physical Review D*, *70*(12), 124015. Retrieved 2023-09-07, from https://link.aps.org/doi/10.1103/PhysRevD.70.124015 doi: 10.1103/PhysRevD.70.124015

Bennett, M. F., Van Eysden, C. A., & Melatos, A. (2010, December). Continuous-wave gravitational radiation from pulsar glitch recovery: Gravitational radiation from glitch recovery. *Monthly Notices of the Royal Astronomical Society*, *409*(4), 1705–1718. Retrieved 2025-03-25, from https://academic.oup.com/mnras/article-lookup/doi/10.1111/j.1365-2966.2010.17416.x doi: 10.1111/j.1365-2966.2010.17416.x

Bidler, J., Smith, J., & Walker, M. (2018). *48 hz bumps found in DQ shift.* Retrieved from https://alog.ligo-wa.caltech.edu/aLOG/index.php?callRep=46045

Blakeslee, R. J., Mach, D. M., Bateman, M. G., & Bailey, J. C. (2014). Seasonal variations in the lightning diurnal cycle and implications for the global electric circuit. *Atmospheric research*, *135*, 228–243.

Buchdahl, H. A. (1959, November). General Relativistic Fluid Spheres. *Phys. Rev.*, *116*(4), 1027–1034. Retrieved from https://link.aps.org/doi/10.1103/PhysRev.116.1027 (Publisher: American Physical Society) doi: 10.1103/PhysRev.116.1027

Buikema, A., et al. (2020, September). Sensitivity and performance of the Advanced LIGO detectors in the third observing run. *Physical Review D*, *102*(6), 062003. Retrieved 2023-10-06, from `https://link.aps.org/doi/10.1103/PhysRevD.102.062003` doi: 10.1103/PhysRevD.102.062003

Capote, E., et al. (2025, March). Advanced LIGO detector performance in the fourth observing run. *Physical Review D*, *111*(6), 062002. Retrieved 2025-04-04, from `https://link.aps.org/doi/10.1103/PhysRevD.111.062002` doi: 10.1103/PhysRevD.111.062002

Christensen, N. (2018, nov). Stochastic gravitational wave backgrounds. *Reports on Progress in Physics*, *82*(1), 016903. Retrieved from `https://doi.org/10.1088/1361-6633/aae6b5` doi: 10.1088/1361-6633/aae6b5

Ciolfi, R., & Rezzolla, L. (2012, November). Poloidal-Field Instability in Magnetized Relativistic Stars. *The Astrophysical Journal*, *760*(1), 1. Retrieved 2023-10-12, from `https://iopscience.iop.org/article/10.1088/0004-637X/760/1/1` doi: 10.1088/0004-637X/760/1/1

Cirone, A., Fiori, I., Paoletti, F., Perez, M. M., Rodríguez, A. R., Swinkels, B. L., … Chincarini, A. (2019, oct). Investigation of magnetic noise in advanced Virgo. *Classical and Quantum Gravity*, *36*(22), 225004. Retrieved from `https://doi.org/10.1088/1361-6382/ab4974` doi: 10.1088/1361-6382/ab4974

Clark, J., Heng, I. S., Pitkin, M., & Woan, G. (2007, August). Evidence-based search method for gravitational waves from neutron star ring-downs. *Physical Review D*, *76*(4), 043003. Retrieved 2023-10-04, from `https://link.aps.org/doi/10.1103/PhysRevD.76.043003` doi: 10.1103/PhysRevD.76.043003

Cornish, N. J., & Littenberg, T. B. (2015, July). Bayeswave: Bayesian inference for gravitational wave bursts and instrument glitches. *Classical and Quantum Gravity*, *32*(13), 135012. Retrieved 2023-07-26, from `https://iopscience.iop.org/article/10.1088/0264-9381/32/13/135012` doi: 10.1088/0264-9381/32/13/135012

Corsi, A., & Owen, B. J. (2011, May). Maximum gravitational-wave energy emissible in magnetar flares. *Phys. Rev. D*, *83*, 104014. Retrieved from `https://link.aps.org/doi/10.1103/PhysRevD.83.104014` doi: 10.1103/PhysRevD.83.104014

Coughlin, M. W., Christensen, N. L., Rosa, R. D., Fiori, I., Gołkowski, M., Guidry, M., … Thrane, E. (2016, Oct). Subtraction of correlated noise in global networks of gravitational-wave interferometers. , *33*(22), 224003. Retrieved from https://doi.org/10.1088/0264-9381/33/22/224003 doi: 10.1088/0264-9381/33/22/224003

Coughlin, M. W., Cirone, A., Meyers, P., Atsuta, S., Boschi, V., Chincarini, A., … Thrane, E. (2018, May). Measurement and subtraction of Schumann resonances at gravitational-wave interferometers. *Phys. Rev. D*, *97*, 102007. Retrieved from https://link.aps.org/doi/10.1103/PhysRevD.97.102007 doi: 10.1103/PhysRevD.97.102007

Creighton, J. D. E., & Anderson, W. G. (2011). *Gravitational-wave physics and astronomy: an introduction to theory, experiment and data analysis.* Weinheim: Wiley-VCH.

Davis, D., Littenberg, T. B., Romero-Shaw, I. M., Millhouse, M., McIver, J., Di Renzo, F., & Ashton, G. (2022). *Subtracting glitches from gravitational-wave detector data during the third observing run.* arXiv. Retrieved from https://arxiv.org/abs/2207.03429 doi: 10.48550/ARXIV.2207.03429

Davis, D., et al. (2021, July). LIGO detector characterization in the second and third observing runs. *Classical and Quantum Gravity*, *38*(13), 135014. Retrieved 2024-02-07, from https://iopscience.iop.org/article/10.1088/1361-6382/abfd85 doi: 10.1088/1361-6382/abfd85

de Freitas Pacheco, J. A. (1998, August). Do soft gamma repeaters emit gravitational waves? *Astronomy and Astrophysics*, *336*, 397-401. doi: 10.48550/arXiv.astro-ph/9805321

Demetriades, N., Murphy, M., & Cramer, J. (2010, 01). *Validation of Vaisala's Global Lightning Dataset (GLD360) over the continental United States. Available at https://www.vaisala.com/sites/default/files/documents/6.Demetriades%2C%20Murphy%2C%20Cramer.pdf.*

Detweiler, S. L. (1975, April). A variational calculation of the fundamental frequencies of quadrupole pulsation of fluid spheres in general relativity. *The Astrophysical Journal*, *197*, 203–217. Retrieved 2023-07-10, from https://ui.adsabs.harvard.edu/abs/1975ApJ...197..203D (ADS Bibcode: 1975ApJ...197..203D) doi: 10.1086/153504

Doneva, D. D., Gaertig, E., Kokkotas, K. D., & Krüger, C. (2013, August). Gravitational wave asteroseismology of fast rotating neutron stars with realistic equations of state. *Phys. Rev. D*, *88*(4), 044052. Retrieved from https://link.aps.org/doi/10.1103/PhysRevD.88.044052 (Publisher: American Physical Society) doi: 10.1103/PhysRevD.88.044052

Drago, M., Klimenko, S., Lazzaro, C., Milotti, E., Mitselmakher, G., Necula, V., ... Yakushin, I. (2021, June). coherent WaveBurst, a pipeline for unmodeled gravitational-wave data analysis. *SoftwareX*, *14*, 100678. Retrieved 2024-06-12, from https://linkinghub.elsevier.com/retrieve/pii/S2352711021000236 doi: 10.1016/j.softx.2021.100678

Driggers, J. (2019). *(length to angle to length, L2A2L) controls issues in advanced LIGO (circa O3).* Retrieved from https://dcc.ligo.org/LIGO-G1900965

Duncan, R. C. (1998, May). Global Seismic Oscillations in Soft Gamma Repeaters. *The Astrophysical Journal*, *498*, L45–L49. Retrieved 2023-07-26, from https://ui.adsabs.harvard.edu/abs/1998ApJ...498L..45D (ADS Bibcode: 1998ApJ...498L..45D) doi: 10.1086/311303

Duncan, R. C., & Thompson, C. (1992, June). Formation of Very Strongly Magnetized Neutron Stars: Implications for Gamma-Ray Bursts. *Astrophysical Journal, Letters*, *392*, L9. doi: 10.1086/186413

Dupuis, R. J., & Woan, G. (2005, November). Bayesian estimation of pulsar parameters from gravitational wave data. *Physical Review D*, *72*(10), 102002. doi: 10.1103/PhysRevD.72.102002

Echeverria, F. (1989, Nov). Gravitational-wave measurements of the mass and angular momentum of a black hole. *Phys. Rev. D*, *40*, 3194–3203. Retrieved from https://link.aps.org/doi/10.1103/PhysRevD.40.3194 doi: 10.1103/PhysRevD.40.3194

Effler, A., Schofield, R. M. S., Frolov, V. V., González, G., Kawabe, K., Smith, J. R., ... McCarthy, R. (2015, February). Environmental influences on the LIGO gravitational wave detectors during the 6th science run. *Classical and Quantum Gravity*, *32*(3), 035017. Retrieved 2025-03-26, from https://iopscience.iop.org/article/10.1088/0264-9381/32/3/035017 doi: 10.1088/0264-9381/32/3/035017

Ferrario, L., Melatos, A., & Zrake, J. (2015, October). Magnetic Field Generation in Stars. *Space Science Reviews*, *191*(1-4), 77–109. Retrieved 2025-01-17, from http://link.springer.com/10.1007/s11214-015-0138-y doi: 10.1007/s11214-015-0138-y

Finn, L. S. (1992, Dec). Detection, measurement, and gravitational radiation. *Phys. Rev. D*, *46*, 5236–5249. Retrieved from https://link.aps.org/doi/10.1103/PhysRevD.46.5236 doi: 10.1103/PhysRevD.46.5236

Fritschel, P. (2019). *Broad noise peaks at 48 hz & 96 Hz: where do they come from?* Retrieved from https://alog.ligo-wa.caltech.edu/aLOG/index.php?callRep=47202

Fuentes, J. R., Espinoza, C. M., Reisenegger, A., Shaw, B., Stappers, B. W., & Lyne, A. G. (2017, December). The glitch activity of neutron stars. *Astronomy & Astrophysics*, *608*, A131. Retrieved 2025-01-22, from https://www.aanda.org/10.1051/0004-6361/201731519 doi: 10.1051/0004-6361/201731519

Gaertig, E., & Kokkotas, K. D. (2011, March). Gravitational wave asteroseismology with fast rotating neutron stars. *Phys. Rev. D*, *83*(6), 064031. Retrieved from https://link.aps.org/doi/10.1103/PhysRevD.83.064031 (Publisher: American Physical Society) doi: 10.1103/PhysRevD.83.064031

Gill, R., & Heyl, J. S. (2010, September). On the trigger mechanisms for soft gamma-ray repeater giant flares: On the trigger mechanisms for SGR giant flares. *Monthly Notices of the Royal Astronomical Society*, *407*(3), 1926–1932. Retrieved 2023-10-16, from https://academic.oup.com/mnras/article-lookup/doi/10.1111/j.1365-2966.2010.17038.x doi: 10.1111/j.1365-2966.2010.17038.x

Gold, T. (1968, May). Rotating Neutron Stars as the Origin of the Pulsating Radio Sources. *Nature*, *218*, 731–732. Retrieved 2025-03-24, from https://ui.adsabs.harvard.edu/abs/1968Natur.218..731G (ADS Bibcode: 1968Natur.218..731G) doi: 10.1038/218731a0

Gołkowski, M., Sarker, S., Renick, C., Moore, R., Cohen, M., Kułak, A., ... Kubisz, J. (2018). Ionospheric D region remote sensing using ELF sferic group velocity. *Geophysical Research Letters*, *45*(23), 12–739.

Gügercinoğlu, E., Ge, M. Y., Yuan, J. P., & Zhou, S. Q. (2022, February). Glitches in four gamma-ray pulsars and inferences on the neutron star structure. *Monthly Notices of the Royal Astronomical Society*, *511*(1), 425–439. Retrieved 2025-01-13, from https://academic.oup.com/mnras/article/511/1/425/6516426 doi: 10.1093/mnras/stac026

Hall, E. D., Kuns, K., Smith, J. R., Bai, Y., Wipf, C., Biscans, S., ... Yamamoto, H. (2021, Jun). Gravitational-wave physics with cosmic explorer: Limits to low-frequency sensitivity. *Phys. Rev. D*, *103*, 122004. Retrieved from `https://link.aps.org/doi/10.1103/PhysRevD.103.122004` doi: 10.1103/PhysRevD.103.122004

Hartigan, J. (1975). *Clustering algorithms.* John Wiley and Sons.

Hartle, J. B. (2002). *Gravity: An Introduction to Einstein's General Relativity* (1st ed.). Pearson.

Haskell, B. (2017, September). Probing neutron star interiors with pulsar glitches. *Proceedings of the International Astronomical Union*, *13*(S337), 203–208. Retrieved 2025-01-22, from `https://www.cambridge.org/core/product/identifier/S1743921317010663/type/journal_article` doi: 10.1017/S1743921317010663

Haskell, B., & Jones, D. (2024). Glitching pulsars as gravitational wave sources. *Astroparticle Physics*, *157*, 102921. Retrieved from `https://www.sciencedirect.com/science/article/pii/S092765052300107X` doi: https://doi.org/10.1016/j.astropartphys.2023.102921

Haskell, B., & Melatos, A. (2015, March). Models of pulsar glitches. *International Journal of Modern Physics D*, *24*(03), 1530008. Retrieved 2025-01-22, from `https://www.worldscientific.com/doi/abs/10.1142/S0218271815300086` doi: 10.1142/S0218271815300086

Helmling-Cornell, A., Ball, M., & Schofield, R. (2019). *Black glass blocking stray beam at HAM 3 viewport as part of 48 Hz investigation.* Retrieved from `https://alog.ligo-wa.caltech.edu/aLOG/index.php?callRep=52136`

Hewish, A., Bell, S. J., Pilkington, J. D. H., Scott, P. F., & Collins, R. A. (1968, February). Observation of a Rapidly Pulsating Radio Source. *Nature*, *217*, 709–713. Retrieved 2025-03-24, from `https://ui.adsabs.harvard.edu/abs/1968Natur.217..709H` (ADS Bibcode: 1968Natur.217..709H) doi: 10.1038/217709a0

Hild, S., et al. (2011, apr). Sensitivity studies for third-generation gravitational wave observatories. *Classical and Quantum Gravity*, *28*(9), 094013. Retrieved from `https://doi.org/10.1088/0264-9381/28/9/094013` doi: 10.1088/0264-9381/28/9/094013

Himemoto, Y., & Taruya, A. (2017). Impact of correlated magnetic noise on the detection of stochastic gravitational waves: Estimation based on a simple analytical model. *Phys. Rev. D*, *96*(2), 022004. doi: 10.1103/PhysRevD.96.022004

Himemoto, Y., & Taruya, A. (2019). Correlated magnetic noise from anisotropic lightning sources and the detection of stochastic gravitational waves. *Phys. Rev. D*, *100*(8), 082001. doi: 10.1103/PhysRevD.100.082001

Ho, W. C. G., Jones, D. I., Andersson, N., & Espinoza, C. M. (2020, May). Gravitational waves from transient neutron star f-mode oscillations. *Phys. Rev. D*, *101*(10), 103009. Retrieved from https://link.aps.org/doi/10.1103/PhysRevD.101.103009 (Publisher: American Physical Society) doi: 10.1103/PhysRevD.101.103009

Holle, R. (2020). personal communication. (Senior Scientist, Vaisala Inc.)

Hurley, K., Boggs, S. E., Smith, D. M., Duncan, R. C., Lin, R., Zoglauer, A., ... Cline, T. (2005, April). An exceptionally bright flare from SGR 1806-20 and the origins of short-duration γ-ray bursts. *Nature*, *434*, 1098–1103. Retrieved 2023-08-08, from https://ui.adsabs.harvard.edu/abs/2005Natur.434.1098H (ADS Bibcode: 2005Natur.434.1098H) doi: 10.1038/nature03519

Hurley, K., Cline, T., Mazets, E., Barthelmy, S., Butterworth, P., Marshall, F., ... Trombka, J. (1999, January). A giant periodic flare from the soft γ-ray repeater SGR1900+14. *Nature*, *397*, 41–43. Retrieved 2023-08-08, from https://ui.adsabs.harvard.edu/abs/1999Natur.397...41H (ADS Bibcode: 1999Natur.397...41H) doi: 10.1038/16199

Ioka, K. (2001, 10). Magnetic deformation of magnetars for the giant flares of the soft gamma-ray repeaters. *Monthly Notices of the Royal Astronomical Society*, *327*(2), 639-662. Retrieved from https://doi.org/10.1046/j.1365-8711.2001.04756.x doi: 10.1046/j.1365-8711.2001.04756.x

Israel, G. L., Esposito, P., Rea, N., Coti Zelati, F., Tiengo, A., Campana, S., ... Pons, J. (2016, April). The discovery, monitoring and environment of SGR J1935+2154. *Monthly Notices of the Royal Astronomical Society*, *457*(4), 3448–3456. Retrieved 2023-07-28, from https://academic.oup.com/mnras/article-lookup/doi/10.1093/mnras/stw008 doi: 10.1093/mnras/stw008

Janssens, K., Ball, M., Schofield, R. M., Christensen, N., Frey, R., Van Remortel, N., ... Ostrowski, M. (2023, January). Correlated 1–1000 Hz magnetic field fluctuations from lightning over Earth-scale distances and their impact on gravitational wave searches. *Physical Review D*, *107*(2), 022004. Retrieved 2024-11-17, from https://link.aps.org/doi/10.1103/PhysRevD.107.022004 doi: 10.1103/PhysRevD.107.022004

Jaranowski, P., Królak, A., & Schutz, B. F. (1998, August). Data analysis of gravitational-wave signals from spinning neutron stars: The signal and its detection. *Physical Review D*, *58*(6), 063001. Retrieved 2025-04-21, from `https://link.aps.org/doi/10.1103/PhysRevD.58.063001` doi: 10.1103/PhysRevD.58.063001

Jeffreys, H. (1998). *Theory of probability* (3rd ed ed.). Oxford [Oxfordshire] : New York: Clarendon Press ; Oxford University Press.

Kaspi, V. M., & Beloborodov, A. M. (2017). Magnetars. *Annual Review of Astronomy and Astrophysics*, *55*(1), 261-301. Retrieved from `https://doi.org/10.1146/annurev-astro-081915-023329` doi: 10.1146/annurev-astro-081915-023329

Kaspi, V. M., Taylor, J. H., & Ryba, M. F. (1994, June). High-Precision Timing of Millisecond Pulsars. III. Long-Term Monitoring of PSRs B1855+09 and B1937+21. *The Astrophysical Journal*, *428*, 713. Retrieved 2025-03-24, from `https://ui.adsabs.harvard.edu/abs/1994ApJ...428..713K` (Publisher: IOP ADS Bibcode: 1994ApJ...428..713K) doi: 10.1086/174280

Keitel, D. (2024). personal communication.

Keitel, D., Woan, G., Pitkin, M., Schumacher, C., Pearlstone, B., Riles, K., ... Weltevrede, P. (2019, September). First search for long-duration transient gravitational waves after glitches in the Vela and Crab pulsars. *Physical Review D*, *100*, 064058. Retrieved 2024-11-12, from `https://ui.adsabs.harvard.edu/abs/2019PhRvD.100f4058K` (Publisher: APS ADS Bibcode: 2019PhRvD.100f4058K) doi: 10.1103/PhysRevD.100.064058

Keith, M. J., Shannon, R. M., & Johnston, S. (2013, July). A connection between radio state changing and glitch activity in PSR J0742-2822. *Monthly Notices of the Royal Astronomical Society*, *432*(4), 3080–3084. Retrieved 2025-03-25, from `http://academic.oup.com/mnras/article/432/4/3080/1000476/A-connection-between-radio-state-changing-and` doi: 10.1093/mnras/stt660

Kemp, D. (1971). The global location of large lightning discharges from single station observations of ELF disturbances in the Earth-ionosphere cavity. *Journal of Atmospheric and Terrestrial Physics*, *33*(6), 919-927. Retrieved from `https://www.sciencedirect.com/science/article/pii/0021916971900912` doi: https://doi.org/10.1016/0021-9169(71)90091-2

Kissel, J. (2019). *New configuration for ETMX actuator does not signficantly impact calibration: OK to go for new calibration update.* Retrieved from `https://alog.ligo-wa.caltech.edu/aLOG/index.php?callRep=51782`

Kissel, J. (2022). *QUAD PUM (L2) DRIVEALIGN matrix, w/ SPOT and MECH banks infrastructure filled in as it was in O3.* Retrieved from `https://alog.ligo-wa.caltech.edu/aLOG/index.php?callRep=62192`

Kissel, J., & Dwyer, S. (2019). *QUAD L2 DRIVEALIGN Frequency-Dependent matrix broken apart and rearraged in an attempt to combat L2A2L coupling.* Retrieved from `https://alog.ligo-wa.caltech.edu/aLOG/index.php?callRep=49825`

Kokkotas, K. (2023). personal communication.

Kokkotas, K. D., Apostolatos, T. A., & Andersson, N. (2001, January). The inverse problem for pulsating neutron stars: a 'fingerprint analysis' for the supranuclear equation of state. *Monthly Notices of the Royal Astronomical Society*, *320*(3), 307–315. Retrieved 2023-09-07, from `https://academic.oup.com/mnras/article/320/3/307/1086201` doi: 10.1046/j.1365-8711.2001.03945.x

Kowalska-Leszczynska, I., Bizouard, M.-A., Bulik, T., Christensen, N., Coughlin, M., Gołkowski, M., … Rohde, M. (2017, Mar). Globally coherent short duration magnetic field transients and their effect on ground based gravitational-wave detectors. , *34*(7), 074002. Retrieved from `https://doi.org/10.1088/1361-6382/aa60eb` doi: 10.1088/1361-6382/aa60eb

Krüger, C. J., & Kokkotas, K. D. (2020, Sep). Fast rotating relativistic stars: Spectra and stability without approximation. *Phys. Rev. Lett.*, *125*, 111106. Retrieved from `https://link.aps.org/doi/10.1103/PhysRevLett.125.111106` doi: 10.1103/PhysRevLett.125.111106

Landau, L. D., & Lfshitz, E. M. (1975). Gravitational Waves. In *The Classical Theory of Fields* (4th ed., Vol. 2, pp. 368–381). Butterworth-Hinemann.

Lasky, P. D., Zink, B., & Kokkotas, K. D. (2012). *Gravitational waves and hydromagnetic instabilities in rotating magnetized neutron stars.*

Lemi sensors: Induction coil magnetometer. (2011). *Available at* *`http://www.lemisensors.com/wp-content/uploads/2016/02/LEMI-120_Datasheet.pdf`*. (Rev. 1.0)

Levin, Y. (2006, May). QPOs during magnetar flares are not driven by mechanical normal modes of the crust. *Monthly Notices of the Royal Astronomical Society: Letters*, *368*(1), L35–L38. Retrieved from https://doi.org/10.1111/j.1745-3933.2006.00155.x (_eprint: https://academic.oup.com/mnrasl/article-pdf/368/1/L35/2831330/368-1-L35.pdf) doi: 10.1111/j.1745-3933.2006.00155.x

Levin, Y., & Van Hoven, M. (2011, November). On the excitation of f modes and torsional modes by magnetar giant flares: Excitation of f modes and torsional modes. *Monthly Notices of the Royal Astronomical Society*, *418*(1), 659–663. Retrieved 2023-05-16, from https://academic.oup.com/mnras/article-lookup/doi/10.1111/j.1365-2966.2011.19515.x doi: 10.1111/j.1365-2966.2011.19515.x

Li, Y., Heng, I. S., Chan, M. L., Messenger, C., & Fan, X. (2022, Feb). Exploring the sky localization and early warning capabilities of third generation gravitational wave detectors in three-detector network configurations. *Phys. Rev. D*, *105*, 043010. Retrieved from https://link.aps.org/doi/10.1103/PhysRevD.105.043010 doi: 10.1103/PhysRevD.105.043010

Lindblom, L., & Detweiler, S. L. (1983, September). The quadrupole oscillations of neutron stars. *The Astrophysical Journal Supplement Series*, *53*, 73–92. Retrieved 2024-02-14, from https://ui.adsabs.harvard.edu/abs/1983ApJS...53...73L (ADS Bibcode: 1983ApJS...53...73L) doi: 10.1086/190884

Link, B., Epstein, R. I., & Van Riper, K. A. (1992, October). Pulsar glitches as probes of neutron star interiors. *Nature*, *359*(6396), 616–618. Retrieved 2025-01-22, from https://www.nature.com/articles/359616a0 doi: 10.1038/359616a0

Livingstone, M. A., Ng, C.-Y., Kaspi, V. M., Gavriil, F. P., & Gotthelf, E. V. (2011, April). POST-OUTBURST OBSERVATIONS OF THE MAGNETICALLY ACTIVE PULSAR J1846–0258. A NEW BRAKING INDEX, INCREASED TIMING NOISE, AND RADIATIVE RECOVERY. *The Astrophysical Journal*, *730*(2), 66. Retrieved 2025-03-25, from https://iopscience.iop.org/article/10.1088/0004-637X/730/2/66 doi: 10.1088/0004-637X/730/2/66

Lopez, D., & the LIGO, Virgo, and KAGRA collaborations. (2024, February). Search for Short-Duration Transient Gravitational Waves Emitted by Neutron Star Glitches. *Annalen der Physik*, *536*(2), 2200142. Retrieved 2025-01-22, from https://onlinelibrary.wiley.com/doi/10.1002/andp.202200142 doi: 10.1002/andp.202200142

Lopez, D., Tiwari, S., Drago, M., Keitel, D., Lazzaro, C., & Prodi, G. A. (2022, November). Prospects for detecting and localizing short-duration transient gravitational waves from glitching neutron stars without electromagnetic counterparts. *Physical Review D*, *106*(10), 103037. Retrieved 2023-10-06, from https://link.aps.org/doi/10.1103/PhysRevD.106.103037 doi: 10.1103/PhysRevD.106.103037

Lyne, A., Hobbs, G., Kramer, M., Stairs, I., & Stappers, B. (2010, July). Switched Magnetospheric Regulation of Pulsar Spin-Down. *Science*, *329*, 408. Retrieved 2025-03-25, from https://ui.adsabs.harvard.edu/abs/2010Sci...329..408L (ADS Bibcode: 2010Sci...329..408L) doi: 10.1126/science.1186683

Lyutikov, M. (2006, April). Magnetar giant flares and afterglows as relativistic magnetized explosions. *Monthly Notices of the Royal Astronomical Society*, *367*(4), 1594–1602. Retrieved 2023-05-16, from https://academic.oup.com/mnras/article-lookup/doi/10.1111/j.1365-2966.2006.10069.x doi: 10.1111/j.1365-2966.2006.10069.x

Macquet, A., Bizouard, M. A., Burns, E., Christensen, N., Coughlin, M., Wadiasingh, Z., & Younes, G. (2021, September). Search for Long-duration Gravitational-wave Signals Associated with Magnetar Giant Flares. *The Astrophysical Journal*, *918*(2), 80. Retrieved 2024-01-05, from https://iopscience.iop.org/article/10.3847/1538-4357/ac0efd doi: 10.3847/1538-4357/ac0efd

Macquet, A., Bizouard, M. A., Christensen, N., & Coughlin, M. (2021, Nov). Long-duration transient gravitational-wave search pipeline. *Phys. Rev. D*, *104*, 102005. Retrieved from https://link.aps.org/doi/10.1103/PhysRevD.104.102005 doi: 10.1103/PhysRevD.104.102005

Mansell, G. (2019). *Range integrands during Friday's SR3 tests.* Retrieved from https://alog.ligo-wa.caltech.edu/aLOG/index.php?callRep=47605

Martynov, D. o. (2016, June). Sensitivity of the Advanced LIGO detectors at the beginning of gravitational wave astronomy. *Physical Review D*, *93*(11), 112004. Retrieved 2025-04-04, from https://link.aps.org/doi/10.1103/PhysRevD.93.112004 doi: 10.1103/PhysRevD.93.112004

Mazets, E. P., & Golenetskii, S. V. (1981, March). Recent Results from the Gamma-Ray Burst Studies in the KONUS Experiment. *Astrophysics and Space Science*, *75*, 47–81. Retrieved 2025-01-17, from https://ui.adsabs.harvard.edu/abs/1981Ap&SS..75...47M (Publisher: Springer ADS Bibcode: 1981Ap&SS..75...47M) doi: 10.1007/BF00651384

Mazets, E. P., Golenetskij, S. V., & Guryan, Y. A. (1979, December). Soft gamma-ray bursts from the source B1900+14. *Soviet Astronomy Letters*, *5*, 343. Retrieved 2025-01-17, from https://ui.adsabs.harvard.edu/abs/1979SvAL....5..343M (ADS Bibcode: 1979SvAL....5..343M)

Mazets, E. P., Golentskii, S. V., Ilinskii, V. N., Aptekar, R. L., & Guryan, I. A. (1979, December). Observations of a flaring X-ray pulsar in Dorado. *Nature*, *282*, 587–589. Retrieved 2023-08-08, from https://ui.adsabs.harvard.edu/abs/1979Natur.282..587M (ADS Bibcode: 1979Natur.282..587M) doi: 10.1038/282587a0

McCarthy, R. (2019). *Comment to: status of 48 Hz investigation: often enhanced by fixable chiller fans, no vibrometry evidence for coupling at TCS mirror 2, or that it is related to 48 hz peak in ISI ST2 Z.* Retrieved from https://alog.ligo-wa.caltech.edu/aLOG/index.php?callRep=50599

McDermott, P. N., Van Horn, H. M., & Hansen, C. J. (1988, February). Nonradial oscillations of neutron stars. *The Astrophysical Journal*, *325*, 725. Retrieved 2023-05-26, from http://adsabs.harvard.edu/doi/10.1086/166044 doi: 10.1086/166044

Mereghetti, S., Pons, J. A., & Melatos, A. (2015, October). Magnetars: Properties, Origin and Evolution. *Space Science Reviews*, *191*(1-4), 315–338. Retrieved 2025-01-17, from http://link.springer.com/10.1007/s11214-015-0146-y doi: 10.1007/s11214-015-0146-y

Misner, C. W., Thorne, K. S., & Wheeler, J. A. (1973). *Gravitation.* New York: W. H. Freeman and Company.

Naccarato, K., Pinto, O., Garcia, S. A. M., Murphy, M., Demetriades, N., & Cramer, J. (2010). *Validation of the new NEW GLD 360 dataset in Brazil: First results 1. Available at https://www.vaisala.com/sites/default/files/documents/7.Naccarato%2C%20Pinto%2C%20Garcia_0.pdf.*

Nguyen, P., et al. (2021, July). Environmental noise in advanced LIGO detectors. *Classical and Quantum Gravity*, *38*(14), 145001. Retrieved 2025-03-26, from https://iopscience.iop.org/article/10.1088/1361-6382/ac011a doi: 10.1088/1361-6382/ac011a

Olausen, S. A., & Kaspi, V. M. (2014, May). The McGill Magnetar Catalog. *Astrophysical Journal, Supplement*, *212*(1), 6. doi: 10.1088/0067-0049/212/1/6

Owen, B. J. (2010, November). How to adapt broad-band gravitational-wave searches for r -modes. *Physical Review D*, *82*(10), 104002. Retrieved 2023-07-06, from https://link.aps.org/doi/10.1103/PhysRevD.82.104002 doi: 10.1103/PhysRevD.82.104002

Pacini, F. (1967, November). Energy Emission from a Neutron Star. *Nature*, *216*, 567–568. Retrieved 2025-03-24, from https://ui.adsabs.harvard.edu/abs/1967Natur.216..567P (ADS Bibcode: 1967Natur.216..567P) doi: 10.1038/216567a0

Palfreyman, J. (2024, May). Epoch of the glitch of the Vela pulsar (J0835-4510) to within 4 seconds. *The Astronomer's Telegram*, *16615*, 1. Retrieved from https://www.astronomerstelegram.org/?read=16615

Palfreyman, J., Dickey, J. M., Hotan, A., Ellingsen, S., & Van Straten, W. (2018, April). Alteration of the magnetosphere of the Vela pulsar during a glitch. *Nature*, *556*(7700), 219–222. Retrieved 2025-01-13, from https://www.nature.com/articles/s41586-018-0001-x doi: 10.1038/s41586-018-0001-x

Palmer, D. M., Barthelmy, S., Gehrels, N., Kippen, R. M., Cayton, T., Kouveliotou, C., … Tueller, J. (2005, April). A giant γ-ray flare from the magnetar SGR 1806–20. *Nature*, *434*(7037), 1107–1109. Retrieved 2025-05-28, from https://www.nature.com/articles/nature03525 doi: 10.1038/nature03525

Piro, A. L. (2005, December). Shear Waves and Giant-Flare Oscillations from Soft Gamma-Ray Repeaters. *The Astrophysical Journal*, *634*(2), L153–L156. Retrieved 2023-07-26, from https://iopscience.iop.org/article/10.1086/499049 doi: 10.1086/499049

Pitkin, M. (2022, September). CWInPy: A Python package for inference with continuous gravitational-wave signals from pulsars. *The Journal of Open Source Software*, *7*(77), 4568. doi: 10.21105/joss.04568

Pitkin, M., Isi, M., Veitch, J., & Woan, G. (2017, May). A nested sampling code for targeted searches for continuous gravitational waves from pulsars. *arXiv e-prints*, arXiv:1705.08978. doi: 10.48550/arXiv.1705.08978

Pradhan, B. K., Chatterjee, D., Lanoye, M., & Jaikumar, P. (2022, Jul). General relativistic treatment of f-mode oscillations of hyperonic stars. *Phys. Rev. C*, *106*, 015805. Retrieved from `https://link.aps.org/doi/10.1103/PhysRevC.106.015805` doi: 10.1103/PhysRevC.106.015805

Pradhan, B. K., Pathak, D., & Chatterjee, D. (2023, October). Constraining Nuclear Parameters Using Gravitational Waves from f-mode Oscillations in Neutron Stars. *The Astrophysical Journal*, *956*(1), 38. Retrieved 2023-10-09, from `https://iopscience.iop.org/article/10.3847/1538-4357/acef1f` doi: 10.3847/1538-4357/acef1f

Prix, R., Giampanis, S., & Messenger, C. (2011, July). Search method for long-duration gravitational-wave transients from neutron stars. *Physical Review D*, *84*(2), 023007. Retrieved 2025-03-25, from `https://link.aps.org/doi/10.1103/PhysRevD.84.023007` doi: 10.1103/PhysRevD.84.023007

Reisenegger, A., & Goldreich, P. (1992, August). A New Class of g-Modes in Neutron Stars. *The Astrophysical Journal*, *395*, 240. Retrieved 2023-10-09, from `https://ui.adsabs.harvard.edu/abs/1992ApJ...395..240R` (ADS Bibcode: 1992ApJ...395..240R) doi: 10.1086/171645

Rich Abbott, et al. (2021, January). Open data from the first and second observing runs of Advanced LIGO and Advanced Virgo. *SoftwareX*, *13*, 100658. Retrieved 2025-01-13, from `https://linkinghub.elsevier.com/retrieve/pii/S2352711021000030` doi: 10.1016/j.softx.2021.100658

Robinet, F., Arnaud, N., Leroy, N., Lundgren, A., Macleod, D., & McIver, J. (2020). Omicron: A tool to characterize transient noise in gravitational-wave detectors. *SoftwareX*, *12*, 100620. Retrieved from `https://www.sciencedirect.com/science/article/pii/S2352711020303332` doi: https://doi.org/10.1016/j.softx.2020.100620

Romani, R. W., Kandel, D., Filippenko, A. V., Brink, T. G., & Zheng, W. (2022, August). PSR J0952-0607: The Fastest and Heaviest Known Galactic Neutron Star. *The Astrophysical Journal Letters*, *934*(2), L17. Retrieved 2025-03-24, from https://iopscience.iop.org/article/10.3847/2041-8213/ac8007 doi: 10.3847/2041-8213/ac8007

Ruderman, M. (1969, August). Neutron Starquakes and Pulsar Periods. *Nature*, *223*, 597–598. Retrieved 2025-03-25, from https://ui.adsabs.harvard.edu/abs/1969Natur.223..597R (ADS Bibcode: 1969Natur.223..597R) doi: 10.1038/223597b0

Ryba, M. F., & Taylor, J. H. (1991a, April). High-Precision Timing of Millisecond Pulsars. I. Astrometry and Masses of the PSR 1855+09 System. *The Astrophysical Journal*, *371*, 739. Retrieved 2025-03-24, from https://ui.adsabs.harvard.edu/abs/1991ApJ...371..739R (Publisher: IOP ADS Bibcode: 1991ApJ...371..739R) doi: 10.1086/169938

Ryba, M. F., & Taylor, J. H. (1991b, October). High-Precision Timing of Millisecond Pulsars. II. Astrometry, Orbital Evolution, and Eclipses of PSR 1957+20. *The Astrophysical Journal*, *380*, 557. Retrieved 2025-03-24, from https://ui.adsabs.harvard.edu/abs/1991ApJ...380..557R (Publisher: IOP ADS Bibcode: 1991ApJ...380..557R) doi: 10.1086/170613

Said, R. K., Cohen, M. B., & Inan, U. S. (2013). Highly intense lightning over the oceans: Estimated peak currents from global GLD360 observations. *Journal of Geophysical Research: Atmospheres*, *118*(13), 6905-6915. Retrieved from https://agupubs.onlinelibrary.wiley.com/doi/abs/10.1002/jgrd.50508 doi: https://doi.org/10.1002/jgrd.50508

Schofield, R. (2016). *Lightning, LIGO, and GW150914. Available at https://dcc.ligo.org/LIGO-T1800506/public.*

Schofield, R., Ball, M., Helmling-Cornell, A., Shoemaker, D., Vorvick, C., & Banagiri, S. (2019). *New beating-shaker technique localizes coupling site of 48 Hz DARM peak, and black glass eliminates it.* Retrieved from https://alog.ligo-wa.caltech.edu/aLOG/index.php?callRep=52184

Schofield, R., Ball, M., Helmling-Cornell, A., & Warner, J. (2019). *Status of 48 hz investigation: often enhanced by fixable chiller fans, no vibrometry evidence for coupling at TCS mirror 2, or that it is related to 48 hz peak in ISI ST2 Z.* Retrieved from https://alog.ligo-wa.caltech.edu/aLOG/index.php?callRep=50315

Schofield, R., Nguyen, P., Austin, C., Banagiri, S., Merfeld, K., & Effler, A. (2019). *Pre-O3 PEM injection summary and links to individual logs.* Retrieved from https://alog.ligo-wa.caltech.edu/aLOG/index.php?callRep=49521

Shenar, T., Wade, G. A., Marchant, P., Bagnulo, S., Bodensteiner, J., Bowman, D. M., … Toonen, S. (2023, August). A massive helium star with a sufficiently strong magnetic field to form a magnetar. *Science*, *381*(6659), 761–765. Retrieved 2025-01-17, from https://www.science.org/doi/10.1126/science.ade3293 doi: 10.1126/science.ade3293

Shoemaker, D., Arnaud, N., & Sawada, T. (2025). *Observing scenario timeline graphic, post-o3.* Retrieved from https://dcc.ligo.org/LIGO-G2002127/public

Silber, I., Price, C., Galanti, E., & Shuval, A. (2015). Anomalously strong vertical magnetic fields from distant ELF/VLF sources. *Journal of Geophysical Research: Space Physics*, *120*(7), 6036-6044. Retrieved from https://agupubs.onlinelibrary.wiley.com/doi/abs/10.1002/2015JA021141 doi: https://doi.org/10.1002/2015JA021141

Simões, F., Pfaff, R., Berthelier, J.-J., & Klenzing, J. (2012, Jun 01). A Review of Low Frequency Electromagnetic Wave Phenomena Related to Tropospheric-Ionospheric Coupling Mechanisms. *Space Science Reviews*, *168*(1), 551-593. Retrieved from https://doi.org/10.1007/s11214-011-9854-0 doi: 10.1007/s11214-011-9854-0

Singh, A. (2017, January). Gravitational wave transient signal emission via Ekman pumping in neutron stars during post-glitch relaxation phase. *Physical Review D*, *95*(2), 024022. Retrieved 2025-03-25, from https://link.aps.org/doi/10.1103/PhysRevD.95.024022 doi: 10.1103/PhysRevD.95.024022

Smoluchowski, R. (1970, April). Frequency of Pulsar Starquakes. *Physical Review Letters*, *24*(16), 923–925. Retrieved 2025-03-25, from https://link.aps.org/doi/10.1103/PhysRevLett.24.923 doi: 10.1103/PhysRevLett.24.923

Sob'yanin, D. N. (2023, April). Ultraslow PSR J0901-4046 with an ultrahigh magnetic field of 3.2ıfmmode\times\else×\fi10^16\text \text \mathrmG. *Phys. Rev. D*, *107*(8), L081301. Retrieved from https://link.aps.org/doi/10.1103/PhysRevD.107.L081301 (Publisher: American Physical Society) doi: 10.1103/PhysRevD.107.L081301

Srivastava, V., Davis, D., Kuns, K., Landry, P., Ballmer, S., Evans, M., ... Sathyaprakash, B. S. (2022, May). Science-driven Tunable Design of Cosmic Explorer Detectors. *The Astrophysical Journal*, *931*(1), 22. Retrieved from https://doi.org/10.3847/1538-4357/ac5f04 (Publisher: American Astronomical Society) doi: 10.3847/1538-4357/ac5f04

Sumiyoshi, K., Kojo, T., & Furusawa, S. (2023). Equation of State in Neutron Stars and Supernovae. In I. Tanihata, H. Toki, & T. Kajino (Eds.), *Handbook of Nuclear Physics* (pp. 1–51). Singapore: Springer Nature Singapore. Retrieved 2025-01-17, from https://link.springer.com/10.1007/978-981-15-8818-1_104-1 doi: 10.1007/978-981-15-8818-1_104-1

Sutton, P. J. (2013). *A Rule of Thumb for the Detectability of Gravitational-Wave Bursts.* arXiv. Retrieved 2025-04-21, from https://arxiv.org/abs/1304.0210 (Version Number: 1) doi: 10.48550/ARXIV.1304.0210

Sutton, P. J., Jones, G., Chatterji, S., Kalmus, P., Leonor, I., Poprocki, S., ... Was, M. (2010, May). X-Pipeline: an analysis package for autonomous gravitational-wave burst searches. *New Journal of Physics*, *12*(5), 053034. Retrieved 2023-05-17, from https://iopscience.iop.org/article/10.1088/1367-2630/12/5/053034 doi: 10.1088/1367-2630/12/5/053034

The LIGO Scientific Collaboration. (2015, April). Advanced LIGO. *Classical and Quantum Gravity*, *32*(7), 074001. Retrieved 2025-03-26, from https://iopscience.iop.org/article/10.1088/0264-9381/32/7/074001 doi: 10.1088/0264-9381/32/7/074001

The LIGO Scientific Collaboration. (2022). *Noise Curves for use in simulations pre-O4.* Retrieved from https://dcc.ligo.org/LIGO-T2200043/public

Thompson, C., & Duncan, R. C. (1995, July). The soft gamma repeaters as very strongly magnetized neutron stars - I. Radiative mechanism for outbursts. *Monthly Notices of the Royal Astronomical Society*, *275*(2), 255-300. doi: 10.1093/mnras/275.2.255

Thompson, C., & Duncan, R. C. (1996, December). The Soft Gamma Repeaters as Very Strongly Magnetized Neutron Stars. II. Quiescent Neutrino, X-Ray, and Alfven Wave Emission. *Astrophysical Journal*, *473*, 322. doi: 10.1086/178147

Thorne, K. (1987). Gravitational radiation. In S. Hawking & W. Israel (Eds.), *Three hundred years of gravitation* (p. 330-458). Cambridge University Press.

Thorne, K. S. (1969, October). Nonradial Pulsation of General-Relativistic Stellar Models. III. Analytic and Numerical Results for Neutron Stars. *The Astrophysical Journal*, *158*, 1. Retrieved 2023-07-10, from `https://ui.adsabs.harvard.edu/abs/1969ApJ...158....1T` (ADS Bibcode: 1969ApJ...158....1T) doi: 10.1086/150168

Thrane, E., Christensen, N., & Schofield, R. (2013). Correlated magnetic noise in global networks of gravitational-wave interferometers: observations and implications. *Phys. Rev. D*, *87*, 123009. doi: 10.1103/PhysRevD.87.123009

Thrane, E., Christensen, N., Schofield, R. M. S., & Effler, A. (2014). Correlated noise in networks of gravitational-wave detectors: subtraction and mitigation. *Phys. Rev. D*, *90*(2), 023013. doi: 10.1103/PhysRevD.90.023013

Torrie, C. (2000). *Development of suspensions for the GEO 600 gravitational wave detector* (PhD thesis). University of Glasgow.

Tsui, L. K., & Leung, P. T. (2005, March). Universality in quasi-normal modes of neutron stars. *Monthly Notices of the Royal Astronomical Society*, *357*(3), 1029–1037. Retrieved 2023-09-07, from `https://academic.oup.com/mnras/article-lookup/doi/10.1111/j.1365-2966.2005.08710.x` doi: 10.1111/j.1365-2966.2005.08710.x

Van Eysden, C. A., & Melatos, A. (2008, November). Gravitational radiation from pulsar glitches. *Classical and Quantum Gravity*, *25*(22), 225020. Retrieved 2025-03-25, from `https://iopscience.iop.org/article/10.1088/0264-9381/25/22/225020` doi: 10.1088/0264-9381/25/22/225020

Veitch, J., Raymond, V., Farr, B., Farr, W., Graff, P., Vitale, S., … Wade, L. (2015, Feb). Parameter estimation for compact binaries with ground-based gravitational-wave observations using the lalinference software library. *Phys. Rev. D*, *91*, 042003. Retrieved from `https://link.aps.org/doi/10.1103/PhysRevD.91.042003` doi: 10.1103/PhysRevD.91.042003

Weber, J. (1960, January). Detection and Generation of Gravitational Waves. *Physical Review*, *117*(1), 306–313. Retrieved 2025-03-03, from `https://link.aps.org/doi/10.1103/PhysRev.117.306` doi: 10.1103/PhysRev.117.306

Weltevrede, P., Johnston, S., & Espinoza, C. M. (2011, March). The glitch-induced identity changes of PSR J1119-6127: The glitch-induced identity changes of PSR J1119-6127. *Monthly Notices of the Royal Astronomical Society*, *411*(3), 1917–1934. Retrieved 2025-03-25, from https://academic.oup.com/mnras/article-lookup/doi/10.1111/j.1365-2966.2010.17821.x doi: 10.1111/j.1365-2966.2010.17821.x

Wilson, O. H., & Ho, W. C. (2024, April). Gravitational waves from glitch-induced f -mode oscillations in quark and neutron stars. *Physical Review D*, *109*(8), 083006. Retrieved 2025-03-25, from https://link.aps.org/doi/10.1103/PhysRevD.109.083006 doi: 10.1103/PhysRevD.109.083006

Wąs, M., Sutton, P. J., Jones, G., & Leonor, I. (2012, Jul). Performance of an externally triggered gravitational-wave burst search. *Phys. Rev. D*, *86*, 022003. Retrieved from https://link.aps.org/doi/10.1103/PhysRevD.86.022003 doi: 10.1103/PhysRevD.86.022003

Yagi, K., & Yunes, N. (2017). Approximate universal relations for neutron stars and quark stars. *Physics Reports*, *681*, 1-72. Retrieved from https://www.sciencedirect.com/science/article/pii/S0370157317300492 (Approximate Universal Relations for Neutron Stars and Quark Stars) doi: https://doi.org/10.1016/j.physrep.2017.03.002

Yim, G., & Jones, D. I. (2020, September). Transient gravitational waves from pulsar post-glitch recoveries. *Monthly Notices of the Royal Astronomical Society*, *498*(3), 3138–3152. Retrieved 2025-03-25, from https://academic.oup.com/mnras/article/498/3/3138/5895343 doi: 10.1093/mnras/staa2534

Yim, G., & Jones, D. I. (2022, December). Gravitational waves from small spin-up and spin-down events of neutron stars. *Monthly Notices of the Royal Astronomical Society*, *518*(3), 4322–4329. Retrieved 2025-03-25, from https://academic.oup.com/mnras/article/518/3/4322/6843612 doi: 10.1093/mnras/stac3405

Yim, G., Shao, L., & Xu, R. (2024, July). High-priority targets for transient gravitational waves from glitching pulsars. *Monthly Notices of the Royal Astronomical Society*, *532*(4), 3893–3913. Retrieved 2025-04-21, from https://academic.oup.com/mnras/article/532/4/3893/7712489 doi: 10.1093/mnras/stae1659

Zhong, S.-Q., Dai, Z.-G., Zhang, H.-M., & Deng, C.-M. (2020, July). On the Distance of SGR 1935+2154 Associated with FRB 200428 and Hosted in SNR G57.2+0.8. *The Astrophysical Journal*, *898*(1), L5. Retrieved 2023-07-28, from https://iopscience.iop.org/article/10.3847/2041-8213/aba262 doi: 10.3847/2041-8213/aba262

Zhou, S., Gügercinoğlu, E., Yuan, J., Ge, M., & Yu, C. (2022, December). Pulsar Glitches: A Review. *Universe*, *8*(12), 641. Retrieved 2025-03-24, from https://www.mdpi.com/2218-1997/8/12/641 doi: 10.3390/universe8120641

Zink, B., Lasky, P. D., & Kokkotas, K. D. (2012, Jan). Are gravitational waves from giant magnetar flares observable? *Phys. Rev. D*, *85*, 024030. Retrieved from https://link.aps.org/doi/10.1103/PhysRevD.85.024030 doi: 10.1103/PhysRevD.85.024030

Zubieta, E., Furlan, S. A., Palacio, S. d., Garcia, F., Gancio, G., Lousto, C., ... PuMA Collaboration (2024, May). Detection of a new giant glitch in the Vela Pulsar observed from the Argentine Institute of Radio astronomy. *The Astronomer's Telegram*, *16608*, 1. Retrieved from https://www.astronomerstelegram.org/?read=16608

Zubieta, E., Missel, R., Furlan, S. B. A., Lousto, C. O., García, F., del Palacio, S., ... Wang, L. (2025, 2). Study of the 2024 major Vela glitch at the Argentine Institute of Radioastronomy. *arXiv e-prints*.

Zubieta, E., et al. (2023, May). First results of the glitching pulsar monitoring programme at the Argentine Institute of Radioastronomy. *Monthly Notices of the Royal Astronomical Society*, *521*(3), 4504-4521. doi: 10.1093/mnras/stad723